UNIVERSITY
OF TRENTO - Italy
DEPARTMENT OF INDUSTRIAL ENGINEERING

XXIX cycle

Doctoral School in Materials, Mechatronics and Systems Engineering

Multifunctionality in epoxy/glass fibers composites with graphene interphase

Haroon Mahmood

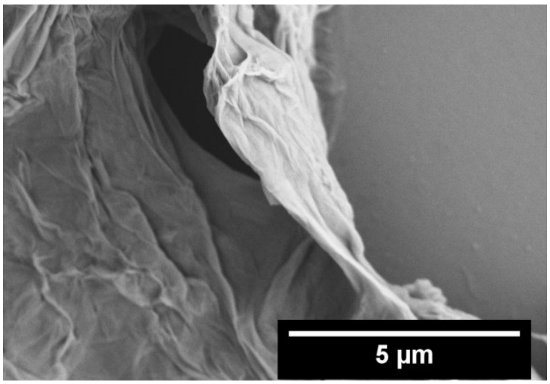

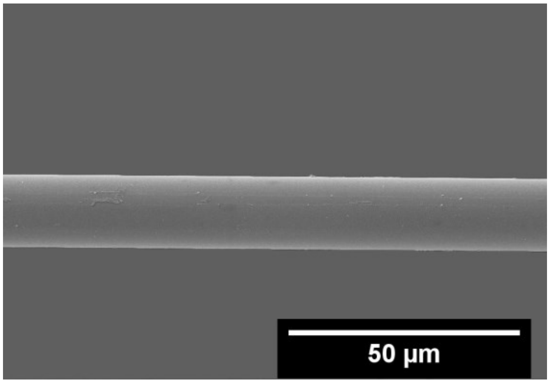

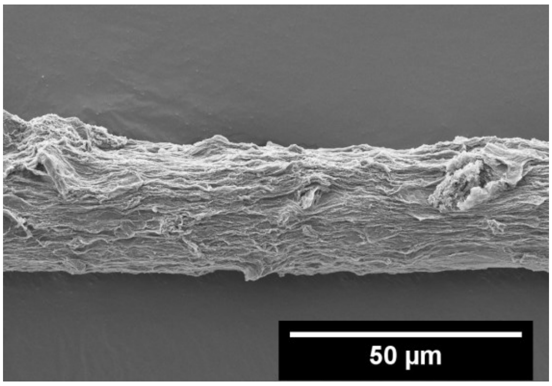

May 2017

MULTIFUNCTIONALITY IN EPOXY/GLASS FIBERS COMPOSITES WITH GRAPHENE INTERPHASE

Haroon Mahmood

E-mail: haroon88@gmail.com

Approved by:

Prof. Alessandro Pegoretti, Advisor
Department of Industrial Engineering
University of Trento, Italy.

Referees:

Prof. Jean-François Gérard,
National Institute of Applied Sciences
University of Lyon, France.

Prof. Luigi Torre,
Department of Civil and
Environmental Engineering
University of Perugia, Italy.

Ph.D. Commission:

Prof. Flavio Deflorian,
Department of Industrial Engineering
University of Trento, Italy.

Prof. Luigi Torre,
Department of Civil and
Environmental Engineering
University of Perugia, Italy.

Prof. Roberto Scotti
Department of Materials Science
University of Milan – Bicocca, Italy

University of Trento, Italy

Department of Industrial Engineering

May 2017

University of Trento - Department of Industrial Engineering

Doctoral Thesis

Haroon Mahmood - 2017
Published in Trento (Italy) – by University of Trento

To my dear family

Table of Contents

Abstract

In this project, the synergetic effect of a graphene interphase in epoxy/glass fibers composites was investigated by coating glass fibers (GF) with graphene oxide (GO) and reduced graphene oxide (rGO) nanosheets by an electrophoretic deposition (EPD) technique. Graphite oxide was prepared using modified Hummers method in which raw graphite powder was oxidized using potassium permanganate ($KMnO_4$) in acidic solution. Using ultrasonic technique, the graphite oxide was dispersed homogenously in water to create a stable GO suspension which was used as a bath in the EPD process.

For the coating process, two copper plates were used as electrodes in the EPD process in which GF were placed in front of anode for GO deposition since GO tends to carry negative charges due to oxygen functional groups attached on the graphene structure as produced in the modified Hummers method. The deposition was carried out at different applied fields while maintaining the dispersion concentration and deposition time constant. This process produced GF coated with GO nanosheets, while to obtain GF coated with rGO, GO coated fibers were subjected to chemical reduction process where the fibers were placed in an environment of hydrazine hydrate which reduced the GO coating on GF. Through this step, rGO coated GF were obtained.

The oxidation level of GO and rGO was evaluated using x-ray diffraction (XRD), Fourier transform infrared spectroscopy (FTIR) and x-ray photoelectron (XPS) spectroscopy techniques which confirmed the successful oxidation of graphite powder into graphite oxide due to liquid chemical oxidation process while the hydrazine reduction method reduced the oxygen amount from 34% to 10% in GO hence converting it into rGO. Scanning electron microscopy analysis of coated fibers revealed uniform coating of GF with GO and rGO where the amount of deposition increased with increased applied field.

The effect of GO or rGO coating on GF obtained by EPD process was first evaluated by determining the adhesion between GF and epoxy matrix. Single fiber fragmentation test was utilized to determine the interfacial shear strength (ISS) between the uncoated or coated fibers and epoxy matrix. Single fiber epoxy composites were prepared by using GO and rGO coated fibers and were tested using a mini-tensile testing machine and monitoring the lengths of fragments of fibers obtained during the tensile test. It was observed that in case of GO coated fibers, the ISS increased by 218% in comparison to uncoated fiber based composite. The increase of interfacial adhesion in this case, it can be attributed to the fact that GO carries

oxygen functional groups which creates physical and chemical bonding between both the GF surface and the epoxy matrix. For investigating the interactions between GF and GO, atomic force microscopy (AFM) was used to determine the interfacial adhesion between them by scratching GO on GF. It was proved that the delamination strength was higher than the ISS, hence proving the efficacy of the selected GO deposition method. On the other hand, single fiber fragmentation tests indicated a 70% increase in ISS for rGO coated GF when embedded in the epoxy matrix as compared to uncoated fibers. This increment is lower than that observed for GO coated fibers and it has been attributed to the fact that rGO does not possess enough oxygen based functional groups to efficiently interact with the polymer matrix. The observed increase in ISS with respect to uncoated GF is based on the frictional forces offered by the roughness of rGO nanosheets. This confirms that the presence of an interphase (either GO or rGO) creates favorable load transfer mechanism through either chemical or physical bonding or even both depending on the nature of the interphase.

To test further the positive effect of GO based interphase in epoxy/glass composites in terms of mechanical reinforcement, multifiber (uncoated and GO or rGO coated) reinforced epoxy composites were created by hand lay-up method. Laminas of fibers were wetted by epoxy resin and stacked over one another in certain number depending on the thickness of the resultant composite. These composites were subjected to various mechanical tests, such as flexural tests, short-beam shear tests, mode I interlaminar fracture toughness and creep tests which also confirmed that GO and rGO based interphase in epoxy/glass composites increase the performances of the composite with respect to that of the uncoated GF based composites. GO proved to be the best interphase in terms of mechanical properties obtained, as proved before.

The multifunctionality of such interphases based on graphene was analyzed and confirmed using multiple tests on epoxy/glass composites containing uncoated and coated (GO or rGO). In particular, the electrical and thermal conductivity of the composites were tested in which the composites based on rGO interphase showed the highest conductivity which not only confirms that rGO coated fibers in epoxy/glass composites render the composites conductive but also proves the successful chemical reduction process used in this work.

These conductive composites were subjected to piezoresistivity tests in which the applied longitudinal strain in different modes resulted in change in resistance thus showing a possibility of using such composites as strain sensing devices or for structural health monitoring purposes in automotive or aerospace applications.

These conductive composite specimens were also analyzed for their dielectric properties. The tests showed increased permittivity values as compared to both uncoated and GO coated composites thus revealing the possibility to use composites containing rGO coated fibers for electromagnetic interference shielding applications.

List of Figures

List of Tables

List of abbreviations and acronyms

ASTM	American standard for testing and materials
BG	Bi-layer graphene
CC	Calibration compliance
CMG	Chemically modified graphene
CNT	Carbon nanotube
CVD	Chemical vapor deposition
DCB	Double Cantilever beam
DMA	Dynamic mechanical analysis
DSC	Differential scanning calorimetry
E_{DISS}	Dissipation energy
EMI	Electromagnetic interference shielding
ENF	End notch fracture
EPD	Electrophoretic deposition
ESD	Electrostatic discharge
FESEM	Field emission scanning electron microscopy
FFM	Friction force microscopy
FG	Few-layer graphene
F_{IF}	Interfacial adhesion between GO and GF
F_{L}	Lateral force
F_{N}	Normal force
FRPC	Fiber reinforced polymer composites
F_{S}	Substrate force
FTIR	Fourier transform infrared spectroscopy
G_{a}	Shear modulus of interface
GF	Glass fiber
G_{I}	Strain energy release rate
G_{Ic}	Critical strain energy release rate
GnP	Graphene nanoplatelets
GO	Graphene oxide
HOPG	Highly ordered prisine graphene

ILSS	Interlaminar shear strength
ISO	International standard organization
ISS	Interfacial shear strength
K_N	Normal spring constant
K_T	Torsional spring constant
L_C	Critical length of fiber fragments
L_S	Fiber fragment length at saturation
MBT	Modified beam theory
MCC	Modified calibration compliance
MG	Multi-layer graphene
NL	Non-linearity
PEDOT:PSS	Poly (3,4-ethyencdioxy thiophene) poly (styrenesulphonate)
rGO	Reduced graphene oxide
SBS	Short beam shear strength
SERR	Strain energy release rate
SFFT	Single fiber fragmentation test
SG	Single-layer graphene
TGA	Thermogravimetric analysis
VIS	Visual crack propagation
XRD	X-ray diffraction
XRF	X-ray fluorescence spectroscopy

Chapter 1 - Introduction

In recent times, the increasing attention given to multifunctional composites has been justified by, not only the increasing demand from the industry to lower the weight of structural components, but also due to the noteworthy ‘additional functionalities’ offered by such next generation composites. The importance of these materials come from the fact that, in comparison to traditional composite materials, superior mechanical properties and specific functional requirements can be realized, like energy storage, healing capabilities, sensing and actuation, strain monitoring etc. The possibility to achieve multifunctionality in composites through the addition of relatively weightless and extremely small sized nanoparticles opens a wide range of opportunities.

In terms of performance and potential applications in the industry, nanocomposites have shown the perspective to ultimately redefine the field of traditional composite materials. However, many limitations have presented a challenge to the scientists and engineers in their path to develop nanocomposites in which the primary limitation is their processing. This is one of the biggest challenge holding industries back in developing the processing-manufacturing technologies in terms of quantity and value for commercialization. For example, dispersion of nanoparticles is extremely difficult because, due to their high surface area, they tend to agglomerate together. Such agglomerates in composites could potentially become a failure point for the structure since a force can result in splitting of the agglomerate nanoparticle [1]. In addition, chemical compatibility between the matrix and the filler plays a crucial role in the filler dispersion in the matrix and eventually the interfacial adhesion between the two phases. Much of the mismatch issue arises due to the hydrophobic nature of several polymer matrices [2]. Degassing is another major problem while synthesizing a nanocomposite as once the air is trapped during processing; the final product contains pores and gas bubbles which potentially can initiate crack and failure of specimen under low strains [3].

A significant enhancement of the properties of composites has been achieved by a very low nanofiller content, which has been credited to the incredible surface area availability of the nanofiller and also to their high aspect ratio. However, improvement in the properties by nanofillers to theoretical expectations is still a big challenge since i) uniform dispersion of nanofiller in polymers is not an easy task, ii) an adequate interfacial adhesion between matrix and nanofiller is a big hurdle and most importantly, iii) alignment of nanofillers can be hardly reached. Theoretical modelling and computational simulations have indicated the significant advantages that could be achieved by aligned nano-scale fillers in certain directions in polymer matrices. Till date many researches have been conducted to develop methods for aligning carbon nanofillers (mainly carbon nanotubes (CNTs) and graphene nanosheets) in polymer matrix and incredible improvements in mechanical and functional properties have been reported as compared to randomly-dispersed carbon nanofillers [4-8]. Various approaches have been proposed in order to align fillers in polymer matrices such as shearing [9], electrically induced fields [10-12] and magnetically induced fields [13-16]. Alignment of nanofillers in an electrical field is considered as an effective method but the limitation comes from the fact that this technique can only be applied to materials with very low electrical conductivity, since the field strength is normally restricted to evade the dielectric breakdown of the polymer [17]. On the other hand, low magnetic susceptibility of fillers means strong magnetic field (25T or more) is normally required to align nanofillers like CNT and graphene, thus limiting the practical application of such methods [14-16, 18]. Lastly, simultaneous dispersion and alignment can be obtained using mixing equipment with high shear forces. Unfortunately, these forces are either not large enough to break and disperse the nanofillers in the polymer matrix. On the other hand, high shear has the disadvantage to degrade both the polymer and nanofiller [19].

The object of this thesis is the development of new multifunctional epoxy/glass structural composites containing graphene oxide (GO) or reduced graphene oxide (rGO) nanoparticles. An alternative method to align GO or rGO nanoparticles in the composites is proposed. In this method, continuous fibers are coated with nanofillers by a method termed as electrophoretic deposition (EPD). This method offers the opportunity that any substance (dissolved in a solvent with a particular charge) can be forced to deposit on a substrate by the application of an external applied electric field through a combination of electrodes. Such coated fibers were subsequently used in combination with an epoxy matrix to obtain both single-fiber microcomposites and unidirectional composites with high fiber volume fraction. As per author's knowledge, there has not been much of research conducted in forming composites with coated fibers with different types of graphene nanosheets and subsequently using them as reinforcement in polymer matrix. Hence, this work demonstrates the use of EPD technique to coat different continuous reinforcements (glass fibers and basalt fibers) with graphene nanosheets (graphene oxide and reduced graphene oxide). A bicomponent epoxy resin was used as a matrix to produce hybrid composites. Finally, main goals of this work are as follows:

- Understanding the behavior of deposition parameters on the final coating observed on fibers and consequent effect(s) on the fiber-matrix interfacial adhesion due to induced graphene coating.
- Realizing the possibility of creating electrically and thermally conductive composites by making the graphene coated fibers reduced through chemical means.
- Using the conductive composites to analyze and evaluate the likelihood of having multifunctional properties, namely thermal behavior, strain monitoring and electromagnetic interference shielding effectiveness.

Using thermal analyses techniques (like differential scanning calorimetry and and thermogravimetric analysis), thermal behavior and stability results were used to characterize the epoxy matrix. The oxidation level of both produced GO and rGO were analyzed by x-ray diffraction (XRD), x-ray photoelectron spectroscopy (XPS) and Fourier transform infrared spectroscopy (FTIR). The morphological observation of graphene nanosheets, coated fibers and fractured hybrid composites was carried out by field emission scanning electron microscopy (FESEM). Mechanical properties of fibers, composites and epoxy cured polymer were investigated by uniaxial tensile tests. The fiber/matrix interfacial shear strength of different single fiber composites was evaluated by the single-fiber fragmentation test. Different electrical resistivity measurement methods were employed depending on the electrical behavior of the investigated materials. Multifunctionality hence created (due to the presence of a conductive interphase of rGO) was analyzed by testing the composites for various applications. Composites having conducting behavior were subjected for their piezoresistive behavior in which the change of absolute resistance was monitored while applying longitudinal strain simultaneously. Moreover the capacitive properties or permittivity was also measured by using an LCR meter. In addition, thermal conductivity was also measured to prove the effectiveness of a continuous interphase in epoxy/glass composites.

Chapter 2 – Background

2.1 *Fiber-reinforced polymer composites (FRPC)*

An important type of composite materials, called fiber-reinforced composites, consist of two main constituents namely fiber and matrix. A fiber possesses high strength and modulus and it is bonded and/or embedded in a matrix. Between these two phases a distinct boundary can be identified (interface) or in some cases a third phase (interphase) can be observed between them. Structurally, fibers act as the principal load-carrying components bearing most of the stresses experienced by the structure, while the surrounding matrix not only binds these fibers in the preferred location and alignment, but also serves as a protecting medium from external damage and, most importantly, transfers all the load sustained by the composite to the reinforcing fibers. Both constituents are able to retain their physical and chemical state but nevertheless their combination yield a material having properties that either of the constituent cannot offer acting alone. Therefore, the synergy between components serve some vital roles in a fiber-reinforced composite material to generate a properties profile useful in several structural applications.

The history of fiber-reinforced polymer composites (FRPC) can be traced back to thousands of years ago [20], however the modern world saw the use of composites first in aeronautical and aerospace applications, like airplanes and spacecraft in the 1960s. This limited application of composites appeared due to the fact that earlier, composites had a high manufacturing cost over metals. However, advances in computer-aided manufacturing techniques and other factors made composites components more cost effective than before [21]. Imaginably, the most prominent applications of polymer based composites are in large volume industrial fields, such as automotive, civil constructions, naval, wind energy and sporting goods.

2.1.1 Role of fiber reinforcement in FPRC

The basic and important engineering properties of composites are a collective result of the mechanical and physical properties of the reinforcing phase. These are normally termed as fiber-dominated properties of the composites. For instance, an increase in fiber volume fraction results in higher level of mechanical properties but a point is reached where an increase in the fiber volume fraction is useless because of the insufficiency of the matrix material to hold the fibers and efficient transfer of the load. Careful attention should be given to the selection of fiber type, fiber length, fiber orientation and fiber volume fraction since a variety of composite properties and characteristics are influenced by it, like density, fatigue strength, tensile and compressive strengths and moduli etc. Various commercially available fibers and their properties are summarized in **Table 2-1**.

2.1.2 Role of matrix in FPRC

Matrix imparts the critical role of providing the composite with damage tolerance, toughness, impact and abrasion resistance. Selection of matrix has a great influence in dictating the final properties of the composite material (e.g. compressive, interlaminar shear strength and in-plane shear properties). During compressive loading, the continuous matrix phase offers a lateral support against the fiber buckling thus resulting in the compressive strength of the composite material. The interlaminar shear strength (ILSS) is an important property in composite materials if designed specifically for bending loads. Likewise, in-plane shear strength is considered major factor while designing a composite material for structures under torsional loading. Moreover, the processing methodology and defects in composite materials largely depend on the processing characteristics of the matrix [22].

There are two types of polymeric matrices used for advanced composites, termed as either thermosets or thermoplastics:

Thermosets are low molecular weight and low viscosity monomers (≈2000 centipoise) that are cured into three-dimensional crosslinked structures hence becoming infusible and insoluble. Chemical reactions promote crosslinking (**Figure 2.1**) driven by heat generation either by the chemical reactions, exothermic heat of reaction, or by an externally supplied heat. A range of thermoset resin matrices are normally used in advanced composite materials including epoxides, vinyl esters, polyesters and bismaleimides, a broad information about the thermosets is given in **Table 2-2**.

i) On contrary, *thermoplastics* are linear or branched polymers which are not chemically crosslinked. They do possess high molecular weights and can be melted, fused, and then cooled again to any desire shape but due to their high viscosity and high melting points, high temperatures and pressures are typically required for processing.

Table 2-1. Properties of selected commercial reinforcing fibers [23].

Fiber	**Typical Diameter (μm)**	**Density (g/cm^3)**	**Tensile Modulus (GPa)**	**Tensile Strength (GPa)**	**Strain-to-Failure (%)**	**Coefficient of Thermal Expansion (10^{-6} /°C)**	**Poisson's Ratio**
Glass							
E-glass	10 (round)	2.54	72.4	3.45	4.8	5	0.2
S-glass	10 (round)	2.49	86.9	4.30	5.0	2.9	0.22
PAN carbon							
T-300[a]	7 (round)	1.76	231	3.65	1.4	-0.6 (longitudinal) 7-12 (radial)	0.2
AS-1[b]	8 (round)	1.80	228	3.10	1.32		
AS-4[b]	7 (round)	1.80	248	4.07	1.65		
T-40[a]	5.1 (round)	1.81	290	5.65	1.8	-0.75 (longitudinal)	
IM-7[b]	5 (round)	1.78	301	5.31	1.81		
HMS-4[b]	8 (round)	1.80	345	2.48	0.7		
GY-70[c]	8.4 (bilobal)	1.96	483	1.52	0.38		
Pitch carbon							
P-55[a]	10	2.0	380	1.90	0.5	-1.3 (longitudinal)	
P-100[a]	10	2.15	758	2.41	0.32	-1.45 (longitudinal)	
Aramid							
Kevlar 49[d]	11.9 (round)	1.45	131	3.62	2.8	-2 (longitudinal) 59 (radial)	0.35
Kevlar 149[d]		1.47	179	3.45	1.9		
Technora[e]		1.39	70	3.0	4.6	-6 (longitudinal)	

Extended chain polyethylene							
Spectra 900[f]	38	0.97	117	2.59	3.5		
Spectra 1000[f]	27	0.97	172	3.0	2.7		
Boron	140 (round)	2.7	393	3.1	0.79	5	0.2
SiC							
Monofilament	140 (round)	3.08	400	3.44	0.86	1.5	
Nicalon[g] (multifilament)	14.5 (round)	2.55	196	2.75	1.4		
Al_2O_3							
Nextel 610[h]	10-12 (round)	3.9	380	3.1		8	
Nextel 720[h]	10-12	3.4	260	2.1		6	
Al_2O_3-SiO_2							
Fiberfrax (discontinuous)	2-12	2.73	103	1.03-1.72			

[a] Amoco

[b] Hercules

[c] BASF

[d] DuPont

[e] Teijin

[f] Honeywell

[g] Nippon Carbon

[h] 3-M

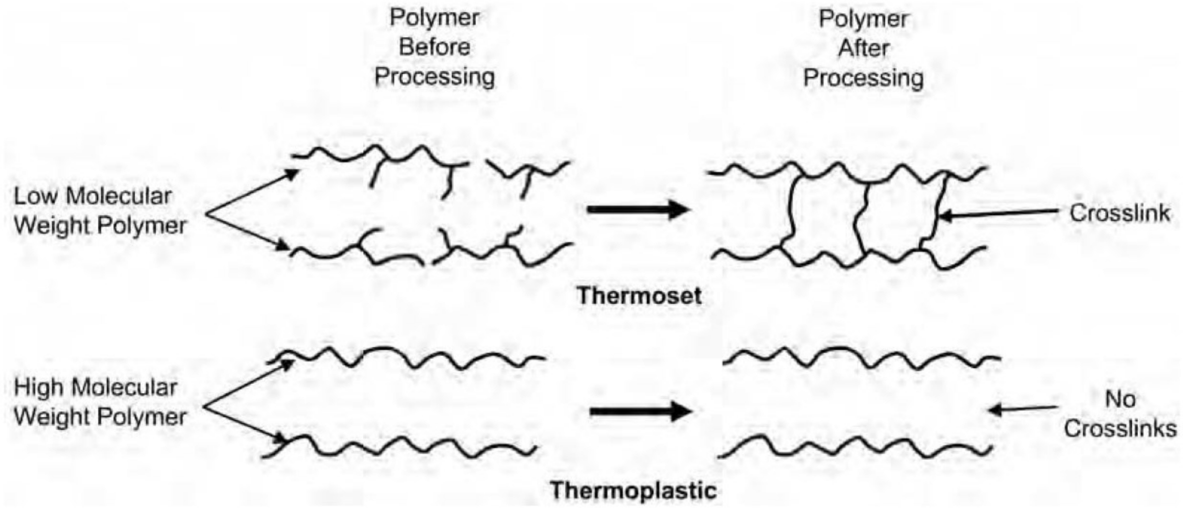

Figure 2.1 Comparison of thermoset resins and thermoplastic polymer structures.

2.1.3 Interface and interphase in FPRC

A definition of *interface* in fiber reinforced composites can be given as "a surface formed by a common boundary between reinforcing fiber and matrix that is in contact with and maintains the bond in between for the transfer of loads" [23]. The physical and/or mechanical properties of an interface may be different from either from that of the fiber or the matrix. On the other hand, an *interphase* could be defined as a region of finite dimensions between the fiber and the matrix where the local properties vary from those of the bulk phases [24, 25]. The physical, chemical and/or mechanical properties differ either continuously or in gradual manner between the bulk fiber and matrix material.

Table 2-2 Comparison of thermoset resin matrices [22].

Epoxies	High-performance matrix systems for primary continuous-fiber composites. Can be used at temperatures up to 250–275 °F. Give better high-temperature performance than polyesters and vinyl esters.
Phenolics	Though difficult to process, resin system with higher thermal stability with good smoke and fire resistance. Mostly used for aircraft applications.

Polymides	Very-high-temperature resin systems (280–310 °C). Difficult processing.
Polyesters	Extensively used in commercial applications due to low cost and processing flexibility. Used for both continuous and discontinuous composites.
Vinyl Esters	Relatively similar to polyesters but are more tough and have better moisture resistance.
Bismaleimides	Epoxy-like processing, high-temperature resin matrices for use in the temperature range of 135–180 °C and possesses elevated-temperature post cure.
Cyanate Esters	Epoxy-like processing, high-temperature resin matrices for use in the temperature range of 275–180 °C and possesses elevated-temperature post cure.

A growing research interest has emerged in various research groups to understand the impact of interphase's physical structure and chemical composition on the final composite properties. In fact, the properties of interphase have a great effect on the way the fiber-matrix interact with each other and consequently the mechanism of stress transfer from matrix to fiber is defined. In addition, the substantial interfacial area between the reinforcements and matrices pave the way to various and elusive effects on the composites properties. Not to forget that since the debonding phenomenon is one of the main mechanisms responsible of composites failure, the ability to counter this problem by its early detection during service conditions and healing as well has become a major challenge in the research field.

The stability of FRPCs greatly depends on the interfacial interaction or adhesion between fiber and matrix phases. For an interfacial adhesion to be termed as good, there should be a gradual transition of filler/reinforcement to matrix properties [26]. However, certain design models are used to fabricate the interphases in composite materials. For example, in order to achieve higher strength and stiffness values, a strong interfacial bonding is recommended while on the other hand, weak interphases are necessary to ensure better energy absorbing performances under impact conditions [27]. The main characteristics of fiber-matrix interactions have been presented in the literature since its evolution i.e. physico-chemical or frictional in nature [28]. The first category include intermolecular interactions, chemical reactions, surface-induced crystallizations and phase separation phenomena etc. while the latter consists of surface roughness of the fibers. Although, both types of interactions are responsible to some degree in the mechanics of composite materials but normally are not mentioned in detail [27].

Overall, the interphase has become a key factor to dictate the composite performance as it enables the scientists and engineers to manipulate it while considering the parameters of the service conditions in which the composite material will be used.

2.2 Mechanical properties of fiber reinforced polymer composites

The selection of a specific material for a structural engineering application is based mainly on its behavior under tensile, shear, compressive or other static or dynamic mechanical loading conditions. Therefore, not only the selection of material is of prime importance but also designing the structure for the particular application. The orthotropic nature of fiber reinforced polymer composites has resulted in the development of test methods based on specific standards which are totally different from those traditionally adopted for isotropic materials.

2.2.1 Interfacial adhesion between fiber and matrix

As discussed in section 2.1.3, the role of interface/interphase is considered to be one of the critical aspects in engineering the mechanical properties of composite materials. Since the role of matrix and fiber are both interrelated to each other hence it is of prime importance that the interfacial adhesion between fiber and matrix has sufficient strength to be able to transfer the load from one to another.

In literature, several different methods have been reported for measuring the level of stress state and strength of the interfacial bond. One of the most common methods for measurements of fiber-matrix adhesion is the single fiber fragmentation test. Although this was first developed for metals [29], it has been adopted for determining the interfacial shear strength in advanced polymer composites.

2.2.1.1 Single-fiber fragmentation test

A micromechanical testing with fewer parameters [30], known as single-fiber fragmentation test, was developed to evaluate the level of adhesion between a fiber and matrix. As the name implies, the test consists of a composite specimen containing a single fiber embedded in the middle of a matrix as shown in the **Figure 2.2**.

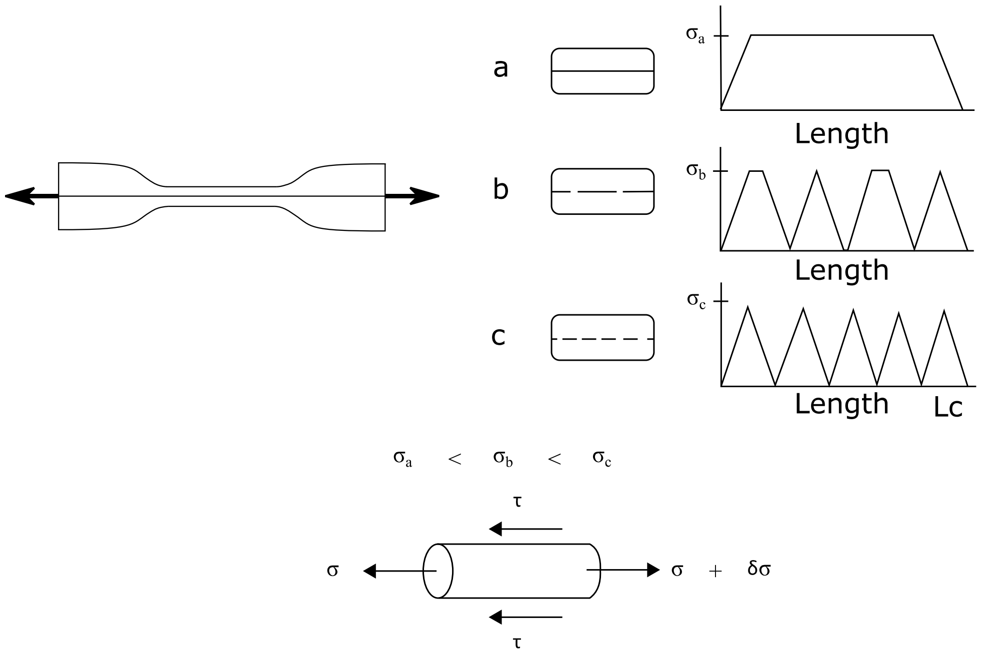

Figure 2.2. Schematic diagram of single fiber fragmentation test.

As evident in the figure, the testing condition is based on applying a tensile load on the composite specimen (a) until the strength of the fiber is reached upon which the fiber ruptures at a point where the stress concentration is high enough. Continuing the tensile loading would result in other points being ruptured, as described as fiber fragmentation (b). A point comes where the load transferred from the matrix to the fiber is not enough to break the fiber into smaller fragments; hence the saturation of fragmentation is achieved (c). The length of the resultant fiber fragments is termed as fiber critical length (l_c), which can be used to calculate the interfacial shear strength (IFSS or ISS) as given by the work of Kelly and Tyson [29]:

$$l_c = \frac{d\sigma_f}{2\tau} \tag{2-1}$$

where d is the fiber diameter and σ_f is the tensile strength of the fiber at critical length, and τ is the shear stress transferred from the matrix to the fiber. This latter can be evaluated by considering Weibull distribution for the fiber strength i.e.:

$$\sigma_f = \sigma_0 \left(\frac{L_c}{L_0} \right)^{-\frac{1}{m}} \Gamma\left(1 + \frac{1}{m} \right) \tag{2-2}$$

where Γ is the Gamma function whereas σ_0 and m are the scale and shape parameters of the Weibull strength distribution at the reference length L_0 respectively.

2.2.2 Interlaminar properties

Unidirectional composites with laminated structures demonstrate excellent in-plane properties however at the same time they exhibit poor interlaminar properties. The reasons could be either a lack of reinforcement in the thickness direction or poor interfacial adhesion between laminas or even both. In any way, this may lead to poor damage tolerance when composites are subjected to interlaminar stresses. One way to look into this problem is that the continuous fibers aligned in the composite structure display highest strength and modulus in the fiber direction. This reinforcement is absent in the thickness direction of the composite structure which is only reinforced by the combination of, i) bonding between fiber and the matrix and ii) the strength of the matrix, which in total as compared to the mechanical properties of the fibers is extremely low. The most common failure case observed due to this issue is the failure between laminas or delamination.

One of the common methods to avoid interlaminar failure is based on using fiber fabrics having 3D ply stitching thus providing with through thickness reinforcement, however such approach leads to reduction of in-plane mechanical properties and also an increase of production cost [31]. The other tactic involves using different types of nanofiller thus providing the opportunity of 'interlocking' the laminates hence improving the interlaminar properties like ILSS, fracture toughness, flexural properties etc. [32-35]. ILSS depends primarily on the matrix properties and fiber-matrix interfacial shear strength, whereas the fiber properties have no influence on the final ILSS.

2.2.2.1 Short beam shear (SBS) test

This test involves three point bending test loading of a specimen having a small span to depth ratio in a configuration in order to produce a horizontal shear failure between the laminas (**Figure 2.3**). To understand this test, consider the following beam equations:

$$\text{Maximum normal stress } \sigma_{xx} = \frac{3PL}{2bh^2} = \frac{3P}{2bh}\left(\frac{L}{h}\right) \tag{2-3}$$

$$\text{Maximum shear stress } \tau_{xz} = \frac{3P}{4bh} \tag{2-4}$$

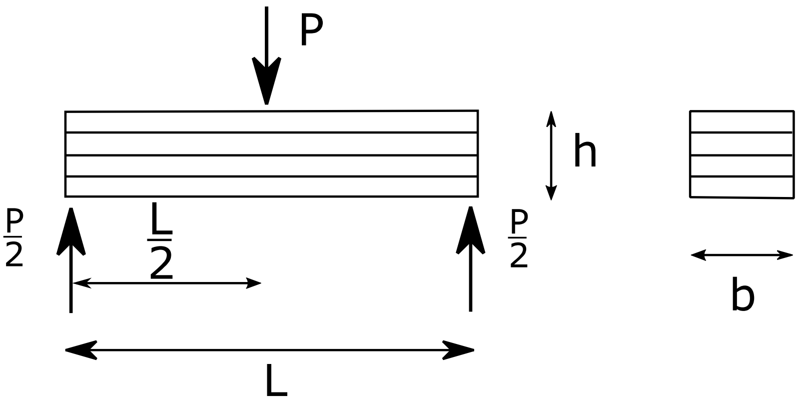

Figure 2.3. Schematic diagram of composite panel in 3 point bend test mode for short beam shear strength test.

As it can be visualized from the Equation 2-3, the maximum normal stress depends on the L/h ratio while the maximum shear stress does not depend on the L/h factor. Thus when very small (3 to 4) L/h ratios are used, the failure most likely occurs for shear in the neutral plane (see **Figure 2.4**) and the corresponding interlaminar shear strength (ILSS) value is evaluated as the maximum shear stress in the beam. These SBS tests are regulated by ASTM standard D2344.

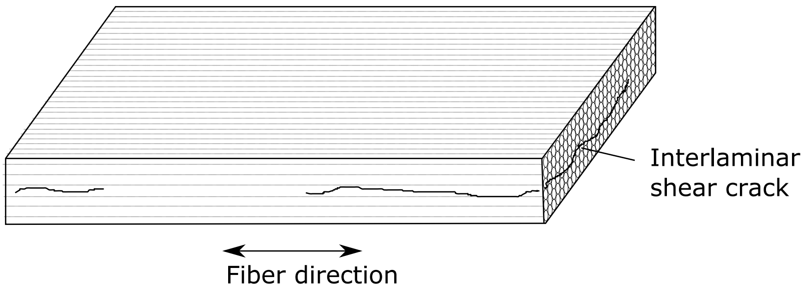

Figure 2.4. Interlaminar shear failure in a 0° laminates in a short-beam shear test [23].

2.2.2.2 Mode I Interlaminar Fracture Toughness (DCB)

This DCB test is employed to determine the strain energy release rate G_I for crack propagation between laminates or delamination growth under Mode I loading. Normally, a unidirectional composite as shown in **Figure 2.5** is used having a rectangular cross section and uniform thickness and width. The specimen contains a started crack (delamination) generated by the insertion of a thin Teflon film (typically 0.013 mm thick) in the midplane during composite lamination. Load is applied through the metal hinges which hold the two beams until the initial crack grows slowly by a predetermined length. The specimen is unloaded and then reloaded until the new crack in the specimen grows slowly by another predetermined length. The load, crosshead displacement, crack opening displacement and delamination length are recorded continuously during the test. The delamination length is determined by considering the distance from the loading line to the edge of delamination. The initiation and propagation value of G_{Ic} can be measured by considering the recorded data and evaluating it with a beam theory and compliance calibration methods.

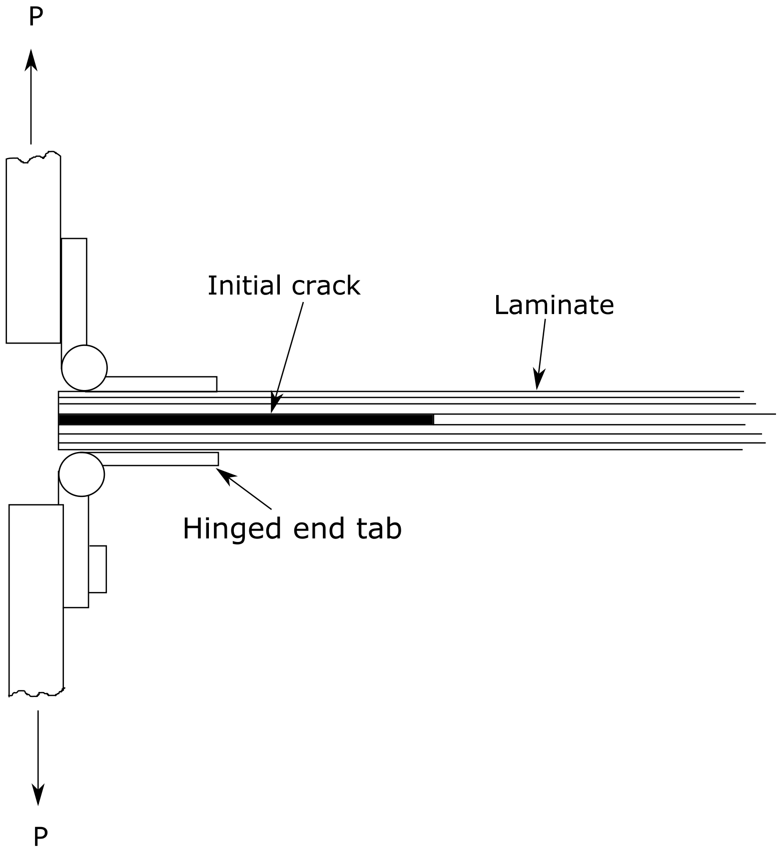

Figure 2.5. Double cantilever beam specimen under opening mode fracture configuration.

According to the standard (ASTM 5528), three data reduction methods are recommended as, i) Modified Beam Theory (MBT) method, ii) Compliance Calibration (CC) method, and iii) Modified Compliance Calibration (MCC) method. The only difference in these methods is the models used for determination of compliance on the bases of crack length.

i) MBT method:

Under this method, the specimen having a crack consists of an upper arm and lower arm which can be assumed as two cantilever beams with a distance Δ in front of the crack tip as shown in **Figure 2.6**.

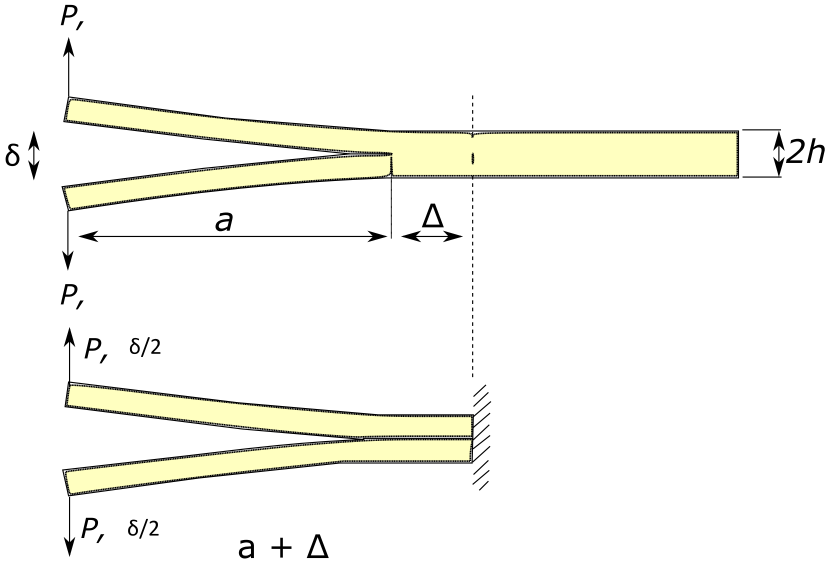

Figure 2.6. Schematic diagram of the DCB specimen (side view).

According to Euler-Bernoulli beam theory, the estimate compliance can be considered as a polynomial of third order as given as:

$$C = m^3 (a + \Delta)^3 \tag{2-5}$$

Using the Strain energy release rate (SERR)-compliance relation given by following equation:

$$G = \frac{P^2}{2b} \frac{dC}{da} \tag{2-6}$$

the equation 2.5 can be written as:

$$G_1 = \frac{3P\delta}{2b(a + \Delta)} \tag{2-7}$$

where

P = Load
δ = total crack opening displacement
b = specimen width
a = length of delamination
C = compliance and defined by δ/P.

The parameter Δ is determined experimentally by the x-intercept of a straight line fit by the least squares to $C^{1/3}$ versus a data as shown in **Figure 2.7**.

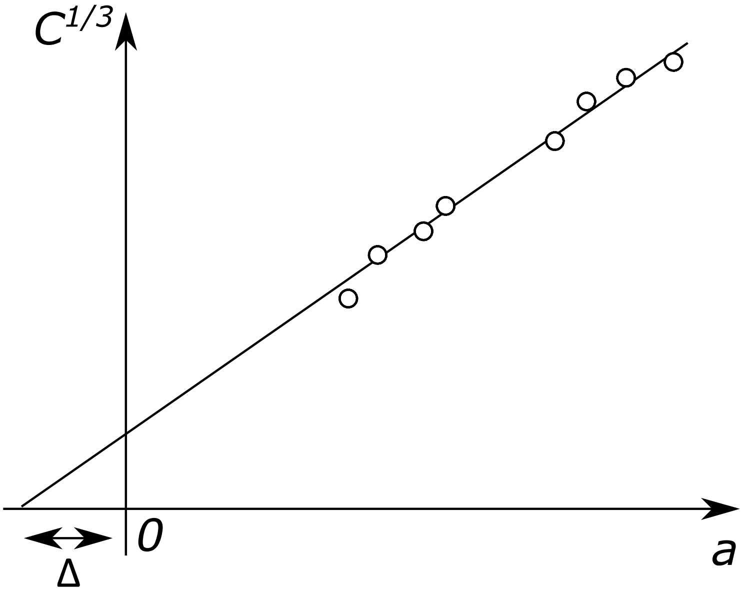

Figure 2.7. Evaluation of Δ according to modified beam theory (MBT).

ii) CC method (Berry's method)

In consideration of the simple beam theory model, the deflection of the tip of a cantilever, υ , with the length, a , can be assumed as:

$$v = \frac{Pa^3}{3EI} \tag{2-8}$$

For a double cantilever beam, the end deflection is assumed to be related to the load by:

$$\delta / 2 = RPa^n \tag{2-9}$$

Therefore, the predicted compliance can be described with the following equation:

$$C = Ra^n \tag{2-10}$$

Finally, the strain energy release rate G_I may thus be given as:

$$G_I = \frac{nP\delta}{2ba} = \frac{nP^2Ra^{n-1}}{2b} \tag{2-11}$$

Here, n is the experimentally determined by slope of the straight line drawn between the natural logarithm of compliance C and natural logarithm of crack length a as shown in **Figure 2.8**:

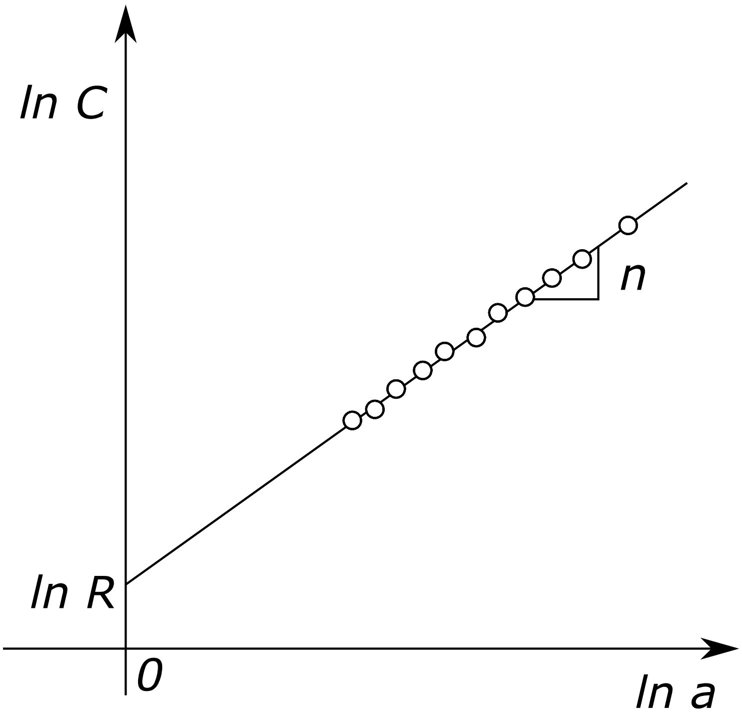

Figure 2.8. Determination of n in compliance calibration (CC) method.

iii) Modified Compliance Calibration (MCC) method

In this method, the normalized compliance is taken into consideration and is related to the normalized delamination length given as $a/2h$:

$$a/2h = \alpha_1 (bC)^{1/3} + a_0 \tag{2-12}$$

Here, a_1 can be determined experimentally by the slope of a straight line that has been fitted to a plot of $a/2h$ versus $(bC)^{1/3}$ data as shown in **Figure 2.9**:

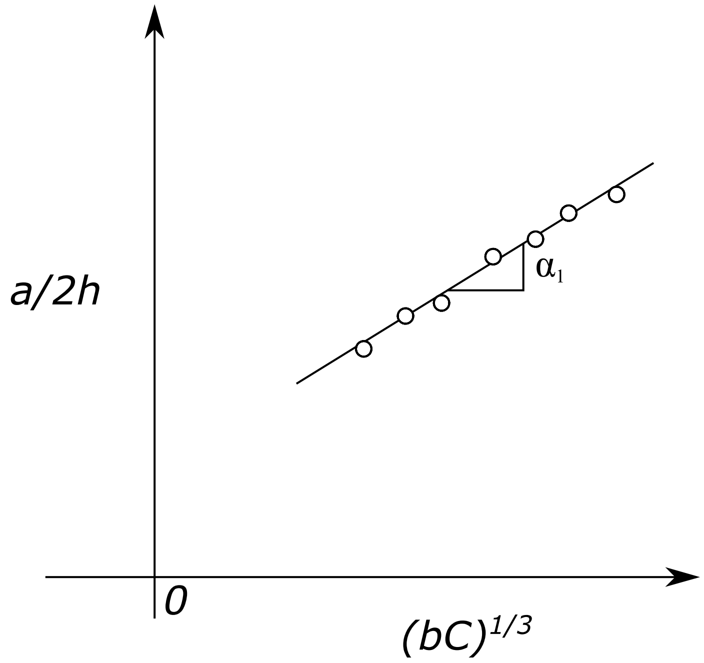

Figure 2.9. Determination of α_1 according to modified compliance calibration (MCC).

Again, using the expression for SERR based on the MCC method G_I is given by:

$$G_I = \frac{3P^2C^{2/3}}{2\alpha_1 b^2(2h)} \tag{2-13}$$

An estimate of the coefficient α_1 and α_0 is given by following equations respectively:

$$\alpha_1 = \frac{\sqrt[3]{E_1}}{4} \tag{2-14}$$

$$\alpha_0 = \frac{-1}{2}\left[\frac{E_1}{11G_{13}}\left\{3-2\left(\frac{\Gamma}{1+\Gamma}\right)^2\right\}\right]^{1/2} \tag{2-15}$$

Where, Γ is:

$$\Gamma = 1.18\frac{\sqrt{E_1 E_3}}{G_{13}} \tag{2-16}$$

Here, E_1, E_3 and G_{13} represent longitudinal Young's modulus, through thickness Young's modulus and transverse shear modulus respectively.

2.2.3 Flexural properties

Flexural stiffness and strength are particularly important properties of resins and laminated fiber composite materials and the use of flexural tests to determine these mechanical properties is widespread in the industry.

2.2.3.1 Three point bending test

For a unidirectional composite, the material properties are considered to be uniform through the thickness of the specimen due to isotropic nature. The normal stresses under such circumstances varies linearly from a maximum in compression on one surface to an equal maximum in tension on the other surface, passing through zero at the mid-plane as known as neutral axis as shown in **Figure 2.10**. Here, the maximum normal stress is given as:

$$\sigma = \frac{6M}{bh^2} \tag{2-17}$$

here M is the bending moment, b and h are the specimen's width and thickness, respectively. The distribution of shear stress through the thickness is however parabolic in nature being maximum at the neutral axis and zero at the outer surfaces of the structure, where maximum value is considered as:

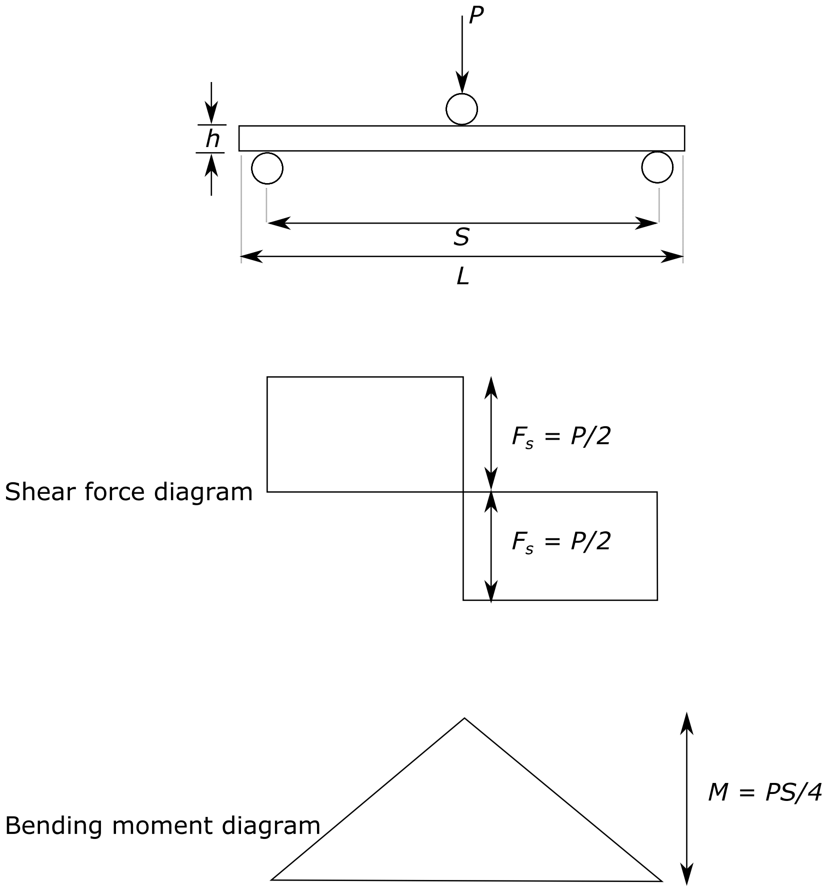

Figure 2.10. Three-point flexure test, together with shear force and bending moment diagrams.

$$\tau = \frac{3F_s}{4bh} \tag{2-18}$$

where F_s is the shear force acting on the specimen's cross-section.

Figure 2.11 shows the variation of normal stresses and shear stress caused by bending moment for a rectangular specimen having a regular cross-section.

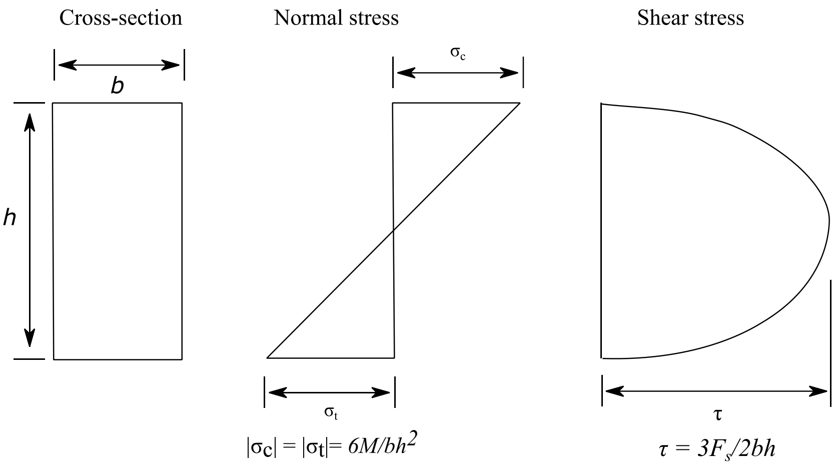

Figure 2.11. Variation of normal stress and shear stress in a flexural test.

In such case, a homogeneous elastic material tested in flexural mode by applying a load at midpoint and supported at two points experiences maximum stress in the outer surface of the test specimen occuring at the midpoint. Hence, flexural stress is obtained using the equation [ASTM D790]:

$$\sigma_f = \frac{3PL}{2bd^2} \tag{2-19}$$

In addition, the tangent modulus of elasticity (often referred as the "modulus of elasticity") is the ratio of stress to corresponding strain within the elastic limit. It is measured by drawing a tangent to the steepest initial straight-line portion of the load-deflection curve and using following equation [ASTM D790]:

$$E_B = \frac{L^3 m}{4bd^3} \tag{2-20}$$

2.3 "Smart" multifunctional hybrid composites

Recent years have seen a remarkable interest in research and development of multifunctional composites especially involving polymer nanocomposites. A multifunctional composite simply refers to a structure that has the capability to perform structural and non-structural functionalities together. These materials are lightweight, chemically stable and mechanically strong and may find utility in various civil and military engineering applications. In recent years, these materials are being engineered to obtain functional properties which could offer active, sensory and adaptive capabilities. The goal in the development of such materials is to realize the multifunctionality by such composites structures without compromising the structural integrity.

These systems, also known as ‘active’ or ‘smart’ materials, possess the capability of detecting environmental changes and/or external stimuli at the most optimum conditions as well as to respond in accordance to the modifications taking place. The most popular way to create these systems is by the incorporation of nanophases that could enhance the mechanical properties by some definite and specific mechanisms and/or introduce new functionalities leading to novel and innovative non-structural properties. On the other hand, a traditional material, which can be either structural or non-structural, is categorized based on its properties which ultimately define its use in the application field. However due to its inactive behavior for not being able to sense the external stimuli hence render them ‘passive’ materials.

It is worthwhile to mention here that the “intelligence” of the multifunctional materials is not totally related to the embedment of electronic devices within the structure, while materials with sensors built-in are also an important group of multifunctional composites. However, multifunctionality can be achieved by integrating specific constituents or mechanisms determined by their own functional or non-functional properties that could be activated only in specific loading conditions or as a response to particular surrounding changes. In other words, the smartness of material is typically associated to its ability to correspond information with the external environment thus offering new mechanisms and capabilities to enhance the non-structural performance of the materials itself.

In recent years, nanomaterials have prompted the field of “hybrid” or “multiscale” polymer composites, due to their ability, but not limited to, of improving the conventional structural properties of composites, but also of inducing functionalities in the structures as well. Nanoscale reinforcements (such as CNTs, graphene, etc.) when added in simple polymer matrix or fiber reinforced polymer matrix have shown to create novel hybrid structures. Creation of such multiscale composites, for getting the optimum level of advantages from the use of nanomaterials in conventional fibrous composites, can be achieved through three different techniques [36]:

1. Dispersion of nanomaterial into the matrix also known as nano-augmentation.
2. Creating organized structures of nanomaterial on to the composite laminates also known as nano-engineering.

3. Designing of multiscale hybrid composite using different numerical tools starting from the molecular dynamic up to macroscale multi-physics also known as nano-design.

In order to obtain required functionalities from a smart material, certain features are required to be incorporated into such smart materials which are defined as follows:

- *Sensing:* External gadgetries like sensors are basically paired to the structure of the material of interest to monitor and/or measure the intensity of an external stimulus. Such sensors have the ability to convert an external physical input and convert the reading into a signal that can be visualized and monitored by instrumentations like signal processing and signal interpreters. Quantities that can be monitored in this way include temperature, pressure, strain, acceleration etc.
- *Actuation:* It is a hydraulic or electrical motion device that has the ability to perform actions such as motion or spark other specific devices. Like sensors, these are directly attached with the composite structure and responds to an external signal (like electricity or heat).

2.3.1 Non-structural functionalities

Functionalities other than structural ones that are being made possible by the creation of hierarchical composites using nano-reinforcements can be described, but not limited to, as electrical conductivity, thermal conductivity, piezoresistivity, dielectricity and electromagnetic interference shielding (EMI).

2.3.1.1 Electrical conductivity

One of the utmost requirement generally pursued in a multifunctional structure is the electrical conductivity due to the fact that in general polymers and glass-fiber reinforced polymer composites are poor conductors of both electricity and heat. The addition of conductive nanofiller has a strong effect on the overall conductivity of such insulating composite materials. Low filler loadings do not improve the electrical conductivity of the polymer matrix. However, at a particular or above a critical filler concentration the conductivity rises by several orders of magnitude. At this critical level of loading, also known as percolation threshold, a continuous and conductive network is created in the composite structure. The resultant conductive composite structures have fascinated researchers as wide array of applications because of this property arise like damage detection, structural health monitoring and electromagnetic interference shielding which will be discussed in following sections.

A possible application of such functionality in a load-bearing structure can be found in aerospace industry where the conductive polymer composites could replace non-conductive materials to improve the lightning protection of the structures. Being lightweight in nature, polymer nanocomposites are favorites to replace the add-on metallic conductors in the aircraft structure for such purpose since they not only increase the weight but also are difficult to repair [37]. Recent reports on incorporation of graphene in fiber reinforced polymer composites has resulted in an increase in electrical conductivity of the hybrid structure. For example, Wenzhen et al. [38] coated carbon fibers with graphene nanoplatelets (GnP) using a continuous solution coating process and its subsequent epoxy based reinforced composite showed an increase in electrical conductivity as compared to its counterpart composites without GnP interphase.

2.3.1.2 Thermal conductivity

The necessity of increasing the thermal conductivity of engineering materials comes from the fact that advanced miniaturized devices and electronics have become not only faster but also denser hence resulting in an increase of power dissipation and consequently the production of large thermal fluxes [39, 40]. Thus the utmost priority in such devices is to have an efficient system of heat dissipation in order to guarantee highest reliability as well as high performance. Recent years have seen reports on the synergistic effect of nanosized fillers (e.g. CNTs, graphene) on the thermal properties of composites. The high thermal conductivities of such nanofillers have shown an increase in thermal conductivity of polymer composites however there are many limitations that are associated with the nanofillers which result in underachievement of the required properties in polymer composites. Unlike electrical conductivity, thermal conductivity does not manifest the ‘percolation threshold’ of the filler loading. In fact it generally increases almost linearly with respect to filler loading, as reported by Shenogina et al. [41].

The efficient loading of nanofiller (maximum dispersion, unidirectional alignment and continuous network) would also dramatically enhance the conductive ability of the polymer composites. Moreover, better compatibility between filler and matrix would minimize the contact resistance and interfacial phonon scattering [42-46] and hence an improvement in thermal conductivity could be achieved.

2.3.1.3 Piezoresisitivity

One of the most sought features of conductive polymer composites is piezoresistivity, which can be described as the change in resistance of a given material under the application of mechanical strain. When this effect is induced in composite systems they can find applications in which in-situ strain monitoring of the structure can be performed while in service. The creation of electrically conductive polymer systems by the incorporation of conductive phase like stainless steel fibers, nickel-coated graphite, coated glass fibers and carbon nanoparticles in non-conductive polymer phase has paved the way to achieve different type of material systems with varying properties as well as the useful functionality of strain monitoring.

The phenomenon of piezoresistivity in heterogeneous composite systems can be attributed to various mechanisms as listed below:

- degradation or breaking of conductive network of nanofiller [47].
- variation of inter-filler distance hence the change in tunneling resistance [48].
- decrease in the conductivity of nanofiller under applied stress [49].
- increase or decrease in alignment of nanofiller under applied strain [50].

The metallic strain gauges used in the modern day applications have low gage factors (2-5) and consist of low resistance elements. Although these gages have good sensitivity and are relatively inexpensive, however they cannot be difficulty embedded in structural materials and provide information only on a limited region. Current research efforts have been focused on obtaining structural composites which act as strain gages with superior electromechanical properties. Sensors based on carbon based materials, such as like carbon nanotubes (CNTs) and graphene, have displayed much better efficiency as compared to commercial available sensors because of the use of high elastic modulus and outstanding electrical properties [51-54] and unveil high sensitivity at nanoscale. Even gauge factors (GF) up to 2900 [55] has been achieved for CNTs based strain sensors which is incredibly higher as compared to metal based piezoresistors.

2.3.1.4 Dielectricity

Materials with dielectric properties play a vital role in modern electronics and power systems [56]. The requirement to improve the dielectric properties of materials is motivated by higher function and tremendous miniaturization of electronics in modern world. Basically, dielectric materials have the potential to control and store electrical charges and energies. These are formed by sandwiching a dielectric material between two metal plates as electrodes on which an external electric potential is applied. In this way, the dielectric materials in capacitors store electrical energy due to the charge separation when the atoms and molecules are polarized. However, the small packaging of microelectronic devices have to fulfill different requirements like low dielectric loss, moderate relative permittivity and moisture absorption resistance etc., the spot light is now on polymer based composites since they have the potential to offer functional packages combining electrical properties, mechanical flexibility, chemical stability and their feasibility to be used in applications like capacitors and dielectricity [57, 58].

With the advancement in the processing and utilization of conductive nanofiller in the polymer matrix for functional properties [59-61], such polymer nanocomposites are also being under investigation for their use as dielectric applications. In particular, carbon nanomaterials have shown good promise for their conductive ability for their potential to be used as high dielectric materials (high-*k*) for various applications, such as electroactive polymer and embedded capacitors. The basic principal of high-*k* polymer/filler nanocomposite is based on the conductivity mismatch between filler and matrix. The dielectric properties of nanocomposites are determined largely by the interface nature of filler/matrix, the filler surface area, orientation of nanofiller and inherent conductivity of the fillers [62].

2.4 Graphene – a FLAT-astic nanomaterial

Graphene, the basic building block for all graphitic structures, has gained tremendous attention on the horizon of material science and physics since its discovery in 2004 by the group of Geim and Novoselov [63]. This two-dimensional, monolayer of carbon atoms (**Figure 2.12**) joined together by sp^2 covalent bonds in hexagonal lattice can be wrapped into a zero-dimensional carbon structure (fullerene), or rolled into one-dimensional carbon structure (carbon nanotube) or placed over one-another as the basic natural carbon structure (graphite) [64]. Among many fascinating properties, graphene possesses a large theoretical specific surface area (2630 m^2g^{-1}), exceptional Young's modulus (1.0 TPa) [65], exceedingly high intrinsic electron mobility (200,000 cm2 v^{-1} s^{-1}) [65, 66] and excellent thermal conductivity (5000 Wm^{-1} K^{-1}) [67].

Before the isolation of graphene in 2004, the elementary electronic properties were already calculated on the basis of the simple crystal structure [68, 69]. However, after its discovery, graphene attracted a massive interest from around the world. Applications like high energy physics [70-72], condensed matter systems [73-75], chemical reactions [76-78] and especially electric and photonic devices [79-83] have benefitted a great deal due to the superlative properties of graphene.

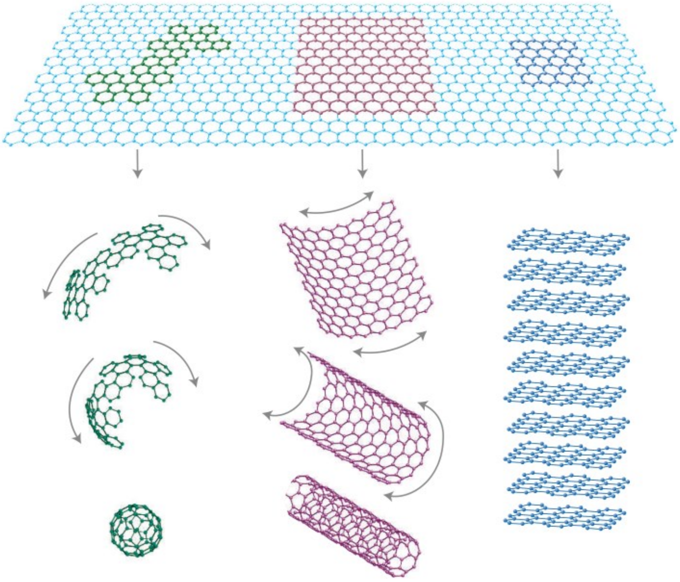

Figure 2.12. Visualization of graphene as mother of all graphitic forms [64].

2.4.1 Classification of graphene

Till date, graphene has been distinguished either by its physical structure or chemical nature.

i) Based on first classification type, four variants of graphene have been defined as single-layer graphene (SG), bi-layer graphene (BG), few-layer graphene (FG) (3-10 layers) and multi-layer graphene (MG) or graphene nanoplatelets (10-100 layers) [84]. Although there isn't any unified theory of exact number of layers beyond which a particular graphene stack acts as graphite however Geim and Novoselov argued that structure consisting of 10 graphene layers demonstrates different electronic properties as compared to graphene [84].

ii) Depending on the chemical nature of the nanosheet, graphene can be either termed as pristine graphene, graphene oxide, reduced graphene oxide or functionalized graphene. For our interest, these are further explained as follows:

2.4.1.1 Prisitine graphene

This terminology is analogous to the term "ideal graphene nanosheet" as it possesses the minimal possible oxygen functionalities, maximum consistent carbon structure and supreme electrical, mechanical and thermal properties. However as like every other "ideal" thing in the world, the production, isolation, placement and utilization of pristine graphene is practically impossible on a large and commercial scale. Although new production procedures are being sought out at laboratory scale however the realization of achieving the large output of such "perfect" nanosheets for practical applications is far from reality.

The first technique presented to isolate a single pristine graphene sheet was by Novoselov and Geim in 2004 by scotch-tape peeling of highly ordered pristine graphene (HOPG) or micromechanical exfoliation [63]. This simple and elegant process offered the researchers to separate the pristine graphene (**Figure 2.13**) on to a different substrate for various characterizations. The obvious difficulties in upgrading this procedure for commercial application have compelled researchers around the world to find its alternative methods. After this, techniques like

In order to gain maximum yield of pristine graphene for large-scale applications, scientists have been able to report, although tedious, but by far better synthesis of pristine graphene in terms of the output of the process. Lots of novel works have been reported developing liquid-phase exfoliation method using ultrasonication technique [85], rotor-stator mixer [86], hydrodynamic force-induced exfoliation [87-90], CVD growth on epitaxial matched metal surface [91-94] or even using toxic organic solvents with high temperature conditions [95]. These methods has enabled the users to obtain high-quality graphene and/or graphene equivalents but with definite problems like low yield, large processing time etc. One of the latest methods being looked after involves supercritical CO_2 fluid due to its nontoxic and low viscous nature along with cheap and non-flammability. Several reports [94, 96-100] have been published in which pristine graphene with different number of layers have been produced using supercritical CO_2, however it seems to be technically impossible to obtain definite number of pristine graphene layers with a single method.

Figure 2.13. First reported single-layer pristine graphene nanosheet as visualized by AFM technique (Adapted from [63]).

2.4.1.2 Graphene oxide

The origin of graphene oxide is derived from graphite oxide which is known to the world of science since mid-1800s. Despite of its old history, the actual structure and composition is still controversial because of its nonstoichiometric composition and strong hygroscopicity of dehydrated graphite oxide [101]. As its name suggests, graphene oxide is basically graphene nanosheet(s) with oxygen atoms covalently attached to its carbon skeleton. The oxygen atoms are, in reality, in the group form as functional groups (hydroxyl, epoxy and carboxy etc.) which render the nanosheet 'active' as compared to pristine graphene. The activeness of graphene oxide nanosheets makes them not only hydrophilic in polar solvents but also due to pertaining negative charges on graphene oxide nanosheets, their high degree of dispersion offers a variety of processing advantages. However the attachment of oxygen functionalities strongly disrupts the delocalized electron network in graphene skeleton thus rendering graphene oxide as an insulator.

Although the discovery of graphene is relatively new, the presence and understanding of GO is quite old whose history dates back to several decades. The earliest well-known example of GO synthesis is when a British chemist B. C. Brodie was conducting experiments on the oxidation of graphite flakes in 1859 [102]. Later, L. Staudenmaier had improved the procedure of oxidizing graphite which resulted in better oxidation and through a simple approach [103]. About 60 years later, two scientists Hummers and Offeman [104] developed the famous oxidation method by reacting graphite with mixture of acids ($KMnO_4$ and H_2SO_4) and paved the way towards a successful and practical oxidation method used till now. Others have developed slightly modified versions but these above mentioned three methods have become the basic routes for synthesizing GO.

2.4.1.3 Reduced graphene oxide

Simply, reduced graphene oxide is obtained when GO is subjected to reduction process i.e., removal of oxygen functionalities from the graphene oxide structure to render it "non-oxidized". Technically, reduced graphene oxide should be equivalent to pristine graphene but not only the reduction process imparts structural defects, such as dislocations, but also the oxygen functionalities do not completely detach themselves from the hexagonal skeleton due to their sp^3 bonding with carbon atoms. Moreover the characterization techniques have revealed the properties of rGO being inferior to pristine graphene obtained by micromechanical exfoliation. Therefore the term 'reduced graphene oxide' is used for these nanosheets obtained through reduction rather than 'pristine graphene' or 'graphene' as well.

Reduction could be achieved through a variety of methods but mainly chemical, thermal or electrochemical pathways have proved to be more efficient and suitable for a large scale application process.

- The dispersion of GO in any solvent can be easily subjected to a chemical reduction process. The first and the most common usage of a chemical to carry out reduction is hydrazine monohydrate due to the non-reactive nature to water (as opposed to other strong reductants) [105]. Other chemicals like hydroquinone, sodium borohydride and strong alkaline solutions have shown mixed results, however this process comes with a danger to human health due to the hazardous or carcinogenic nature of these chemicals.
- Removal of oxygen-based functionalities from the graphene oxide surface is also possible through thermal means. By treating a GO sample in a furnace at temperature above 1000°C, carbon dioxide gets released which enforces the exfoliation of the stacked structure of GO with pressures ranging around 130 MPa [106]. The release of CO_2 gases consequently results in the reduction of the graphene oxide where the bulk conductivities reported were in the range of 1000 – 2300 S m^{-1} [107]. The noticeable drawback of this process is the

structural damage hence creating vacanices and topological defects throughout the plane of thermally reduced GO [108].

- One other method proven to reduce GO relies on the removal of oxygen-based functionalities through electrochemical means. This involves deposition of GO on variety of substrates and then subjecting the deposition to voltammetry in a buffer solution. Prompt reduction takes place which results in the creation of rGO film having conductivity approximately around 8500 S m^{-1}. This methods has shown the viability of reducing GO with the visible advantage of avoiding hazardous chemicals as well as high temperature processes, but for broad range applications, scalability of such process remains unclear.

2.4.1.4 Functionalized graphene

Other than oxygen-based functional groups attached to the carbon structure of graphene, covalent or non-covalent attachments of other chemical groups have been reported thus defining a new category of graphene known as functionalized graphene or chemically modified graphenes (CMGs). The association of functional groups to the graphene structure is based on the fact that, in case of GO, orthogonal reactions take place to the groups (carboxylic acid, epoxy and hydroxyl groups) attached to the structure which allows selective functionalization of one site over the other. While in the case of rGO, modification could take place by non-covalent physisorption, π-π stacking or van der Waals interaction [77]. Although selective chemical transformation is a challenging task, however functionalized graphene has proved to be a versatile precursor for a wide variety of applications like polymer composites [109, 110], optoelectronics [111, 112], drug-delivery vehicles [113] and biodevices [114].

2.4.2 Application of graphene in polymer composites

Due to the superlative properties of graphene and its versatility of having multiple functional properties, graphene tends to find its importance in polymer based nano/micro/composites as well. As filler, graphene improves the engineering capabilities of a composite structure. However, the crucial factors that determine the optimum level of loading in polymer matrix include graphene’s surface activity, level of dispersion in polymer matrix, chemical affinity to the surrounding medium and percolation threshold at which the properties of the composite improve dramatically. Such interaction thus cause the improvement in properties like electrical, optical, thermal, magnetic and especially mechanical [115] thus raising the application range from laboratory scale to industrial/commercial scale.

Electronic devices have found increasing applicability of graphene/polymer nanocomposite due to its high carrier mobility, high electrical conductivity and moderately high optical transmittance in the visible spectrum. Significant uses, but not limited to, include organic solar cells [116-118], liquid crystal devices [119], dye-sensitized solar cells [120, 121], organic light emitting diodes (OLEDs) and field emission devices [122, 123]. Graphene based polymer nanocomposite thin films are also getting a huge attention from the most popular technology of modern era i.e., touch screens, flat panel displays etc [124]. Such thin films are being developed by CVD grown graphene which is transferred to polydimethyl siloxane or polyethelene terephthalate (PET) [124, 125]. Such films have also been tested for solar cell applications [116] and field effect transistors [125]. In addition to these, graphene-doped conducting polymers such poly (3,4-ethyencdioxy thiophene) poly (styrenesulphonate) (PEDOT:PSS) and poly (3-hexylthiophene) (P3HT) have demonstrated to offer improved power consumption efficiency as compared to counter electrodes based on PEDOT:PSS in dye-sensitized solar cells [121].

Conductive graphene/polymer nanocomposites also find their usefulness in important applications like electrostatic discharge (ESD) and electromagnetic interference shielding (EMI). Recent reports have indicated a higher shielding efficiency from EMI in case of graphene based polymer composites [62, 126-128].

2.5 Electrophoretic deposition

The electrophoretic deposition (EPD) is a technique consisting of colloidal process of depositing a variety of micro or nano scaled materials (metallic, polymeric and/or ceramic particles) on to a diverse range of substrates in the form of thin films or coatings depending on a variety of deposition parameters. It is one of the efficient processes that enable the user to achieve microstructural and morphological homogeneity in the deposition products with also a high packing density [129]. The popularity of such deposition process is due to, but not limited to, its simplicity, cost-efficiency, wide applicability and scalability to large dimensions [130, 131].

The process of deposition involves the mobility of charged particles (required to be deposited) between a pair of electrodes towards a substrate (which could act as an electrode), due to an applied electric field. The outcome of the motion of electrically charged particles in the deposition process is the accretion of particles and development of a homogenous and firm deposit. As opposed to other colloidal processes, low solid loadings in the suspension results in low viscosity hence facilitating of easy handling and simple processing. As a thumb rule, any solid particulate form with a particle size less than 30 µm can be deposited on to substrates using EPD technique [130, 131].

2.5.1 Parameters

Considering the final properties of the deposition like thickness, homogeneity etc., it is important to control many parameters involving the EPD process. These could include parameters related to either the suspension or the deposition process.

The importance of particle nature is of prior importance when considering deposition of a thin film or coating over a substrate. Obtaining a homogenous and smooth deposition requires a stable aqueous suspension which consequently depends on having particles suspended in the liquid for a longer period of time. This could be achieved if the particles bear a certain electrostatic charge and are light and small enough to defy gravity. Hence a uniform deposition could be achieved by small particles (<30 µm). However this doesn't imply that larger particles can't be homogenously deposited which can be possible only if they have strong surface charge. It has been also reported that for the final deposition to be crack-free, smaller particle size is essential [132].

The suspension's nature used in EPD has shown to be also a key factor in determining the properties of deposition product. A highly conductive suspension results in slow particle motion in the aqueous medium while too resistive suspension would render the instability of particle's charge [133]. A similar behavior can also be obtained when considering the dielectric constant of the liquid. In case of low dielectric constant, deposition fails due to insufficient dissociative power while a high dielectric constant reduces the double layer region due to high ionic concentration in the liquid and hence affects greatly the electrophoretic mobility [134].

As discussed earlier, the stability of the suspension is a key factor in the electrophoretic deposition process which is determined by a factor called the Zeta potential. A Zeta potential is defined as the degree or quantity of magnitude of the electrostatic charges or charge repulsion/attraction between the particles in a suspension. A high and uniform surface charge of the suspended particles paves the path in EPD towards: i) suspension stability due to the intensity of repulsive interaction between particles, ii) mobility and velocity of charged particles during EPD and iii) determination of the green density of the deposit [135]. The key success of achieving a uniform deposition is the mobility of particles individually rather than as agglomerates hence it is of great necessity the presence of high particle charge density in a suspension. Similarly, the presence of sponge and porous-like deposits also come from the fact that low charged particles when are deposited on to a substrate tend to coagulate at relatively large inter-particle distances. Contrarily, highly charged particles will repulse each other during deposition and while occupying position individually would lead to a solid and high particle packing density [136]. The manipulation of zeta potential, luckily, can be done by different additives, such as acids, bases and polyelectrolytes in the suspension which affect the charge magnitude and polarities of the particles [137].

Deposition process parameters also have a great effect on the depositions in the EPD process. A prolonged deposition time would result in increasing amount of thickness of deposit (**Figure 2.14**) but this, at the same time, results in lowering of deposition rate. Previous studies have shown that deposition is linear during the initial deposition period but if longer time is allowed, the rate decreases and attains a plateau at high deposition times [138] Logically, a higher applied potential could result in increased amount of deposit but the downside of such higher driving force could be deterioration of the deposit. Basu et al. reported uniform film deposition at moderate applied fields while relatively higher applied fields have negative effects on the quality of the deposit [139]. This has been justified by the theory that higher applied fields causes turbulence in the suspension which disturbs the flow in the surrounding medium of the coating, during or after the deposition. In addition, the particles moving fast towards the substrate don’t attain enough time to settle in positions to form a close-packed structure. Finally higher potential applied means higher particle flux and movement thus exerting pressure on the already deposited particles thus creating disruption in the structure of the deposit [135].

In processes like EPD, it is highly desirable to use substrates with excellent electron conductivity, like as metals or alloys. In cases when non-conductive materials are desired to be coated, either pre-coating of the surface is required to provide the electron conductivity of the surface or the substrate could be placed between the electrodes in the EPD suspension. Studies have shown the effect of substrate electrical conductivity on the green density of the deposits achieved in EPD [140].

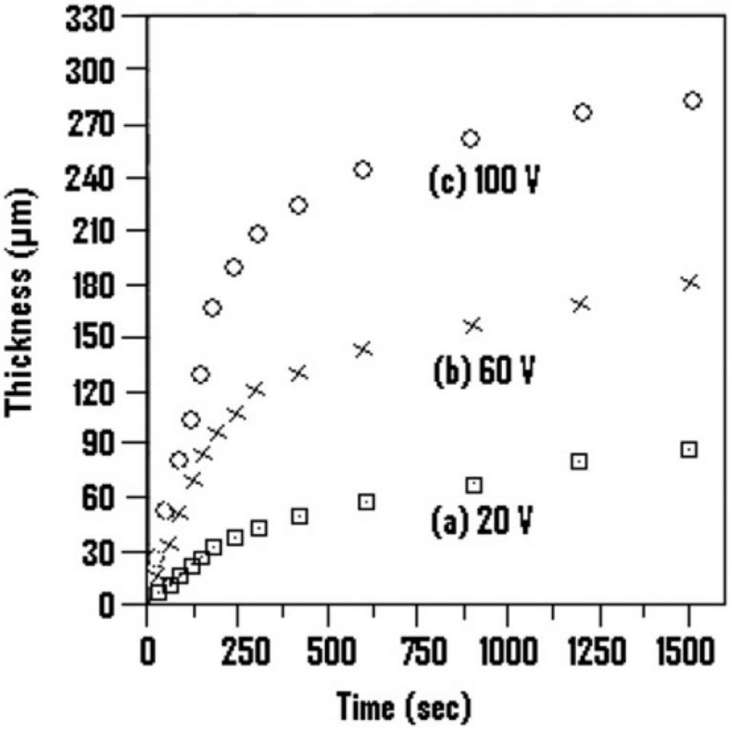

Figure 2.14. Deposition thickness with respect to deposition time for ZnO coatings on copper electrode at different applied potential (adapted from [135]).

2.5.2 Kinetics

A successful EPD process requires the user to be acquainted with the knowledge of the EPD's kinetics. This would ensure, not only the control and manipulation of deposition rate, but also the opportunity to vary the deposit's microstructure. According to a study [140], the kinetic aspects of EPD depend on four possible deposition parameters:

Table 2-3. Possible deposition parameters in EPD.

	Current	**Voltage**	**Concentration**
A	Constant	Unaltered	Constant
B	Constant	Unaltered	Decreasing
C	Unaltered	Constant	Constant
D	Unaltered	Constant	Decreasing

The result of these conditions can be best visualized as in **Figure 2.15**. Curve A shows a constant deposition rate with maximum yield if allowed sufficient deposition time, while curves B, C and D, one way or the other the deposition rate decreases asymptomatically as well as also the rate of deposition respectively. In either case of constant-current or constant-voltage condition, the effect of decreasing suspension concentration on the reduction of the rate of deposition and final yield is apparent. Even if the suspension concentration is unaltered (curve A and C) during deposition, it is clear that the final yield is significantly higher in curve A than curve C and the rate of deposition was constant in curve A while it decreased asymptotically with respect to time in case of curve C. Hence the deviation of curve A from curve C is not because of lowering of suspension concentration but is basically due to the decrease of particle velocity as a function of deposition time. Such effect is caused when a constant-voltage deposition is carried out where the deposited mass creates a shielding effect and hence presents a higher electrical resistance compared to the suspension where the deposition is taking place. Subsequently, the electrical driving force per unit length of suspension decreases with time as the deposit grows.

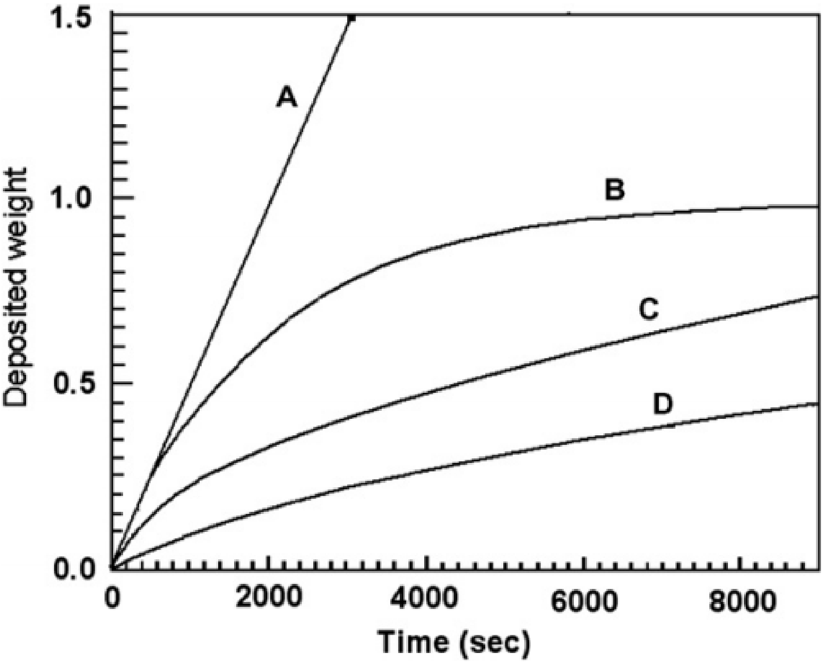

Figure 2.15. Schematics of EPD kinetics (Adapted from [140]).

2.5.3 Mechanism

A number of various mechanisms have been reported in literature previously regarding the formation of a deposit in the EPD process. Haymaker and Verwey [141] discussed the possibility of formation of a deposit by electrophoresis is similar to as the formation of a sediment due to gravitation. In other words, the pressure exerted by incoming particles permits the particles near to or in the deposit to overcome the interparticle repulsion. Mechanism of neutralization of particle charge was suggested by Grillon et al. [142] that any particle that would come in contact with the deposition electrode or the deposit would be neutralized and become static. Such mechanism has a great importance in case of single particles or monolayer deposits. This mechanism describes the initial stage deposition from very dilute suspension however it is invalid for the cases in which a) EPD is carried out for longer times, b) particle-electrode processes are prevented like semi-permeable membrane induces deposition between electrodes and c) reactions occur at the electrode which modify the pH in the vicinity.

In one theory, Sarkar and Nicholson [131] showed that there was no increase of electrolyte concentration near the electrode takes place. As shown in **Figure 2.16**, they considered the movement of positively charged particles such as oxide particle towards the cathode in a typical EPD cell. In such case when the particle's lyosphere system (or the diffuse double layer which is the formation of the counter ions from liquid around the charged particle) moves, the applied electric field and also the fluid dynamics distort the double layer in a way that it becomes more thinner ahead and slightly wider behind the particle. The cations, along with the positively charged particle, in the liquid also move towards the cathode. These counter ions will tend to react with these accompanying cations in high concentration around them. Such chemical reaction hence causes the thinning of the double layer around the 'tail' of the particle so that the next incoming particle can approach for London Van der Waals attractive forces to dominate and induce coagulation or deposition. This mechanism has high plausibility to occur firstly due to the presence of particles near the electrode and secondly it works for incoming particles with thin double layer heads, coagulating with particles already in the deposit.

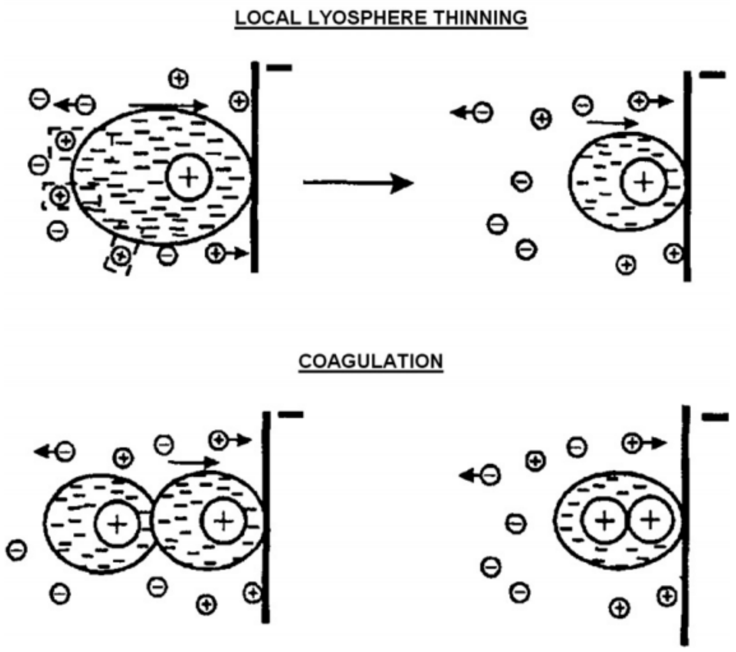

Figure 2.16. Electrical double layer distortion and thinning mechanism for electrophoretic deposition (Adapted from [131]).

2.5.4 Applications

Since the advent of nanotechnology and increasing understanding of nanoparticle’s nature, there is an ever increasing demand and interest of utilizing the proliferating advantages of nanomaterials in engineering applications. To elucidate and exploit the benefits on a wider scale, it is important to recognize the control, distribution and integration of nanomaterials in an effective manner. Deposited nanomaterials have shown to possess as many potential applications as individual nanomaterial does. Hence, development of modes and techniques to spread nanomaterials would impart a vital action in their execution in commercial and industrial applications. Fortunately, due to a great number of successful studies, a wide array of material classes have been demonstrated to be electrophoretically deposited like metals, polymers, ceramics and new generation of nanomaterials like carbon nanotubes (CNT), graphene etc. Moreover, the favorable and promising processing condition facilitates the creation of different coatings, shaping monolithic objects and also infiltration of porous materials and woven fiber preforms for composite production.

In terms of CNT, EPD has demonstrated to be a powerful tool for creating an ordered structure of CNT and CNT-based nanostructures for a considerable number of applications.

The ease of manipulation the processing conditions, novel applications based on CNT and its composite have been recently reported including but not limited to continuous films for various applications like porous film [143], CNT-reinforced resin films [144], composite films [145-147], complex patterns, membranes/nanofilters [148], nanoelectronics [146, 149-151], fuel-cell electrodes [152-154] and supercapacitors [155].

Graphene, being more superlative nanomaterial as compared to CNT, has shown more promise in engineering applications due to its excellent electrical conductivity, large specific surface area, optical transparency and electronic properties. EPD has also shown to be a beneficial technique for depositing graphene for various applications like field emission devices [156-158], biosensors [159], energy storage applications [160-163], optoelectronics [164], capacitors [164-166], fuel cells [156, 167, 168], electrochemical sensors [169] and solar cells [170, 171].

Chapter 3 - Experimental

3.1 Materials

3.1.1 Epoxy

A bi-component was used in this work to act as a matrix for the fiber reinforced composite. The system (**Figure 3.1**) was composed of a resin (EC 252) and a hardner (W 241) provided by Elantas Italia S.r.l. (Collecchio, Italy), whose properties are listed in **Table 3-1**.

Table 3-1. Properties of epoxy resin and hardner.

Resin:	
Industrial code	*EC 252*
Viscosity (25°C)	*300-400 mPas*
Color	*Transparent*
Density (25°C)	*1.1 – 1.14*
Hardner:	
Industrial code	*W 241*
Viscosity (25°C)	*180 – 300 mPas*
Color	*Transparent*
Density (25°C)	*0.99 – 1.01*

The ratio of resin to hardner used in this work was 100:40 and the curing cycle selected was at least 3h at 23°C (room temperature) followed by 15h at 60°C. At the end, the samples were left in an oven to cool down (annealing). The final density of cured epoxy resin as calculated by ASTM D792 – 13 was 1.14 g/cm^3 as described in section 3.4.1.1.

Figure 3.1. Epoxy system: Hardner (left) and resin (right).

The terminology, epoxy, in polymer refers to a family of monomers that consists of an epoxy/oxirane ring, which is a three-membered ring comprising two carbon atoms and an oxygen atom bonded with two and one hydrogen atoms respectively as displayed in **Figure 3.2** [23, 172]. The functionality of epoxy resin depends on the number of these oxirane rings per epoxy resin, which can be situated internally, terminally or in cyclic structures [172].

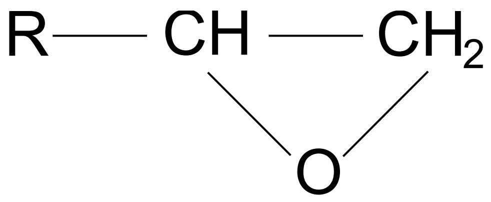

Figure 3.2. Epoxy/Oxirane ring – Chemical structure.

3.1.2 Glass fiber

E-glass fibers, with the trade code XG 2089, were kindly supplied by PPG Fiber glass© (**Figure 3.3**). These had an average diameter of 16.0 ± 0.1 µm with an epoxy compatible silane-based coupling agent. These fibers were used without any further treatment. The apparent density of the GF was calculated using helium pycnometry technique (section **3.4.1.2**).

Figure 3.3. Left: PPG XG2089 Glass fiber roving, Right: close up of glass fibers.

3.1.3 Graphene nanosheets

Graphene nanosheets were prepared by using the well-established Hummer's method but with a slight modification [104]. The liquid-based chemical reaction was applied to graphite powder (particle size < 20 µm) supplied by Sigma Aldrich (USA) to produce graphite oxide. The produced product was treated further to create graphene oxide and reduced graphene oxide, which will be discussed in next sections.

3.1.3.1 Graphite oxide synthesis

Graphene oxide was synthesized using an approach similar to Hummer's method [104]. 1 g graphite powder was added into 46 ml of H_2SO_4 cooled in an ice bath and was stirred for 10 min followed by the addition of 1 g of $NaNO_3$ and further stirred for 15 min. Then 6 g of $KMnO_4$ were added very slowly to avoid a spontaneous exothermic reaction in the mixture. After that, it was allowed to stir for at least 24 h at 35°C. Finally, distilled water in an excess was added to the above mixture in such a way that the temperature was kept under 80°C. The reaction was terminated by the addition of 30% hydrogen peroxide (H_2O_2) to the mixture. The final product was comprehensively washed using hydrochloric acid (HCl) solution and distilled water to eliminate manganese (Mn) ions and acid respectively. The obtained brown solution was dried in a vacuum oven at 50°C for at least 36h.

3.1.3.2 Graphene oxide exfoliation

Graphene oxide was obtained by mechanical exfoliation of the graphite oxide obtained from the chemical reaction described in section 3.2.1.1. In this process, graphite oxide in a determined amount was added in de-ionized water and was then subjected to ultrasonication using a tip sonication machine (Hielscher UP400S, **Figure 3.4**) for 60 mins at least with a power of 4000W, amplitude of 50% and 0.5 cycle to completely exfoliate the graphene oxide nanosheets.

Figure 3.4. Hielscher UP400S tip sonication device.

3.1.3.3 Reduction of graphene oxide

In this work, reduction of graphene oxide was carried out for two different requirements.

i) *Characterization*: In order to evaluate the reduction of GO, the product obtained on the electrodes during electrophoretic deposition was placed in a glass petri dish along with a tissue paper soaked with hydrazine hydrate (N_2H_4). The petri dish was covered and was then heated for 24h at 100°C.

ii) *Reduced graphene oxide coated fibers*: In this case, the GO coated fibers were placed in a suitable glass container and the reduction was carried out in the same way as described in the previous paragraph.

3.2 Electrophoretic deposition of GO on GF and reduction to rGO

The technique used here to coat graphene nanosheets on GF was electrophoretic deposition (EPD) [173]. According to the section 2.5.1, the deposition quality and quantity are both dependent on the parameters of the deposition process. In this work, certain parameters were kept constant while only the deposition voltage was varied according to the requirement (**Table 3-2**).

Table 3-2. Electrophoretic deposition parameters.

Parameter	**Value**
Applied voltage	5V, 10V, 15V, 20V
Distance between cathode and substrate	2 cm
Time	5 min
Dispersion concentration	1 mg/ml

A schematic diagram of the EPD process is shown in **Figure 3.5.** Electrophoretic deposition setup, a schematic diagram. The electrodes used were copper sheets of 1 mm thickness and GF were placed in front of an anode using a metallic window. This is basically due to the nature of GF being insulating. Therefore, in order to deposit the nanoparticles on the GF, an electrode was placed behind the fibers during the deposition process. The electrodes along with metallic frame containing GF (**Figure 3.6**) were immersed in a graphene oxide dispersion of 1 mg/ml concentration as shown in **Figure 3.7**.

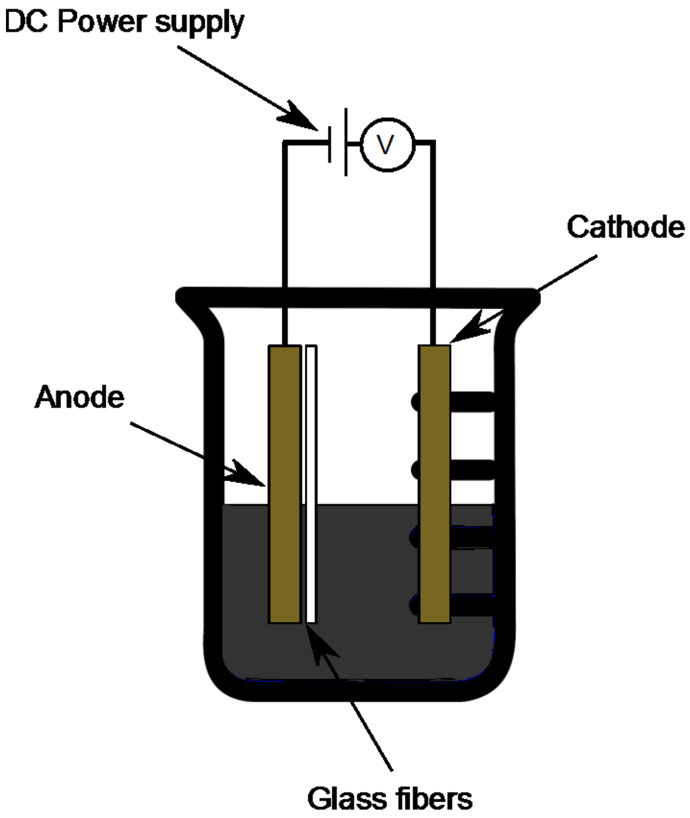

Figure 3.5. Electrophoretic deposition setup, a schematic diagram.

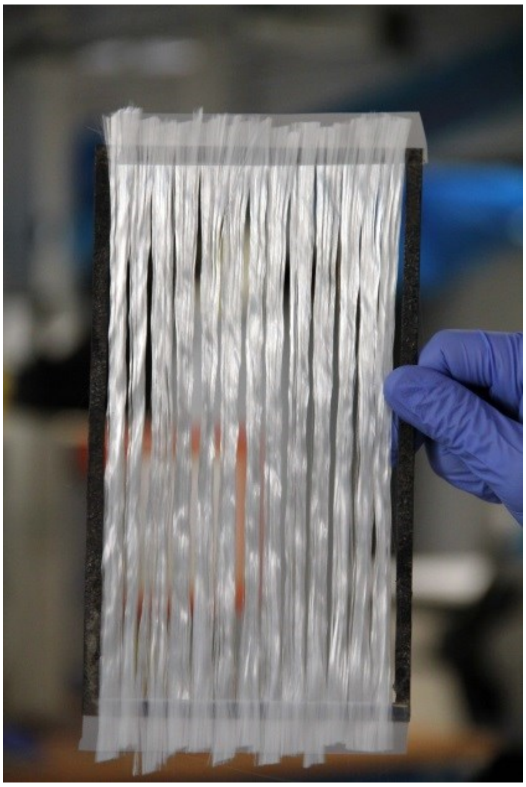

Figure 3.6. Glass fibers on metallic window frame.

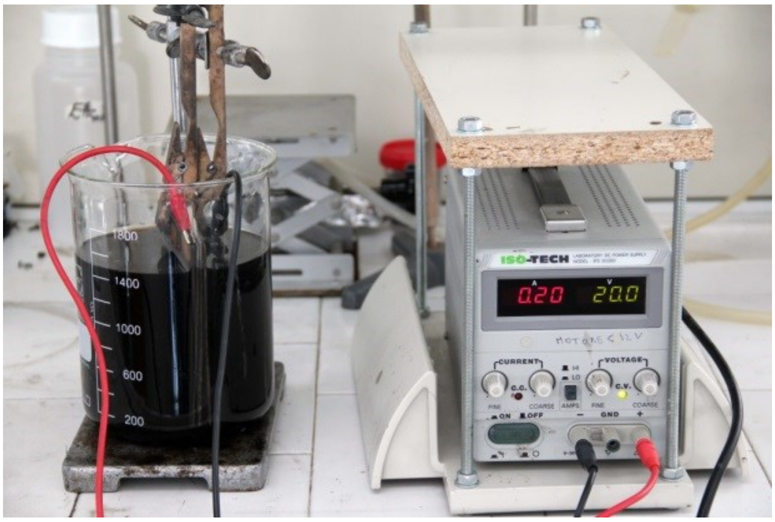

Figure 3.7. Electrophoretic deposition process, deposition of graphene oxide on glass fibers.

Since the nature of GO particles is negative due to the chemical modification process in the modified Hummer's method (section **3.1.3.1**), the fibers were placed in front of anode so that the particles moving towards anode, when voltage was applied between the electrodes, would tend to hit the GF and hence get deposited on the surface of the fibers. The deposition on one side of the fibers was carried out according to the given parameters and the same process was repeated while reversing the metallic frame to expose the uncoated portion towards cathode while coated side of the fibers towards the anode. After the whole coating process, the fibers were dried under vacuum at 50°C for at least 12 h. **Figure 3.8a** shows the GF obtained after the drying in vacuum, the slight color change of GF from white to beige confirmed the coating of GO on GF.

In order to reduce the GO coating on GF laminate obtained in previous step, the same was subjected to thermochemical reduction as described in section **3.1.3.3**, the resultant fibers appeared to be dark grey in color which visually confirms the reduction of GO on GF as it can be visualized in **Figure 3.8b.**

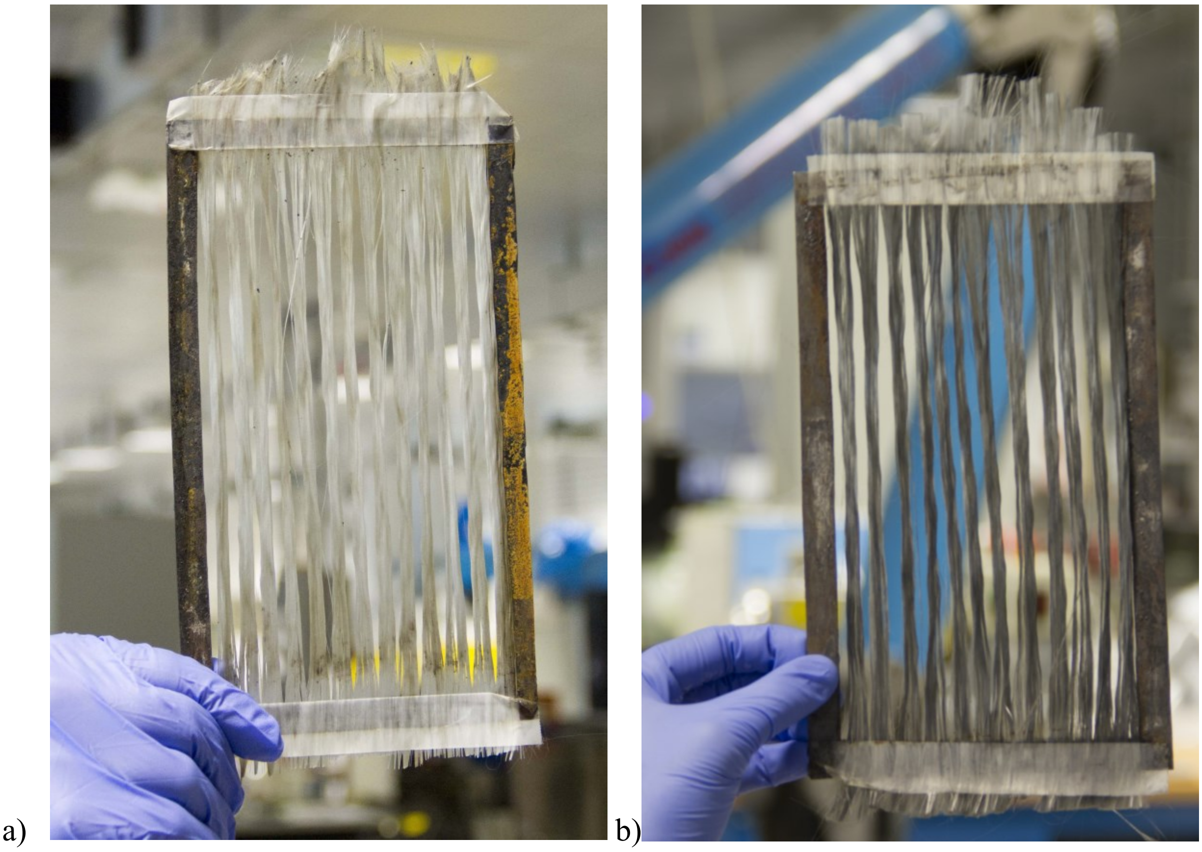

Figure 3.8. a) Electrophoretic deposition of GO on GF and b) subsequent thermochemical reduction to obtain rGO coated GF.

3.3 Composites preparation

3.3.1 Micro-composite preparation

For the evaluation of interfacial adhesion between fiber reinforcement (uncoated or coated) and epoxy matrix, single fiber epoxy composites were prepared. Specimens were prepared in a silicon mold by suspending the fiber in the center of mold and embedding in the epoxy matrix. The samples were cured at room temperature for at least 3 hours and then thermally cured at 60°C for 15 hours. After that, the samples were annealed in oven before taking them out for testing. The final specimen dimensions were 50 mm × 5 mm × 2 mm.

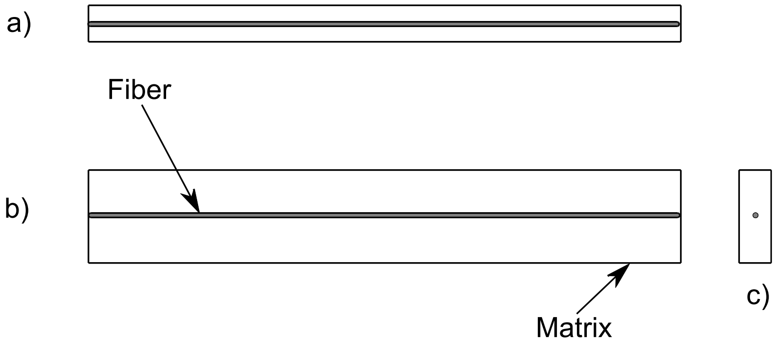

Figure 3.9. Single fiber composite specimen for fragmentation test, a) Side view, b) Top view, c) Front view.

3.3.2 Macro-composite preparation

Since GF coated with GO and rGO at 10V/cm showed the maximum ISS values in the SFFT (as investigated in section **4.5**), hence it was decided to use the same parameters of GO and rGO coating on GF for their use in macro-composite preparation with epoxy resin as matrix. Macro-composites were prepared by hand lay-up method (**Figure 3.10**) in which the fibers (uncoated, GO and rGO coated) in the form of laminates were stacked while resin was infused within the fibers using a roller. After laminating certain number of laminas for required thickness of composite, a constant load of approximately 0.01 MPa was applied on the composite by placing some load on the structure and curing was performed as described in section 3.1.1.

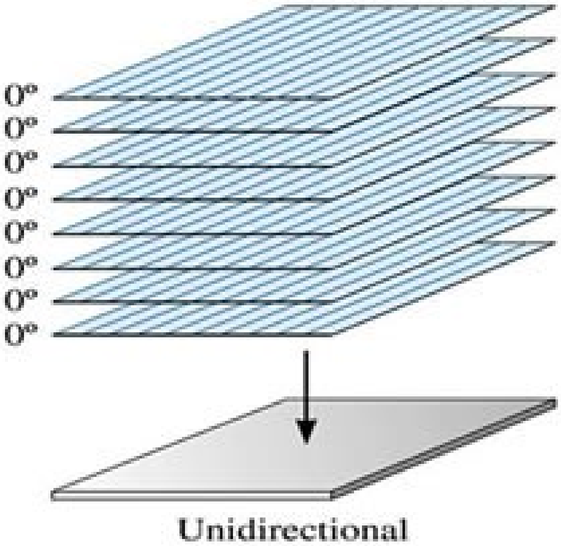

Figure 3.10. Hand lay-up method for producing unidirectional FRP composites.

3.3.3 Samples designation

Composites were designated based on the type of reinforcement. Composites based on uncoated glass fibers are referred to as Ep-GF composites, while GO and rGO coated glass fibers based composites were referred to as Ep-GO-GF and Ep-rGO-GF respectively.

3.4 Testing procedures

3.4.1 Density measurements

3.4.1.1 Displacement method

Density of the neat epoxy and multiscale composites were measured according to the ASTM standard D792 – 13. The weight of the specimen was measured in both air and pure distilled water and the following formula was used to calculate the density:

$$D_S = \frac{m_a}{m_a - m_w} \times D^T{}_w$$

where:

D_S = Density of specimen

m_a = Mass of specimen in air

m_w = Mass of specimen in water

$D^T{}_w$ = Density of water at the time of testing

3.4.1.2 Helium pycnometry

Density measurements were carried out using helium pycnometry technique (Micromeritics®Accupyc 1330 helium pycnometer), at an ambient temperature of 23 °C, using a testing chamber of 3.5 cm^3 (**Figure 3.11**).

Figure 3.11. Micromeritics®Accupyc 1330 helium pycnometer

3.4.2 Thermal analyses

3.4.2.1 Differential scanning calorimetry (DSC)

Differential scanning calorimetry tests were performed by a Mettler DSC30 calorimeter (**Figure 3.12**) on samples weighing around 10 mg. The tests were carried out under constant nitrogen flow of 100 ml min^{-1} and temperature ramp of 10°C min^{-1} between 0° to 200°C. The glass transition temperature was measured as the inflection point in the DSC curve.

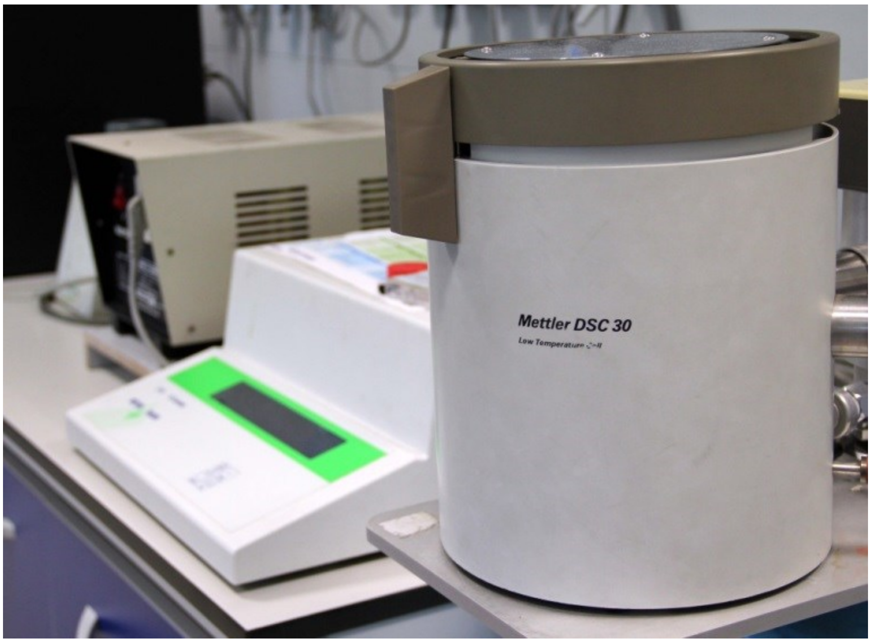

Figure 3.12. Mettler DSC30 Differential scanning calorimeter.

3.4.2.2 Thermogravimetric analysis (TGA)

The thermal stability of epoxy and different composites were investigated using thermogravimetric analysis (TGA) using a Mettler TG50 thermobalance (**Figure 3.13**). Around 10 mg and 40 mg of the specimens were selected of epoxy and composites respectively. The tests were conducted between 25°C and 700°C. The onset temperature (associated to a mass loss of 5%) and the residual mass at 700 °C were determined. The maximum degradation temperature was evaluated from the main peak of mass loss rate curves.

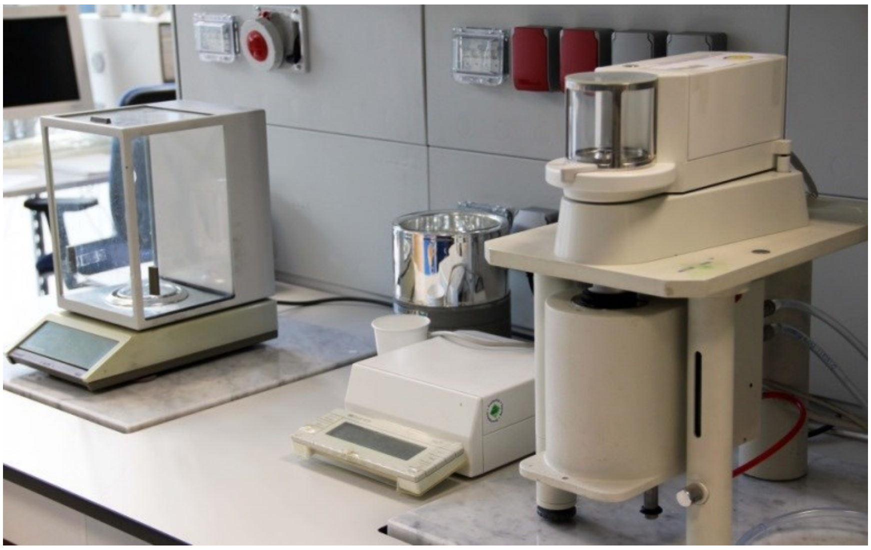

Figure 3.13. Mettler TG50 thermogravimetric analysis machine.

3.4.3 Morphological characterization

3.4.3.1 Optical microscopy

The cross-section view of multiscale composites was observed by optical microscopy technique using a Zeiss Axiophot optical microscope, equipped with a Leica DC300 digital camera. The specimens were polished using abrasive grinding papers with grit size 800, 1200 and 4000 sequentially.

3.4.3.2 Scanning electron microscopy (SEM)

Morphological analyses of different specimens were performed by field emission scanning electron microscopy (FESEM) using a Zeiss Supra 40 microscope (Berlin, Germany) (**Figure 3.14**). Before performing microscopy observations, the specimens were coated by a platinum/palladium alloy (80:20) thin coating of about 5 nm.

Figure 3.14. Zeiss Supra 40 field emission scanning electron microscope.

3.4.3.3 Friction force microscopy (FFM)

FFM (friction force microscopy) was performed in contact mode in atomic force microscopy (AFM) using diamond coated cantilever tip apex (model: DCP01_NTMDT) [173]. Here, AFM plays a dual role of mapping and manipulating the substrate in a sequential manner. Sader method [174, 175] was applied to measure normal (K_N) and torsional (K_T) spring constants of cantilever. Typical values of $K_N = 6.03\times10^8$ N/m and $K_T = 8.25\times10^8$ N/m for cantilever with tip radius of 51 nm were obtained. Calibrated tip was slid from bare GF to GO covered region at a fixed normal force (F_N).

3.4.4 Chemical structure analyses

3.4.4.1 X-ray diffraction (XRD)

The oxidation level of graphite was analyzed using the x-ray diffraction technique in which an x-ray diffractometer (Rigaku III D-max) was employed consisting of a monochromatic radiation source of Cu-Kα line of wavelength around 51.54056 Å (**Figure 3.15**). The measurements were carried out in the 2θ range of 5-80° with a step size of 0.04°.

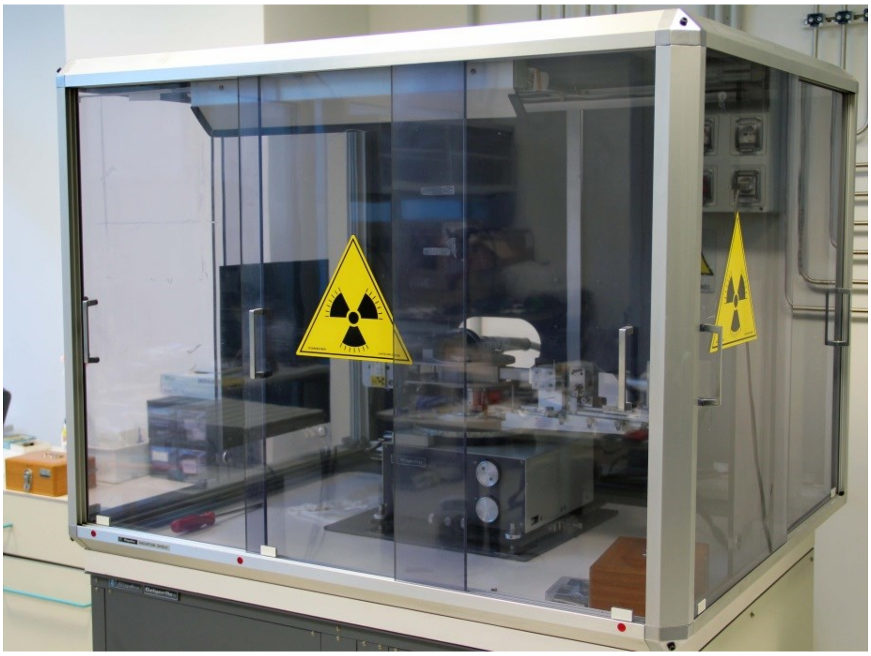

Figure 3.15. Riagku III D-max x-ray diffractometer.

3.4.4.2 Fourier transform infrared spectroscopy (FTIR)

Fourier transform infrared spectroscopy was recorded using a Nikolet Avatar 330 device with a 4 cm^{-1} resolution (**Figure 3.16**). The samples were prepared by mixing the samples in tiny amount in KBr powder and forming thin discs in a mold under a compressive pressure of 10 bar.

Figure 3.16. Nikolet Avatar 330 Fourier transform infrared spectroscopy machine.

3.4.4.3 X-ray photoelectron spectroscopy (XPS)

Elemental composition of GO and rGO was analyzed by X-ray photoelectron spectroscopy (Kratos Axis Ultra DLD) machine equipped with a hemispherical analyzer and a monochromatic Al Kα (1486.6 eV) x-ray source (**Figure 3.17**). A 90° emission angle between the axis of the analyzer and the sample surface was adjusted. O 1s and C 1s core lines of each sample were collected. The quantification, reported as relative elemental percentage, was performed using the integrated area of the fitted core lines, after Shirley background subtraction, and correcting for the instrument sensitivity factors.

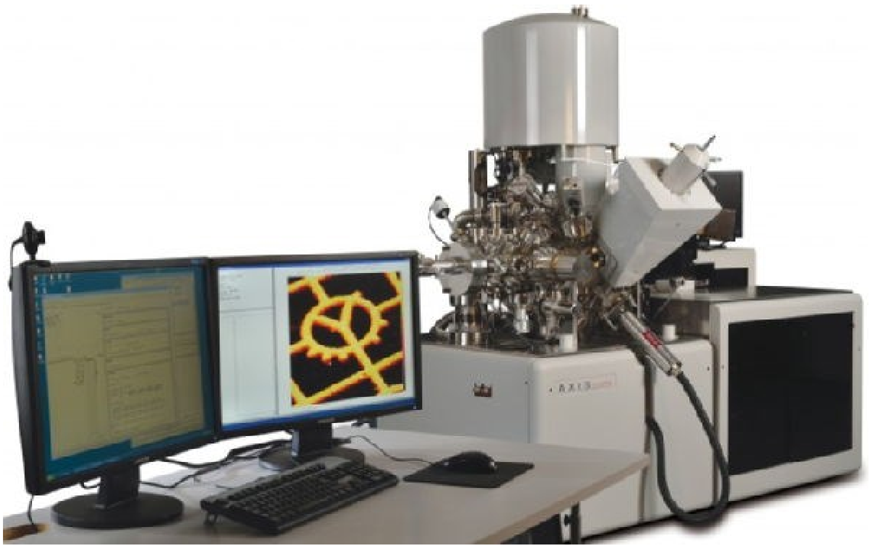

Figure 3.17. Kratos Axis Ultra DLD x-ray photoelectron spectroscopy machine.

3.4.5 Mechanical characterization

3.4.5.1 Single fiber tensile testing

To determine the strength of the glass fibers, single filament of fibers (mounted on a paper tab, **Figure 3.18**) were tensile tested with an Instron® 4502 (Norwood, USA) universal tensile tester equipped with a 10N load cell. According to ASTM C1557-03 standard, a gage length of 20 mm was selected and 31 samples were tested at a cross-head speed of 0.2 mm-min^{-1}. The iterative procedure proposed by Gurvich et al. [176] was applied to perform data reduction.

The tensile strength of the fiber was calculated as:

$$\sigma_{fb} = \sigma_0 \left(\frac{L}{L_0} \right)^{-\frac{1}{m}} \Gamma\left(1 + \frac{1}{m}\right) \tag{3-1}$$

where Γ is the Gamma function, while σ_0 and m are respectively the scale and shape parameters of the Weibull distribution, which were evaluated from the strength data determined at one single gage length by fitting the distribution of the failure probability.

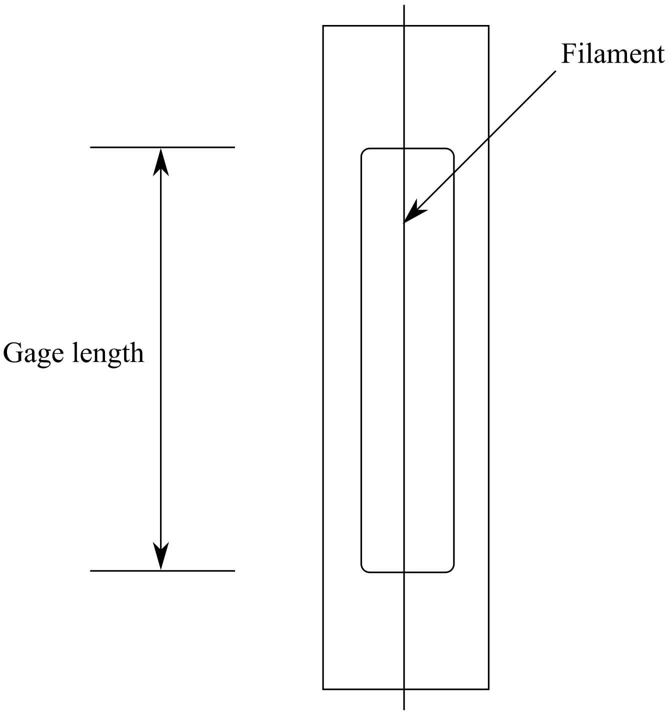

Figure 3.18. Schematic diagram of single fiber filament mounted on a paper tab.

3.4.5.2 Single fiber fragmentation test (SFFT)

A tensile testing machine (Minimat, by Polymer Laboratories, Loughborough, UK) was utilized to perform single-fiber fragmentation tests. A polarized optical stereo-microscope (Wild M3Z, Leica) was used to observe the fiber fragmentation process while performing the tensile test (**Figure 3.19**) at a cross-head speed of 10 mm min^{-1}. The test was continued until 10% of strain was achieved in order to ensure a saturation of fragmentation across the length of the fiber.

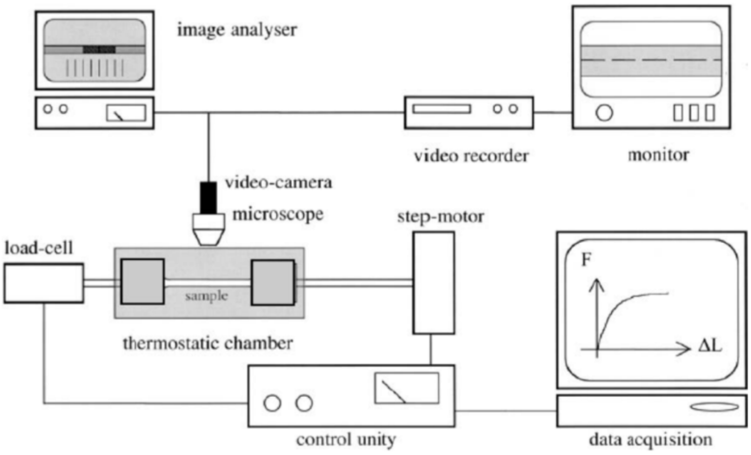

Figure 3.19. Single fiber fragmentation test, a schematic construction of the setup.

The mean fiber length at saturation, L_s, was calculated through an image analysis software (ImageJ) from which the fiber critical length, L_c, was estimated as $4/3L_s$. According to Kelly-Tyson approach, an average value of ISS was calculated according to the following formula,

$$ISS = \frac{\sigma_{fb(L_c)} d}{2L_c} \tag{3-2}$$

where $\sigma_{fb(L_c)}$ is the tensile strength of the fiber at the critical length, d is the fiber diameter and L_c is the fiber critical length as estimated from the fragmentation test.

3.4.5.3 Quasi-static tensile tests

Uniaxial tensile tests were performed on neat epoxy using an Instron® 4502 (Norwood, USA) universal tensile tester. At least 5 1BA type dumbell specimens (ISO 527 standard) were prepared and the tests were tested at a crosshead speed of 0.25 mm min^{-1} up to 1% axial deformation using a resistance extensometer (Instron® model 2620-601, gage length 12.5 mm). The elastic modulus was calculated as a secant value between deformation levels of 0.05 and 0.25% as per ISO 527 standard. Ultimate tensile properties were evaluated by testing the specimen at a higher cross-head speed (10 mm min^{-1}) without extensometer.

3.4.5.4 Dynamic mechanical thermal analysis (DMTA)

Viscoelastic properties of the fabricated composites were determined by DMTA analysis. Samples of dimensions 55 mm × 13mm ×1.3 mm were tested between a temperature ranges of 0 to 150°C with a temperature ramp of 5°C/min in dual-cantilever mode.

The creep behavior under variable thermal conditions of the composite specimens (with uncoated or coated fibers) were investigated using TA instruments DMA Q800 in dual cantilever mode. The composite specimens were tested at 30°C for 3600 s by applying a constant stress (σ_0) of 5MPa while the frequency of applied oscillating strain was 0.05. Rectangular specimens with dimension of 55 mm × 13mm ×1.3 mm were used while adopting a constant span length of 35 mm. The creep compliance D(t) was plotted against the time for different composites.

Findley's model was adopted to fit the experimental data obtained through creep testing. This model can be obtained by expanding the Kohlrausch–Williams–Watts (KWW) model, generally described by a Weibull-like function as a series and ignoring all but the first term [177]:

$$D(t) = D_0 + k(t)^n \tag{3-3}$$

where D_0 is the elastic instantaneous creep compliance, k is a coefficient related to the magnitude of the underlying retardation process and n is an exponent tuning the time dependency of the creep process. D_0 and k are functions of environmental variables. In this work, creep curves at different temperatures for different composites were fitted using Findley's model to investigate possible correlations between the viscoelastic response of the material and the fitting parameters.

3.4.5.5 Three point bend test

To measure the flexural properties of uncoated and graphene interphase reinforced composites, three point bend test was performed in accordance to ASTM D790 – 15. The specimens tested had dimensions of around 80 mm × 13 mm × 1 mm and the span to depth ratio for flexural tests was 60:1 and 40:1 for determining flexural modulus and flexural strength respectively.

3.4.5.6 Short beam shear test

Interlaminar shear strength of the laminated composites (uncoated and graphene interphase reinforced) was determined using short beam shear test according to ASTM D2344

– 13 standard. At least 5 specimens of 4 mm thickness were tested under 3 point bending conditions until the deflection equal to the thickness of the sample was achieved. The maximum corresponding force (F_m) value was used to evaluate the interlaminar shear strength as:

$$ILSS = 0.75 \times \frac{F_m}{b \times h} \tag{3-4}$$

where b and h are the width and thickness respectively

3.4.5.7 Mode I fracture toughness: Double cantilever beam (DCB) test

Investigation of the fracture toughness under opening mode (mode I) condition was performed by a test called double cantilever beam test according to the given standard of ASTM 5528 – 01. The sampling involved creation of a composite laminates having 18 fibers plies (coated or uncoated) with an insert of Teflon thin film (thickness = 23 µm) as a crack starter. The final dimensions of the specimen were 180 mm × 25 mm × 4 mm. Piano hinges were attached to the composite specimen 50 mm apart from the crack tip at the crack end (**Figure 3.20a**). The crack advance during the test was monitored using a digital webcam (Logitech B910 HD) recording the test simultaneously with the test procedure. Three specimens of each composite type were tested and the results were interpreted by considering three different G_{Ic} values. i) *Deviation from linearity (NL)* was obtained by considering the point in load-displacement plot where deviation from linearity was observed (or onset of nonlinearity NL), assuming the delamination starts to grow from the insert. ii) *Visual observation (VIS)* point where the delamination was visually observed to grow from the insert. iii) *Maximum load (MAX)*, the highest load observed by the composite during the test as obtained from the load-displacement plot.

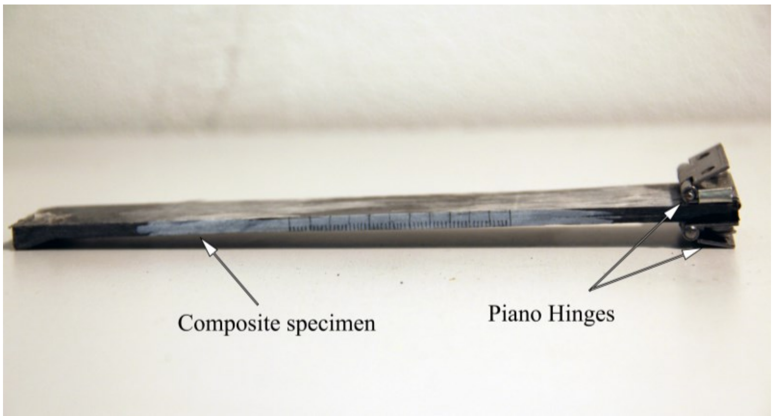

a)

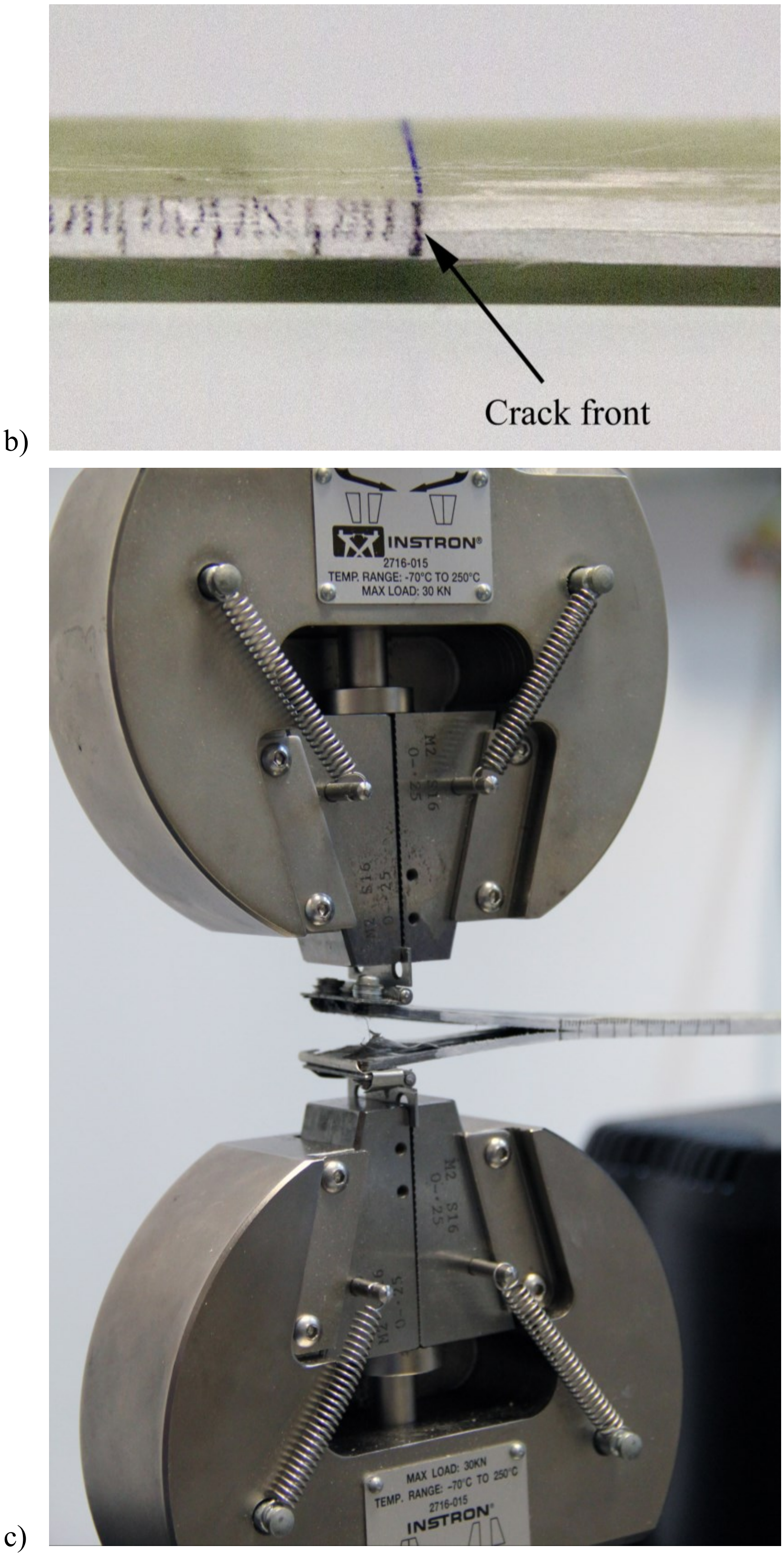

Figure 3.20. a) Composite specimen attached with piano hinges b) a close up of the crack front created by the thin Teflon sheet inserted during fabrication, c) Testing configuration in opening mode (Mode I).

3.4.6 Functional properties testing

3.4.6.1 Electrical resistivity

Two different resistivity measurement methods were employed depending on the electrical behavior of the investigated materials. For specimens having resistivity levels exceeding 10^6 Ωcm, the electrical resistivity was measured using a Keithley 8009 resistivity test chamber coupled with a Keithley 6517A high-resistance meter. In all other cases of more conductive samples, a 6-1/2-digit electrometer/high resistance system (Keithley model 6517A) was used and a 2-points electrical measurement was chosen as test configuration due to its simplicity and similarity to real applications (**Figure 3.21**).

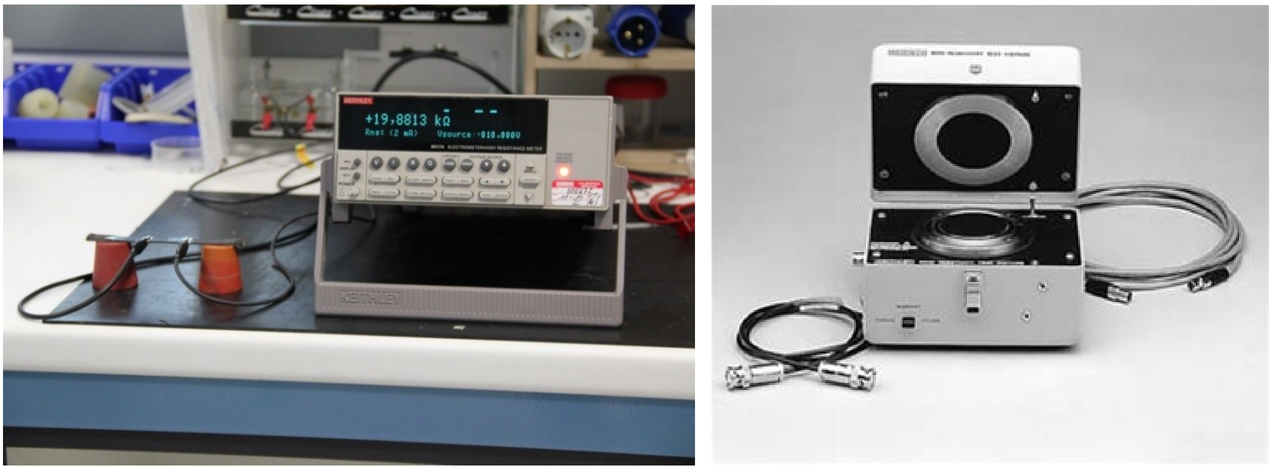

Figure 3.21. Electrical characterization instruments, Left: Keithley 6517A electrometer. Right: Keithley 8009 resistivity test fixture.

3.4.6.2 Piezoresistivity

The piezoresistivity of the conductive composite specimens, which is the change of resistance upon the application of mechanical strain, was investigated by testing the composite specimens (80 mm × 13 mm × 1 mm) in different mechanical loading conditions (tensile, flexural) using the Instron® 5969 and simultaneously measuring the absolute resistance of the specimens by mounting the electrometer (Keithley 6517A) on the specimens as shown in **Figure 3.22**. A home-made software was used to record the readings of electrometer during the test.

A gage factor (k) was calculated by using the formula shown in Equation 3-5

$$k = \frac{\left(\Delta R / R_o\right)}{\varepsilon} \tag{3-5}$$

The gage factor (k) can also be expressed as following:

$$k = \frac{\Delta R / R_o}{\varepsilon} = \frac{\Delta \rho / \rho_o}{\varepsilon} + \left(1 + 2\upsilon\right) \tag{3-6}$$

where $\Delta\rho/\rho_o$ is the material property where as ν is the Poisson's ratio of the specimen which was calculated to be 0.36 by using biaxial extensometer.

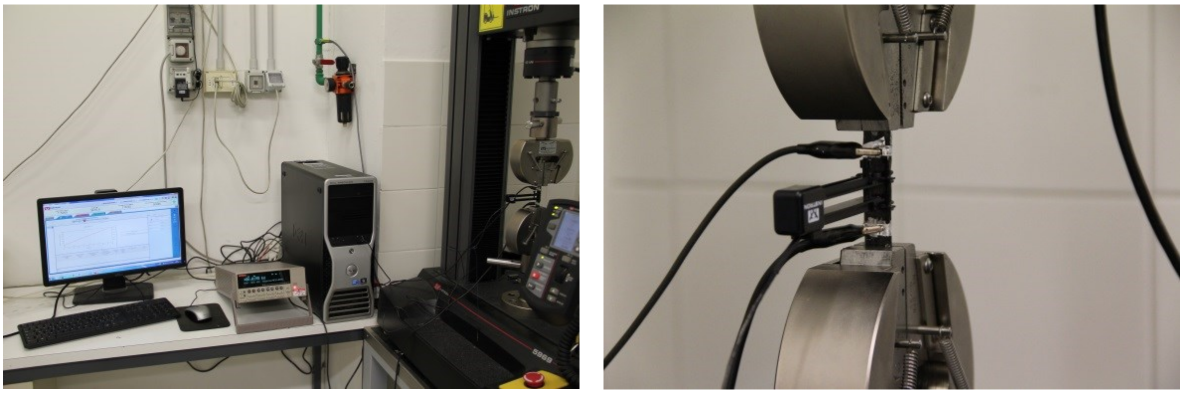

Figure 3.22. Piezoresistivity analysis setup on conductive composite specimens.

3.4.6.3 Dielectricity

The measurement of relative permittivity and dielectric loss of the composites (uncoated and graphene reinforced composites) were performed by an Agilent 4284A impedance analyzer in the frequency range from 20 up to 10^6 Hz. The size of the specimens were around 10mm × 10mm × 1.5mm and an aluminum foil was used as conductive electrode plates placed on the top and below of the specimen to create the parallel plate testing configuration.

3.4.6.4 Thermal conductivity

For investigating the effect of continuous interphase along the fiber length in the case of thermal conductivity measurements, three different sample types were prepared with respect to fiber orientation for composites containing uncoated and coated GF (GO and rGO). Considering the directions of composites defined as shown in **Figure 3.23**, composite specimens containing fibers oriented in the thickness direction were prepared which were designated as x-axis (**Figure 3.24**). The significance of this sample type was to test the effect of oriented interphase on the thermal conductivity in the composites specimens. With respect to other directions that do not contain continuous interphase, other sample type were prepared in which the fibers were along the length of the specimen termed as y-axis and z-axis. The difference being that along the y-axis, the composite specimen was compressed by applying a constant load (as described in **section 3.3.2**) which contains high fraction of fibers as compared to z-axis which did not experience any load during curing process. The reason to create such specimens was to see if the compression along y-axis could had resulted in the creation of continuous network of nanofiller capable to conduct thermal energy through the composite specimen.

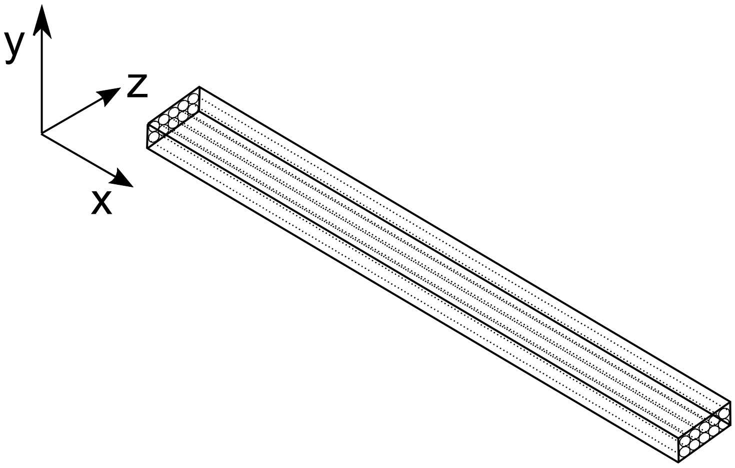

Figure 3.23. Description of directions in terms of orientation of thermal conductivity measurement.

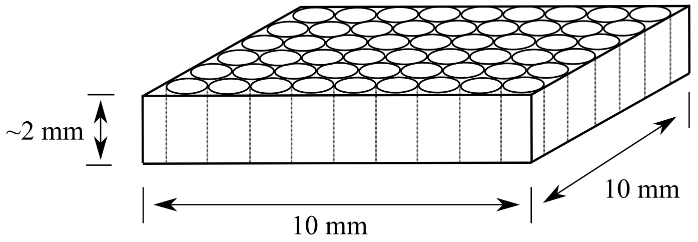

Figure 3.24. Schematic diagram of composite sample with fibers along the thickness direction of the specimen (x-axis).

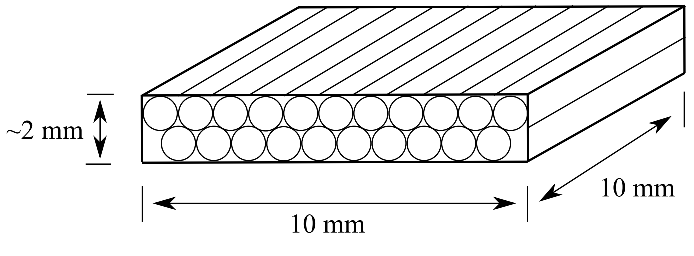

Figure 3.25. Schematic diagram of composite sample with fibers along the length direction of the specimen (y-axis and z-axis).

Thermal conductivity measurements were performed by Netzsch Laser Flash Analysis LFA 447. In this method, one side of a specimen with dimensions (10mm × 10mm × 2mm) was exposed to an energy pulse from a light source (laser or xenon flash lamp) [178] and measuring the temperature history on the other side using a liquid nitrogen cooled infrared detector. Three different temperatures were selected to measure the thermal conductivity of the specimens i.e. 25, 50 and 75 °C performing 3 shots respectively. The data was analyzed using the software Proteus. Cowan method was used to calculate thermal diffusivity (α) with pulse correction. A standard Pyrex 7740 reference material prepared according to ASTM-E 1461 was used to determine the heat capacity (c_p) and then was compared with the samples. Sample density (ρ) was determined by measuring the mass and volume of the specimen. In this way the thermal conductivity (λ) was calculated using the following equation (3-7):

$$\lambda = \alpha \times \rho \times c_p \tag{3-7}$$

Chapter 4 - Results and discussion

4.1 Characterization and testing of epoxy matrix

4.1.1 Differential scanning calorimetry (DSC)

The glass transition temperature (T_g) of cured epoxy resin (~3h at room temperature and 15h at 60°C) was obtained by performing DSC analysis. **Figure 4.1** shows the thermogram obtained during the DSC ramp and the T_g evaluated as the inflection point was 33°C. The main advantage to use an epoxy resin with such low T_g was to have a soft epoxy matrix capable of being tested in single fiber fragmentation test (SFFT) because the optimum condition is to have strain failure of matrix to be at least three times than that of the embedded fiber [179].

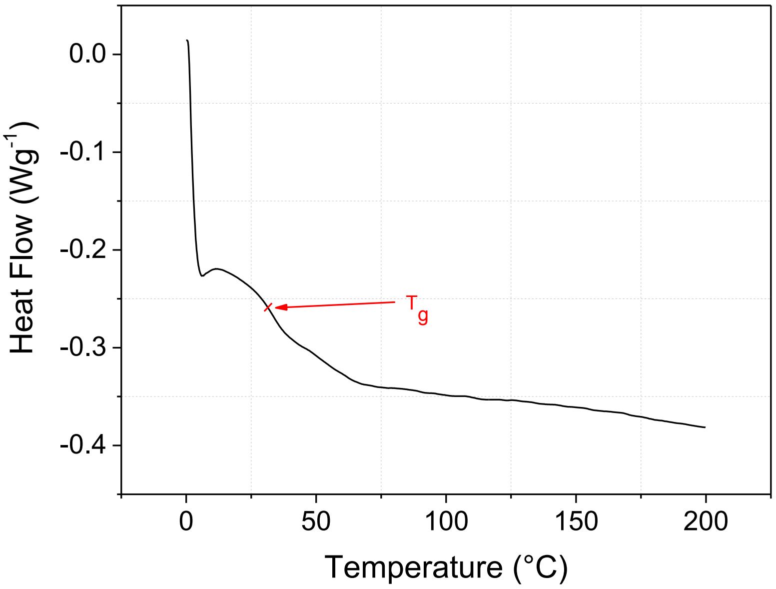

Figure 4.1. DSC thermograms of neat cured epoxy resin.

4.1.2 Thermogravimetric analysis (TGA)

Figure 4.2 shows the thermogram obtained during the TGA ramp between 25 to 700°C at a heating rate of 10°C/min The onset of degradation temperature ($T_{d,onset}$) was evaluated by the intersection point of the tangents to two branches of the thermogravimetric curve, while the maximum rate of degradation temperature ($T_{d,max}$) was determined from the peak maxima in the first derivative of weight loss curve.

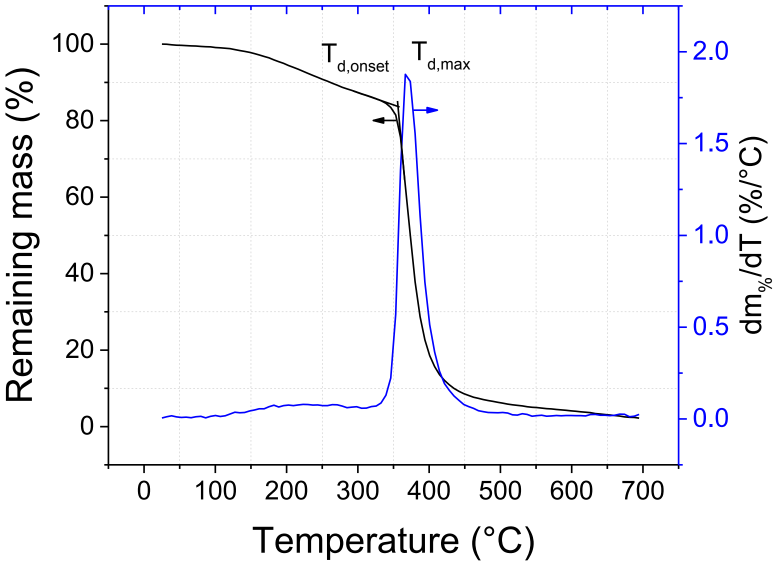

Figure 4.2 Thermograph of epoxy, showing the thermogravimetric curve (left y-axis) and the first derivative of weight loss curve (right y-axis).

4.1.3 Mechanical properties

The mechanical properties obtained by tensile testing of the cured epoxy resin (**Figure 4.3**) are summarized in **Table 4-1**.

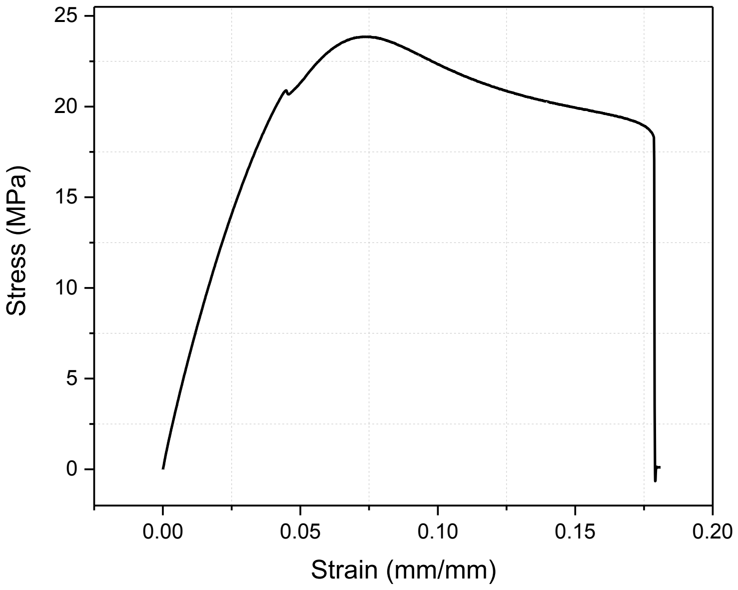

Figure 4.3. Representative stress-strain curve of cured epoxy resin obtained through tensile test.

Table 4-1 Mechanical properties of cured epoxy resin.

Physical properties	**Value**
Young's Modulus (MPa)	795 ± 28
Tensile strength (σ_y) (MPa)	26.47 ± 4.21
Stress at break (σ_b) (MPa)	19.77 ± 2.26
Strain at break (ε_b) (mm/mm)	0.17 ± 0.04

4.1.4 Dynamic mechanical thermal analysis (DMTA)

The dynamic mechanical properties of the epoxy matrix obtained (**Figure 4.4**) are summarized in the **Table 4-2**.

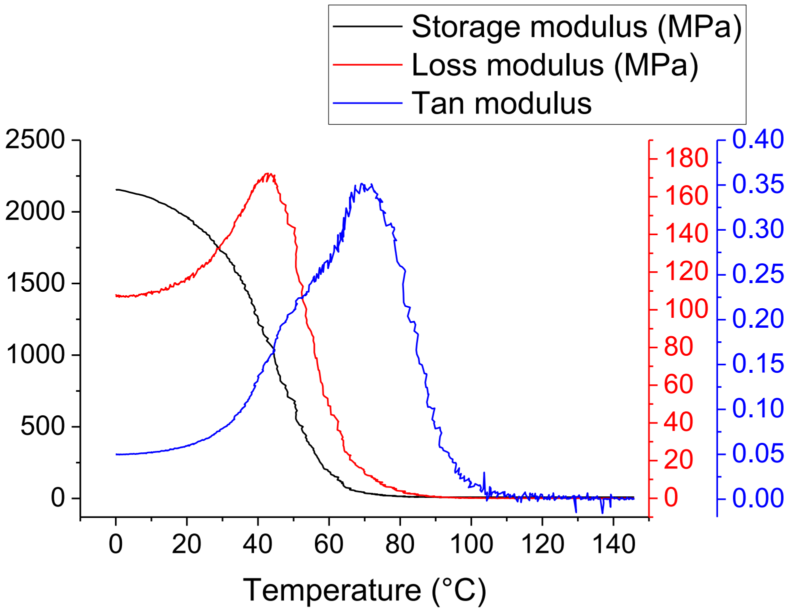

Figure 4.4. Dynamic mechanical properties of epoxy matrix.

Table 4-2 Results of DMTA test on epoxy matrix.

Dynamic mechanical property	**Value**
Storage modulus E' (0°C)	2152 MPa
Storage modulus E' (23°C)	1895 MPa
Loss modulus E" (23°C)	121 MPa
Tan delta peak value	0.34
T_g at Loss modulus peak"	42°C

4.2 Characterization and testing of glass fiber

4.2.1 Density measurement

As received GF were weighed prior to measuring their density using helium pycnometry technique. Around 0.65g of GF were inserted in a testing chamber of 3.5cm^3 and using helium as a displacement fluid, apparent density was measured by performing around 300 measurements consecutively which gave an average density of 2.55 g/cm^3. The distribution of density measured against the measurement number is plotted in **Figure 4.5**.

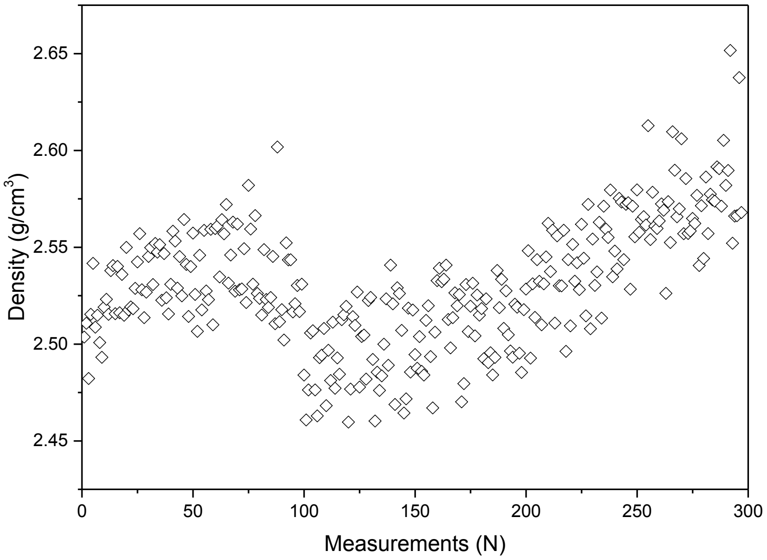

Figure 4.5. Density of glass fiber measured through a Micromeritics®Accupyc 1330 helium pycnometer (23°C) with 3.5cm^3 chamber.

4.2.2 Diameter measurement

A composite (based on clean fibers bonded in epoxy matrix) was cut and polished across its cross-section and it was observed under FESEM as shown in **Figure 4.6**. The diameter of each fiber was measured using software (ImageJ) and the size distribution against their count is represented in a bar chart shown in **Figure 4.7**.

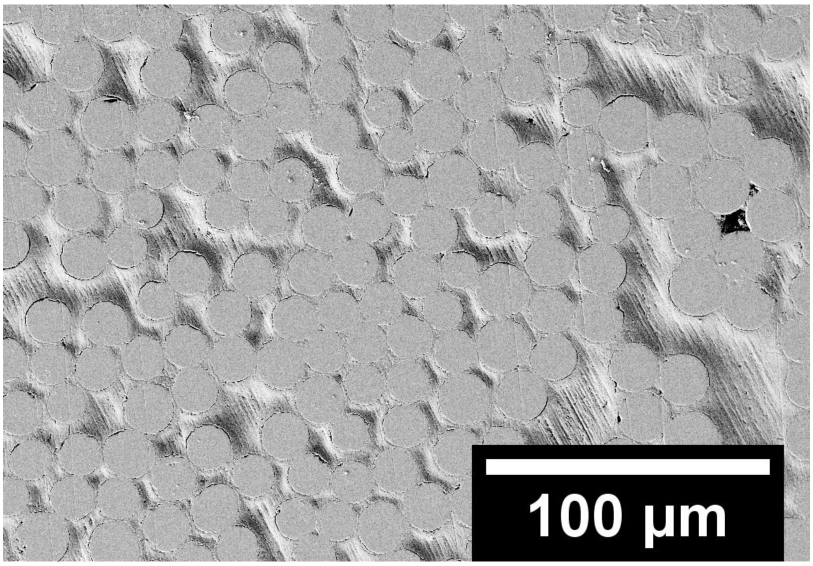

Figure 4.6. Cross-sectional view of uncoated fiber reinforced epoxy composite observed using FESEM.

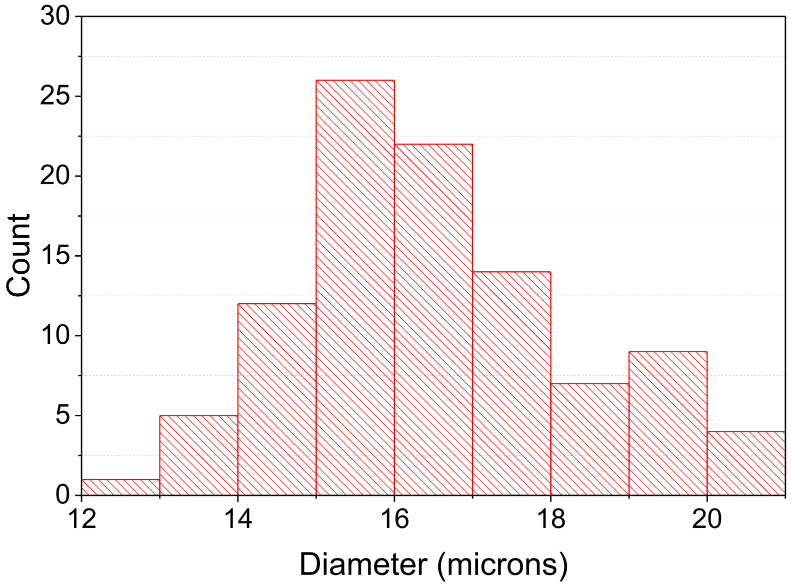

Figure 4.7. Size distribution of glass fiber diameter.

4.2.3 Strength evaluation

Tensile strength was determined using a statistical treatment on the Weibull distribution. Particularly, the iterative procedure by Gurvich et al. [176] has been adopted to determine the shape (m) and scale (σ_0) parameters. **Figure 4.8** represents the plot of the failure probability as a function of fiber strength along with the fitting line whereas **Table 4-3** summarizes the parameters determined by using this approach:

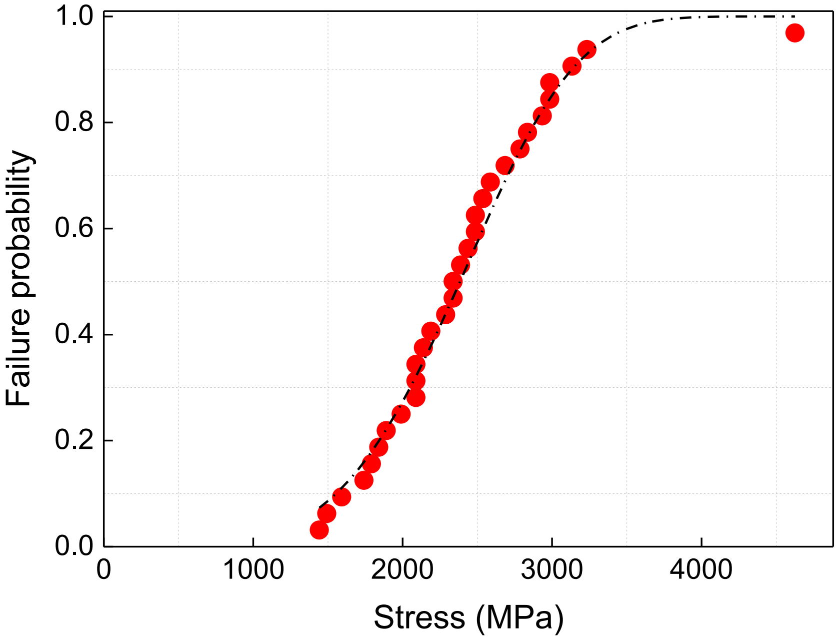

Figure 4.8. Plot of the failure probability as a function of applied stress along with the Weibull fitting curve.

Table 4-3. Tensile strength parameters of GF as determined from single fiber tensile tests.

Parameter	***Value***
Number of specimens (N)	*31*
Young's modulus	*85.3 GPa*
Average strength at L = 20 mm ($\bar{\mathbf{R}}$)	*2402 MPa*
Scale parameter (σ_o)	*3551 MPa*
Shape parameter (m)	*4.4*
Coefficient of variation (v)	*26.3%*
Strain at break (%)	*3.34 ± 0.8*

4.3 Characterization of synthesized graphene nanosheets

4.3.1 X-ray diffraction (XRD)

As reported in **Figure 4.9**, X-ray diffractograms of precursor graphite shows a characteristic and intense peak (0 0 2) at 26.4° thus confirming the crystalline nature of typical graphite powder (**Figure 4.9**a). The oxidation reaction of graphite powder in modified

Hummer’s method replaced the (002) peak by a (001) diffraction peak of GO (**Figure 4.9b**). The peak shift was due to the increased interlayer spacing of graphite layers due to the insertion of oxygen based functional groups in GO as well as water molecules [180]. Finally, the rGO diffractogram exhibits a peak repositioned back to the pristine graphite peak location due to the removal of most of the oxygen groups from GO, hence decreasing the interlayer spacing (**Figure 4.9c**). Note that both GO and rGO peaks are much less intense and broader due to amorphous/distorted nature hence confirming the occurrence of the exfoliation process.

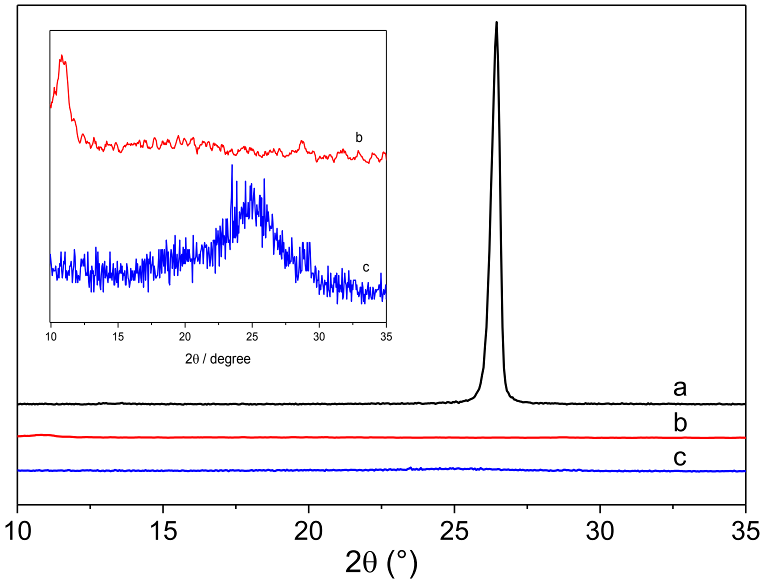

Figure 4.9. X-ray diffractograms of (a) graphite, (b) GO and (c) rGO. The internal box shows the magnified picture of diffractograms of (b) GO and (c) rGO.

4.3.2 Fourier transform infrared spectroscopy (FTIR)

The FTIR spectra of graphite, GO and rGO are shown in **Figure 4.10**. As compared to pristine graphite, GO shows relatively intense peaks associated to groups like O-H, C=O and C-O at wavenumbers approximately 3830 cm^{-1}, 1625 cm^{-1} and 1085 cm^{-1} respectively that confirms the destruction of original extended conjugated π-orbital system of the graphite and insertion of oxygen-containing functional groups into carbon skeleton (**Figure 4.10a,b**). However after chemical reduction, a lowering in the intensity of the functional groups peaks of rGO spectra confirms the removal of oxygen-containing groups (**Figure 4.10c**). It is interesting to know that complete reduction was not possible through traditional reduction methods hence oxygen was not completely removed from rGO.

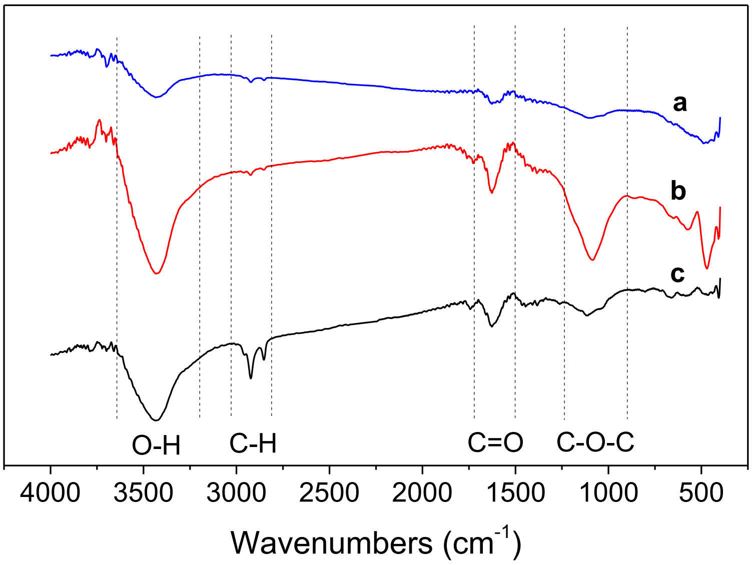

Figure 4.10. Spectra of Fourier transform infrared spectroscopy of (a) graphite, (b) GO and (c) rGO.

4.3.3 Scanning electron microscopy (SEM)

Exfoliation of GO sheets can be seen in **Figure 4.11** as observed from FESEM analysis. The sheets, being of different layered thickness, are several micrometers in lateral size with the characteristic wrinkling of nanosheets which is a common phenomenon among thin films and membranes.

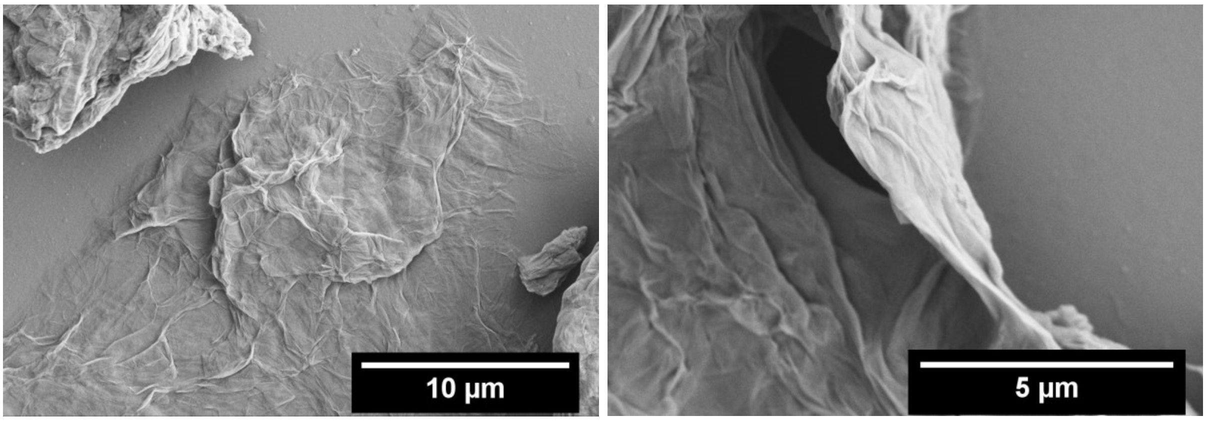

Figure 4.11. FESEM images of GO nanosheets.

4.3.4 X-ray photoelectron spectroscopy (XPS)

Figure 4.12 displays the XPS spectra of both GO and rGO samples that provide the information of the surface chemical composition. The C1s XPS spectrum (**Figure 4.12a**) of GO reveals a certain degree of oxidation with at least three oxygen functional groups attached to the carbon skeleton, namely the carboxyl group (COOH), the C in C-O bonds and non-oxygenated carbon (C-C). The semi-qualitative results for the carbon and oxygen present on the specimen surface were also measured using the atomic sensitivity factors, where the oxygen carbon distribution resulted to be 34% and 66% respectively (**Table 4-4**). XPS spectrum of rGO also confirms the presence of the same functional groups present in the sample but with reduced intensity of the peaks of oxygenated groups (**Figure 4.12b**). The addition of a new C-N group in rGO spectrum is obvious due to the fact that the chemical reduction of GO took place in the nitrogen-rich environment of hydrazine hydrate. The percentages of oxygen and carbon on the specimen surface came out to be 10% and 90% respectively (**Table 4-4**), hence confirming a successful reduction of GO.

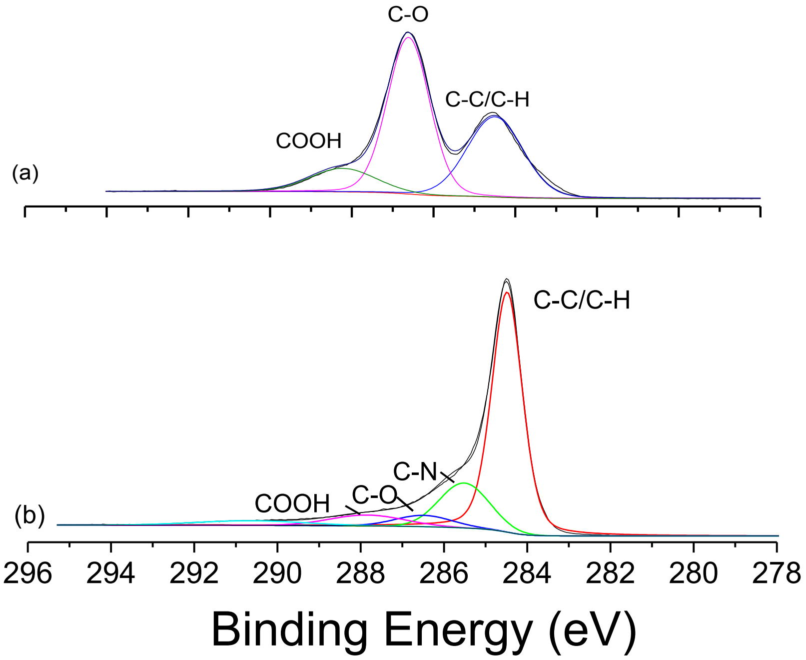

Figure 4.12. The C1s spectra of (a) GO and (b) rGO.

Table 4-4. Elemental analysis of GO and rGO specimens obtained through XPS analysis.

Sample	O (%)	C (%)
GO	34.2	65.8
rGO	9.9	90.1

4.4 Characterization and testing of graphene coated fibers

4.4.1 Scanning electron microscopy (SEM)

The electrophoretic deposition of GO and rGO on GF can be practically confirmed using FESEM observations. In **Figure 4.13**, an overview of the surfaces of uncoated, GO and rGO coated GFs at various electric deposition applied fields is presented. When the applied deposition field was increased from 2.5 V/cm to 10 V/cm, the GO coating deposited on GFs appeared to be more and more thick and uniform.

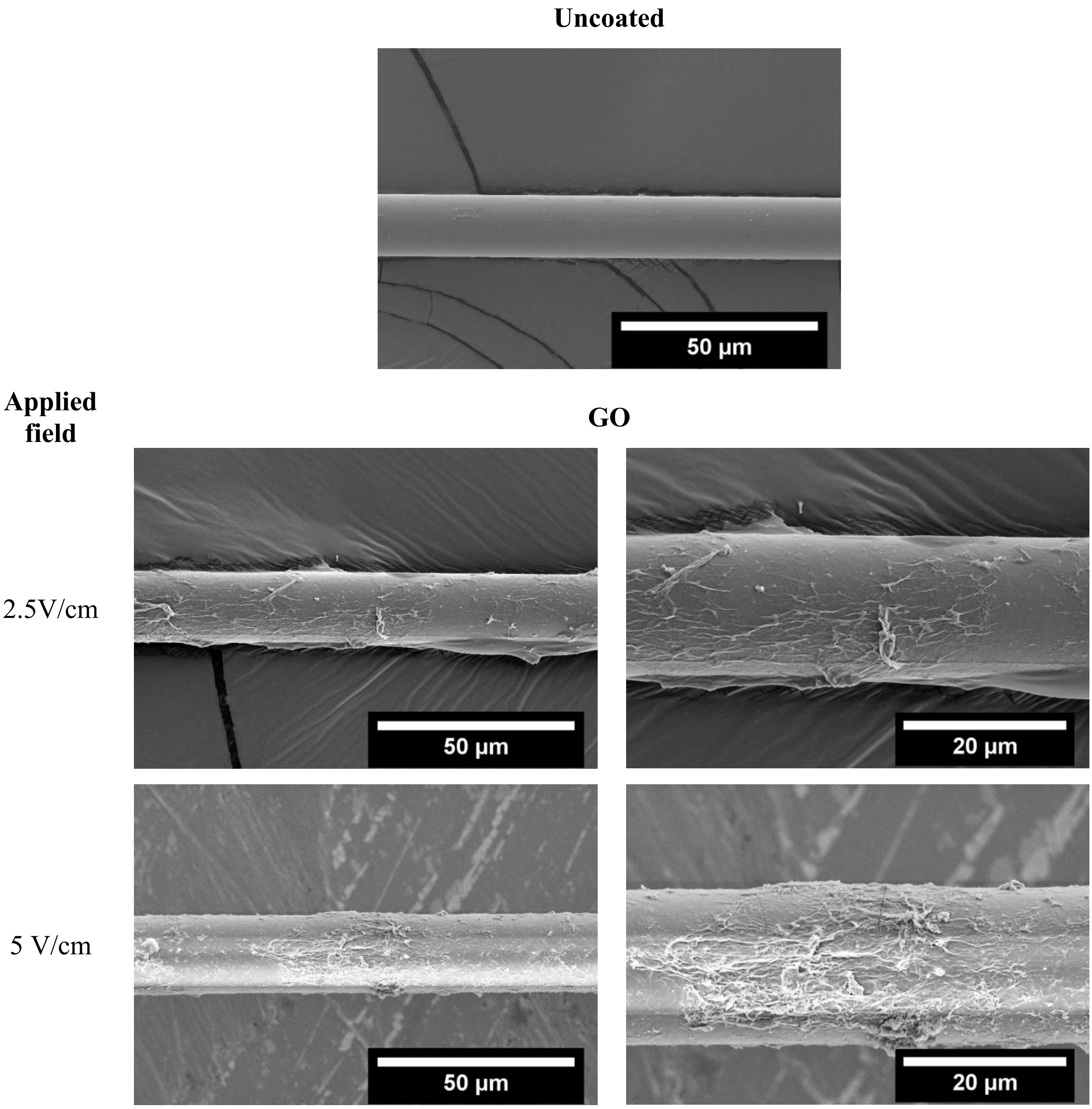

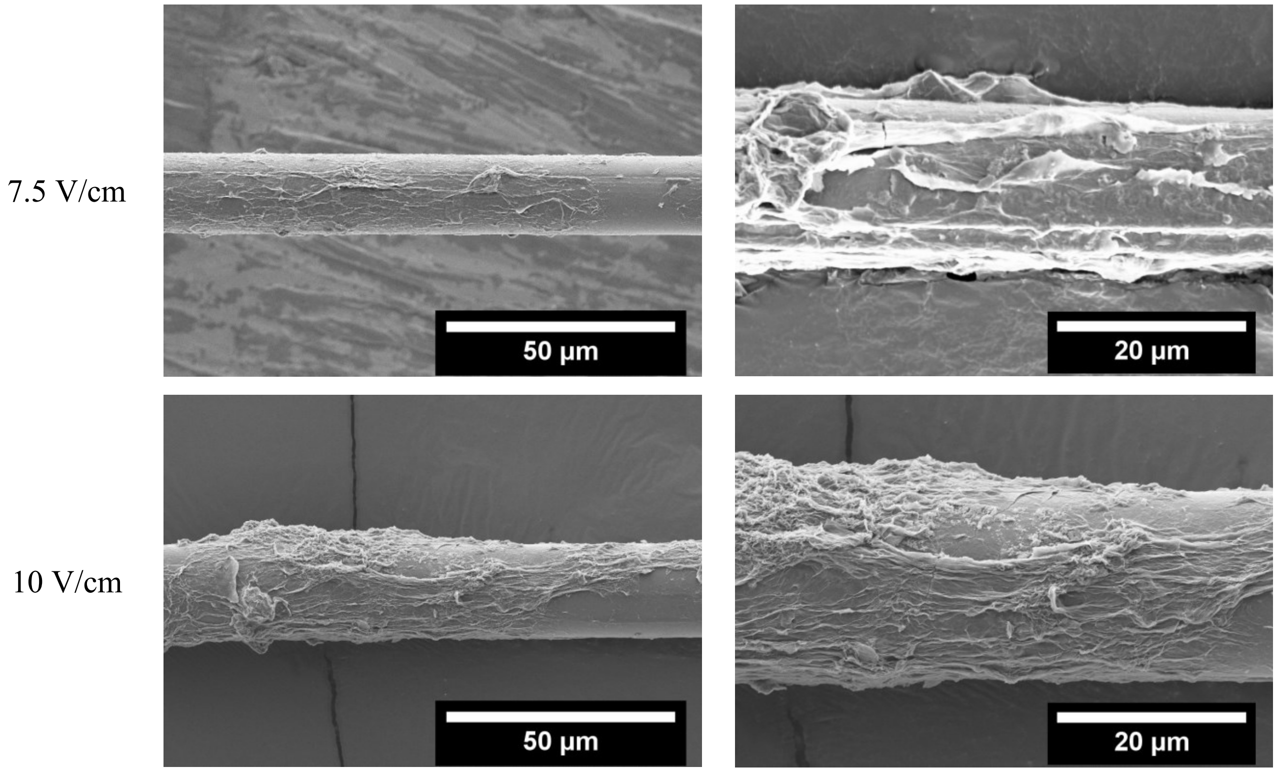
7.5 V/cm
50 µm
20 µm
10 V/cm
50 µm
20 µm

rGO

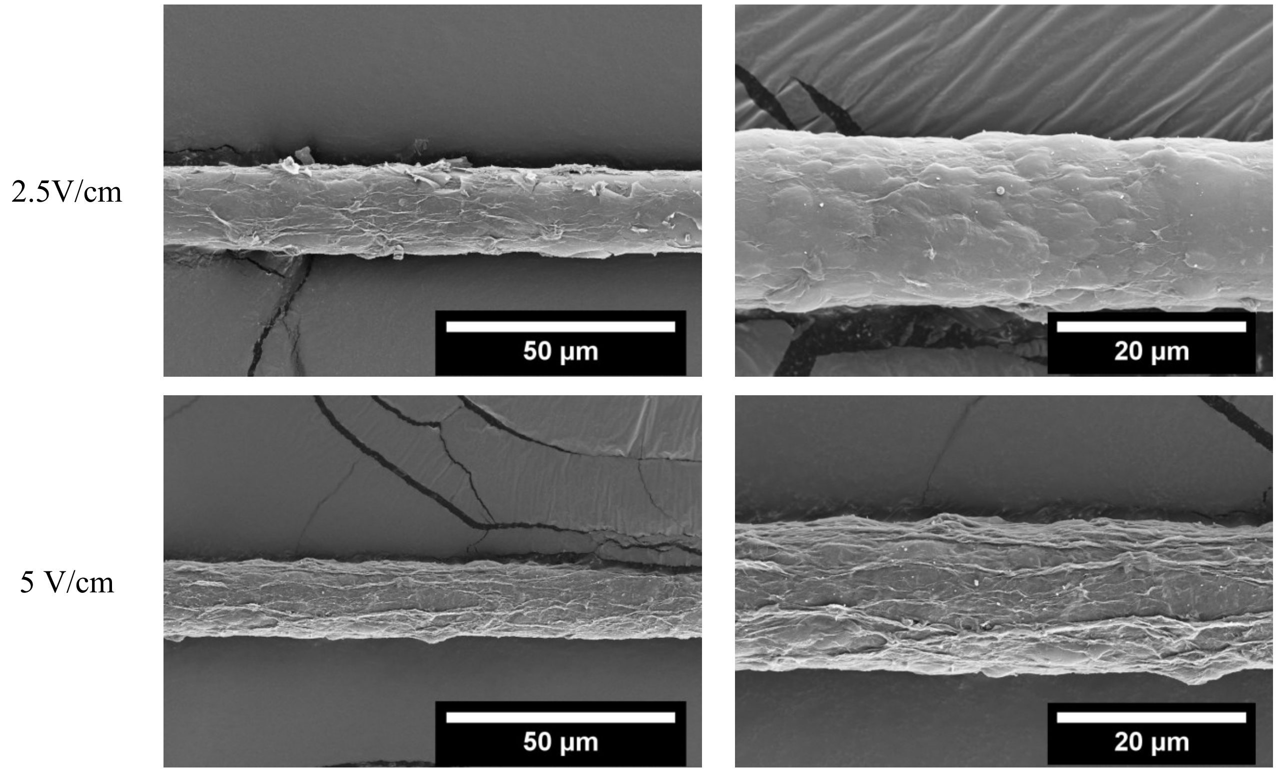
2.5V/cm
50 µm
20 µm
5 V/cm
50 µm
20 µm

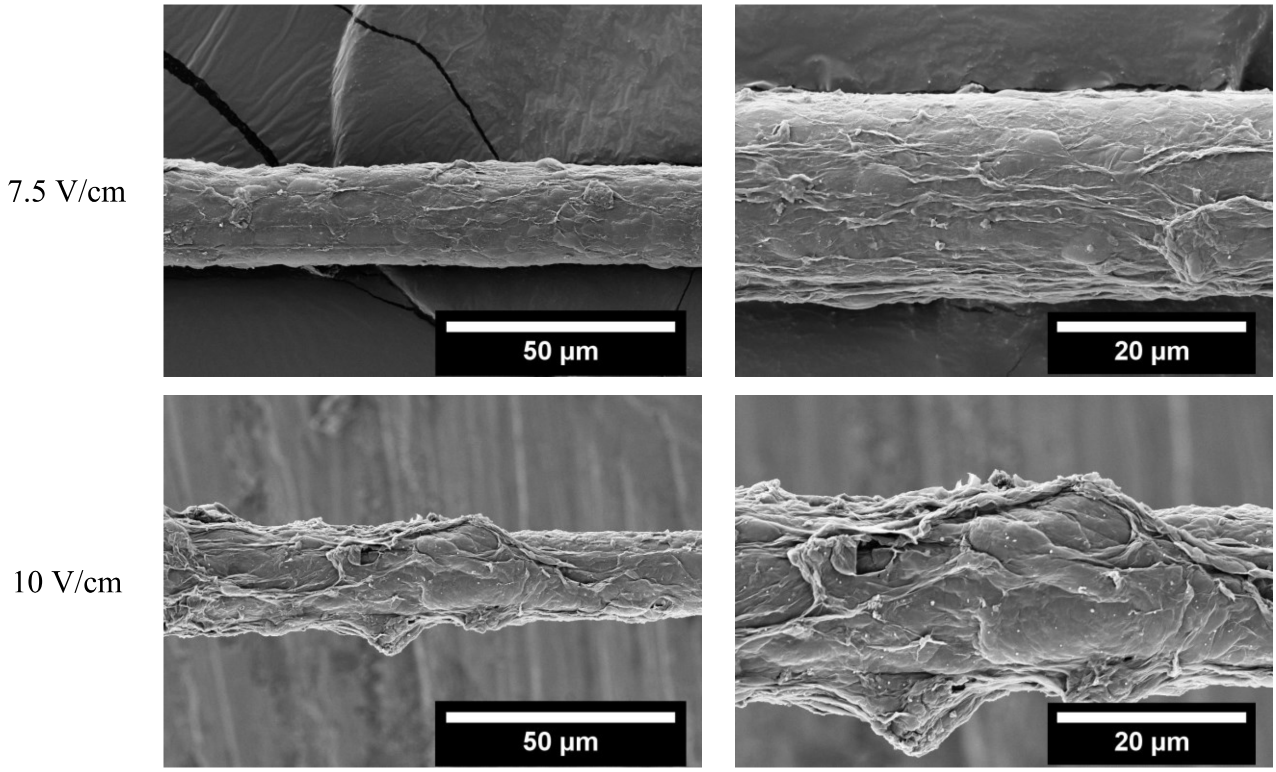

Figure 4.13. FESEM pictures of GF coated with GO and rGO with respect to different applied fields. Note: 0 V/cm refers to condition in which GF was not subjected to EPD process.

The amount of GO deposited on the GFs was estimated by weighing the GF bundle before and after the EPD process. The rate of weight increase of the GF bundle is reported in **Figure 4.14** as a function of the deposition voltage. It is worthwhile to note that a linear correlation between the deposition rate and the intensity of the electrical field can be observed. The linear fit of average values (line in **Figure 4.14**) indicates a rate of weight increase of GO on GFs of 0.00133 ± 0.00003 % cm min^{-1} V^{-1}. A similar trend was observed also by An et al. [181] who studied the EPD process of CNTs onto E-glass fibers fabrics. In fact, a mass change of the E-glass fabric linearly increasing with the applied electrical field used for the EPD of CNTs was reported.

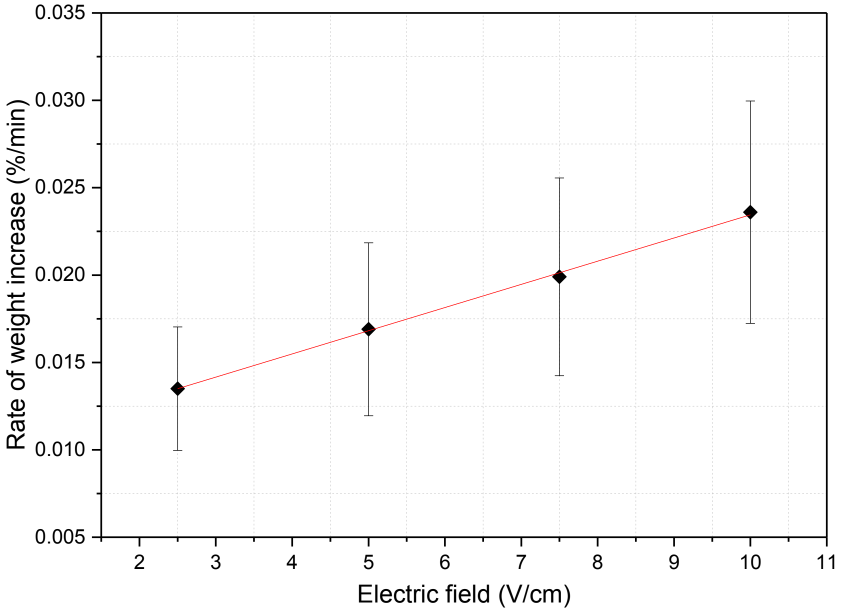

Figure 4.14. Rate of weight increase of GO coated glass fiber as a function of the applied electric field used during the EPD process.

4.4.2 Atomic force microscopy (AFM)

a) Roughness measurement [173]

The intermittent contact mode in AFM was used to investigate and calculate the variable thickness and roughness of GO/GF on topographic images such as that reported in **Figure 4.15**. As interpreted by the color bar, the bright color shows thicker GO where the four different regions (1, 2, 3 and 4) have been chosen arbitrarily for roughness measurements, and the resulting values are reported in **Table 4-5**. It appears that the GO coating was not homogenously distributed and the thicker regions, like in region 2 and 3 have considerably higher roughness as compared to other regions.

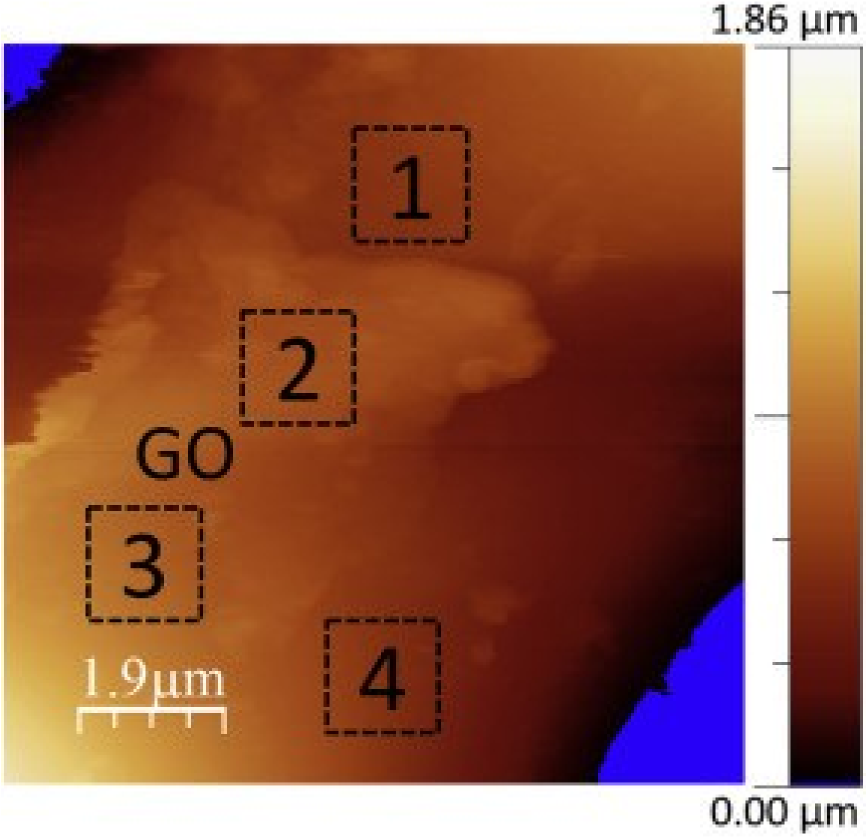

Figure 4.15. Topographic AFM image (height channel) shows GO on glass, scale bar shows different thickness of GO. Regions 1–4 are randomly chosen (1.5 μm^2) to carry out roughness measurements as given in **Table 4-5** [173].

Table 4-5. Roughness measurement of four marked locations [173].

Marked areas number	Roughness average Ra (nm)	Root mean square RMS (nm)
1	8.216	10.72
2	58.300	20.05
3	3.198	4.04
4	2.797	3.56

b) Delamination of GO over GF [173]

Friction force microscopy (FFM) technique was employed to delaminate GO over GF. The delamination was initiated from a significant edge interface between GF and GO, a schematic diagram of which is shown in **Figure 4.16a**. The black and brown regions are the surfaces of GF and GO respectively. The scanning pattern of the cantilever probe (slider) makes a fast scan along the x-axis while progresses slowly in the y-axis direction, as depicted by the yellow dashed lines. The first scan carried out was at relatively low F_N value in order to collect morphological information of the area where FFM was to be carried out. The force applied at low F_N deforms the coating elastically but when F_N was increased, a permanent deformation of the GO nanosheets was observed. **Figure 4.16b** and **Figure 4.16c** are F_L maps (recorded from the torsional movement of the cantilever) carried out at two different F_N values of 0.753 μN and 3.7 μN, respectively.

The resistance offered by the GO and/or GF surfaces in relative motion gives the cantilever the torsional bending. It was observed that different F_L signals were observed at fixed F_N due to different angular interactions with tip apex and thickness of GO. In this work, we will consider only the fixed angle (i.e. 90°) interaction between GO and fast scan direction of probe. In **Figure 4.16b** and **Figure 4.16c**, the bright colors show higher F_L obtained at the edges of GF while the quantitative value of F_L is plotted in **Figure 4.16d** where line profile was carried out from GF to GO covered regions. It shows the cantilever's encountering of the constant lateral force F_L along E-glass surface until F_L suddenly increases as indicated by a vertical black line. Higher values of F_L are required as the cantilever starts penetrating through the GO due to additional force required to scratch the layers of GO from the GF as well as to destroy the bonds between inter and intra layer of GO. The area under the curve of lateral force displacement plot can be considered as a total dissipated energy (E_{DISS}).

This lateral force (F_L) comprised of the contribution from glass substrate (F_S), from interlayer adhesion between GO layers (F_{IL}) and from interfacial adhesion between GO and GF (F_{IF}), which can be shown as an Equation 4.1:

$$F_L = F_{IL} + F_{IF} + F_S \tag{4-1}$$

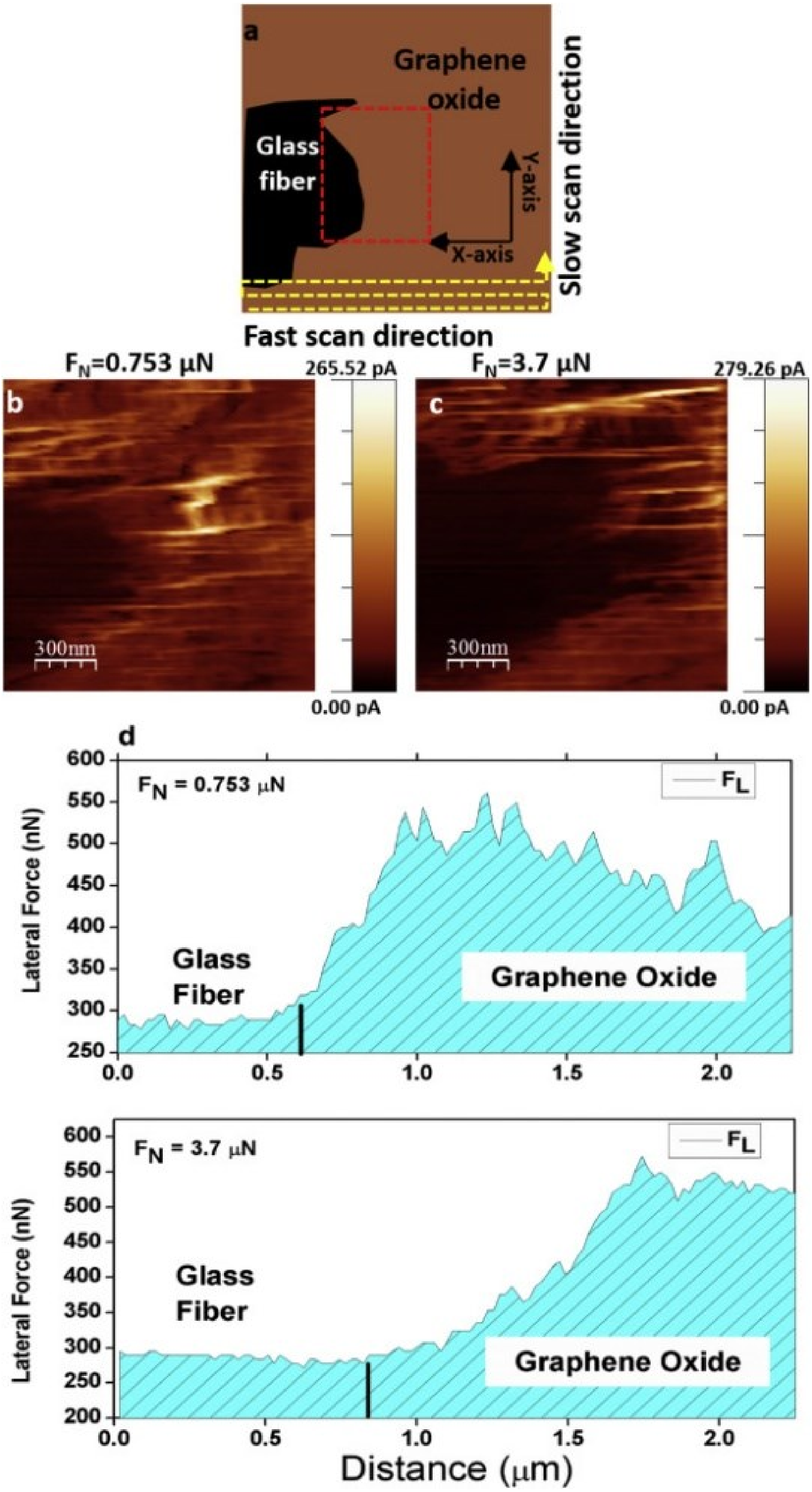

Figure 4.16. a) Schematic view of glass substrate (black color) and GO covered glass regions (brown) mimics the F_L map given in b) and c). Yellow dashed line shows raster scanning pattern of AFM probe in X and Y directions. b) and c) show FL map of same region.

Removing the contribution from glass friction (F_L-F_S), gives us the remaining contribution from interlayer and interfacial adhesion which is used to measure the shear strength of the GO/GF interface. F_L-F_S was measured to be 303 nN for current thickness (h ≈ 22 nm) of GO, scratch length (l = 1.45 µm) and width (b = 102 nm). Such case is only possible when i) FFM was carried out under switch-off feedback loop, else the cantilever will follow the topography of GO instead to ploughing and ii) the substrate (GF) offers lower lateral force value than the coating layer (GO). The coefficient of friction (f_{cof}) measured for GF and GO were 0.07 and 0.15 respectively. This case favors the delamination of the coating rather than producing a significant wear of the substrate [182]. **Figure 4.17** reports AFM images of scan size 5 × 2 μm^2 in tapping mode for topography (**Figure 4.17a**) and phase channel (**Figure 4.17b**) reveal the delamination of GO after FFM operations. It indicates that the debris of the GO gathered at periphery of FFM analyzed region which was up to 3 µm in height. Moreover, the phase contrast picture of **Figure 4.17b** contains no wear scar on GF and it clearly reveals the difference between the substrate and the delaminated GO. In addition, no peeled-off GO was accumulated to the cantilever tip apex which gives us the information that the failure of the interface could be either adhesive or cohesive. For adhesive failure, the failure front propagates strictly at the interface whereas for the cohesive failure just below or above the interface within one phase [183]. Normally, smaller adhesion/cohesive strength ratio (below 1) lead to "flaking" (adhesive failure) whereas for larger (than 1) values would cause "chipping" (cohesive failure) [184]. The smaller size of scratch width rendered it difficult to discriminate between the two different mechanisms. At nanoscale level, Aoyama et al. [184] described abrasion characteristics for adhesive or cohesion failures of thin films (few nanometers) by examining the debris obtained after scan. In this case of GO coating over GF, wear response was characterized as reported in **Figure 4.17**. It shows significant shear displacement of GO along the scanned region and the debris, collected up to 3 µm (**Figure 4.17a**), at the periphery of this scanned region. The phase contrast allow us to distinguish between GF and GO debris. This suggests that GO over GF exhibited predominant adhesive rather than cohesive failure in this work and under certain loading condition (normal force of 3.7 µN).

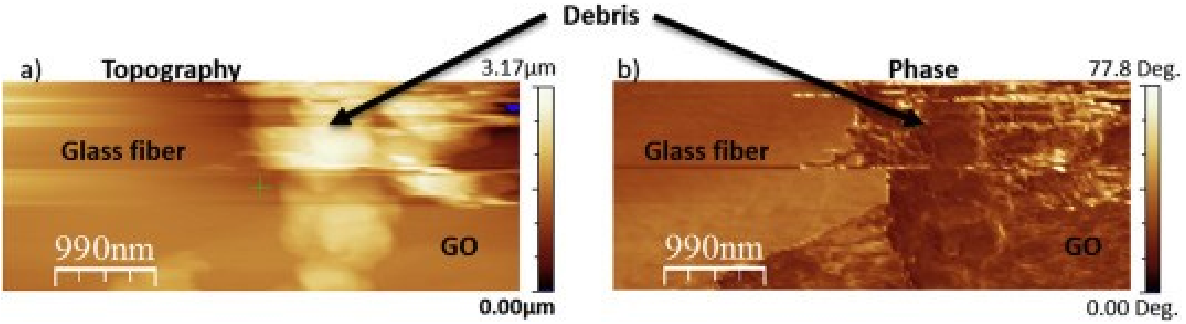

Figure 4.17. AFM image of scan size 5 × 2 µm2 in tapping mode for topography (a) and phase channel (b) shows delamination of GO after FFM operations.

Critical normal force (F_N = 3.7 µN) at which permanent deformation of GO occurred also produced the measured net shearing force F_L-F_S. From the work done by this force and from the analysis of the delaminated area, the energy dissipated per unit area (2Γ) can be evaluated. Using Equation 4.2 [185] we can derive the shear strength, namely:

$$2\Gamma = \frac{E_{DISS}}{A} = \frac{1}{2}\frac{\left(\tau + Pf_{cof}\right)^2 h}{G_a} \tag{4-2}$$

where E_{DISS} is the total energy dissipated (4.39×10^{-13} Nm) during delamination under cantilever probe, which travelled through 1.45 µm, A is the area of delamination, G_a is the shear modulus of the interface, P is the pressure applied and h is the thickness of GO. Assuming the condition of zero applied pressure (i.e. P = 0) in Equation 4.2, shear strength (τ) can be calculated as follows:

$$\tau\gamma = \frac{2E_{DISS}}{1bh} \tag{4-3}$$

where $G_a \approx \tau/\gamma$ is the shear modulus of the interface and the shear strain γ can be calculated as γ = arctan (y/h). Here y and h are the elastic shear displacement (y ≈ 260 nm) and thickness of GO (h ≈ 22 nm) respectively. The first one is the critical displacement that can be calculated just before rupture of GO obtained from stick-slip profile at GO edge as determined in **Figure 4.16d** at F_N = 0.753 µN. The elastic displacement of GO occurring during interaction with sliding AFM probe with relatively lower F_N recovered its original position after removal of shear force, as described by Hunley and coworkers [186]. In the same context, shear strain was calculated to be 1.4. Thus, the shear strength and hence shear modulus at zero applied pressure are calculated as $\tau_{p=0} = 1.9\times10^{8}$ N/m^2 and $G_{a,p=0} = 1.35\times10^{8}$ N/m^2. Substituting this value of G_a at applied pressure $P \approx F_N/(\pi r2) = 4.5 \times 10^{8}$ N/m^2 (where r is the AFM tip radius) in Equation 4.3, τ is recalculated as 0.13 GPa which also corresponds to the convergent solution of this iterative method.

4.5 Micro-composite testing

The microcomposites observed under optical microscope simultaneously during the SFFT showed the fragmentation of the fibers (as observed in **Figure 4.18**).

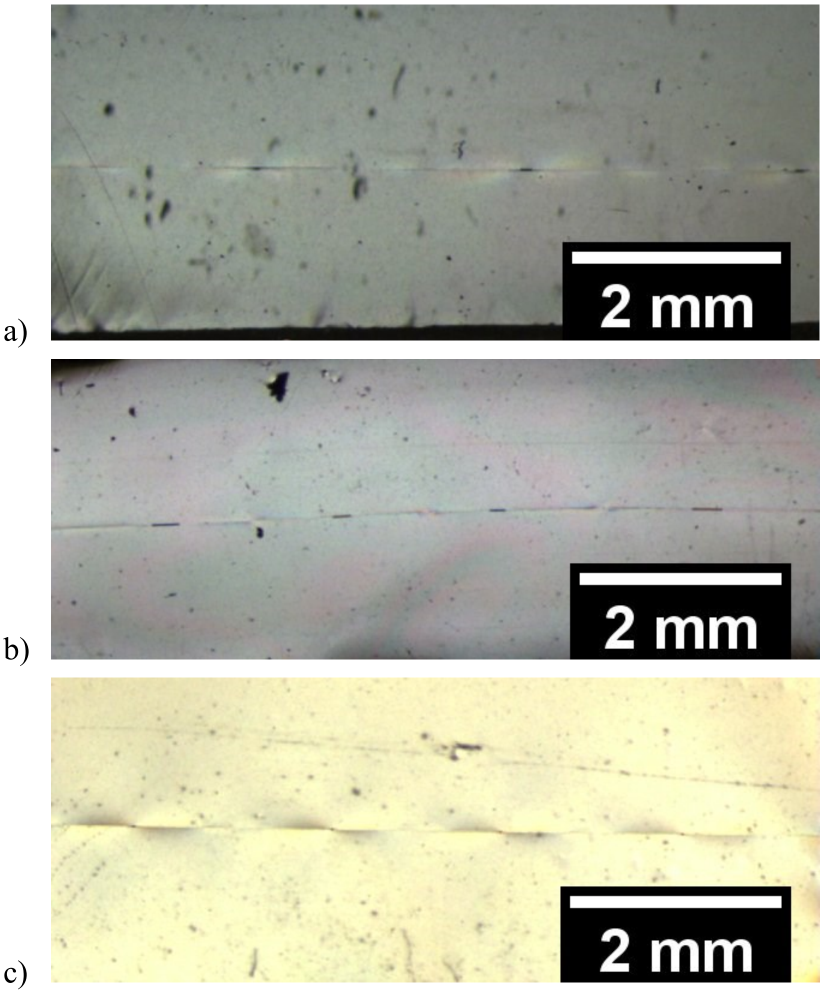

d)

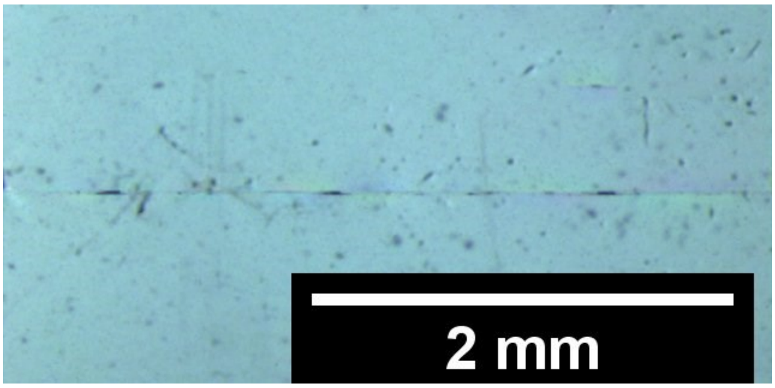

e)

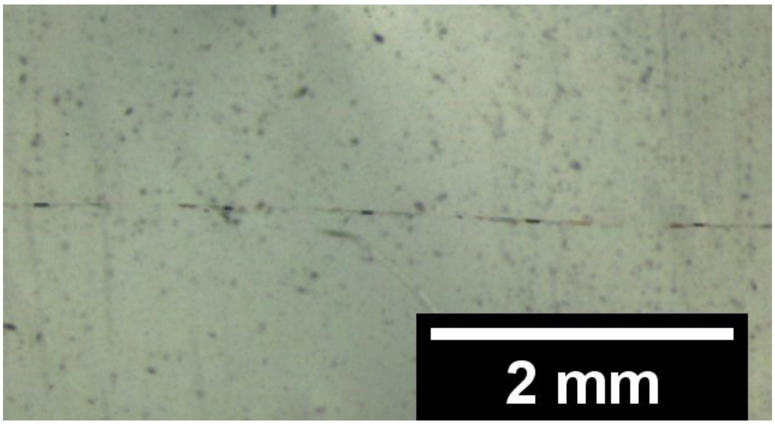

Figure 4.18. Fragments of fiber observed during single fiber fragmentation test on microcomposites containing a) uncoated GF; GF coated by GO at b) 2.5V/cm, c) 5V/cm, d) 7.5V/cm and e) 10V/cm.

The average saturation lengths of fiber fragments as determined by the SFFT of composite specimens containing uncoated fiber and coated fibers (GO and rGO) at various applied fields are reported in the **Table 4-6**. The values of average fragment lengths were used to calculate ISS values based on the simplified micromechanical model presented by Kelly and Tyson [29] and reported in **Figure 4.19** as a function of the electric field used during the EPD process. In case of GO, it can be inferred from the data that the increase in the applied voltage used during the EPD process had an effect in the enhancement of interfacial adhesion thus resulting in shortening of fragment lengths. A noteworthy improvement of 218% of ISS can be witnessed in case of GF coated with GO electrophoretically deposited at 10 V/cm. This positive effect could be partly attributed to the fact that GO creates a favorable bond between the GFs and epoxy resin due to the surface functional groups thus enhancing the effective distribution of load on the GF. In such condition, the increased surface roughness results in mechanical interlocking along with the good adhesive compatibility between the epoxy matrix and GO are both responsible for the observed increase of ISS in microcomposites [187]. On the other hand, as it can be seen from **Figure 4.19**, when the applied voltage was increased, the EPD process was more effective in producing a homogeneous and thick GO coating on the GF.

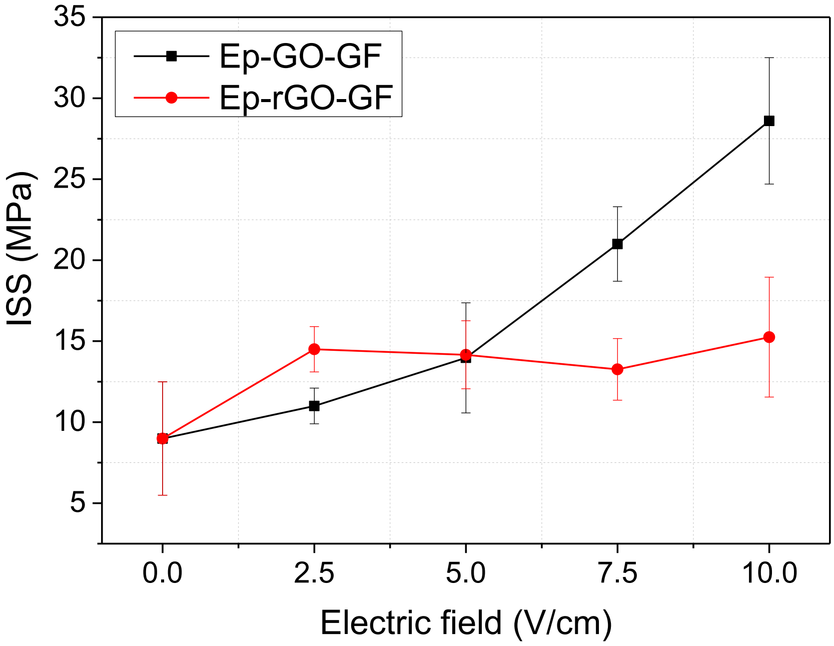

Figure 4.19. Fiber-matrix interfacial shear strength values as determined by the fragmentation test on epoxy microcomposites containing E-glass fiber coated with GO and rGO as a function of the electric field used during the EPD process.

In case of rGO coated fibers, after an initial increase, the ISS values remain almost constant as the electrical field of the electrophoretic deposition is increased and with values systematically lower than those observed in microcomposites containing GO coated fibers. This supports the hypothesis that functional groups play a major role in creating favorable bonds with the matrix. In fact, the absence of oxygen functionalities on the rGO sheets practically limits the possibility of chemical bonding between rGO and epoxy matrix. Secondly, the substantial independency of ISS values from the applied deposition voltage confirms that the main load-transfer mechanisms is based on the mechanical interlocking in this case.

Table 4-6. Effect of EPD on the fragmentation tests results.

	Fragments length at saturation L_S (mm)		**Critical length L_C (mm)**		**Tensile strength of fiber $\sigma_{fb}(L_C)$ (MPa)**		**Interfacial shear strength ISS (MPa)**	
Applied voltage (V/cm)	**GO**	**rGO**	**GO**	**rGO**	**GO**	**rGO**	**GO**	**rGO**
0 (uncoated)	2.7 ± 0.9		3.5 ± 1.2		3548.3 ± 267.5		8.9 ± 3.5	
2.5	2.0 ± 0.2	1.6 ± 0.1	2.7 ± 0.2	2.2 ± 0.2	3720.8 ± 65.4	3913.7 ± 70.4	11.0 ± 1.1	14.5 ± 1.4
5	1.7 ± 0.3	1.7 ± 0.2	2.3 ± 0.4	2.2 ± 0.3	3876.3 ± 165.1	3893.5 ± 107	13.9 ± 3.4	14.2 ± 2.1
7.5	1.2 ± 0.1	1.7 ± 0.2	1.6 ± 0.1	2.4 ± 0.3	4191.6 ± 83.4	3846.9 ± 99.9	21.0 ± 2.3	13.3 ± 1.9
10	0.9 ± 0.1	1.6 ± 0.3	1.3 ± 0.1	2.1 ± 0.4	4436.0 ± 111.9	3940.9 ± 167.9	28.6 ± 3.9	15.3 ± 3.7

Figure 4.20, **Figure 4.21** and **Figure 4.22** compare the morphology of GF (uncoated, GO and rGO respectively) obtained after conducting a tensile test on few GF reinforced epoxy composite. The samples were prepared by taking few uncoated, GO and rGO coated fibers and immersing them in epoxy resin and curing them according to the curing cycle used in this work. The samples (dimensions ca. 70 × 5 × 2) were subjected to tensile test at 10mm/min of cross-head speed in which the sample had failed with the fibers protruded from the matrix. The samples were observed under FESEM to conduct fractography on the GF surface.

In case of uncoated GF (**Figure 4.20**), the fibers show complete wetting of epoxy matrix with some areas containing bits of epoxy attached. This behavior is typical of GF having surface sized by a silane coupling agent to promote better adhesion with epoxy matrix. Visualizing the fiber surfaces that were coated with GO and rGO (**Figure 4.21** and **Figure 4.22** respectively) reveal not only the same wetting behavior of epoxy over the entire fiber surface but also some remnants of the nanosheets coatings attached to the fiber. This indicates three possible failure modes which could occur either at epoxy/coating interface, coating/coating interface (between the layers of graphene nanosheets) or at coating/fiber interface. An overall evaluation, however, using SFFT had revealed an improvement in ISS values for composites containing GO and rGO coated fibers which indicates this mixed failure modes resulting in an enhanced interfacial adhesion.

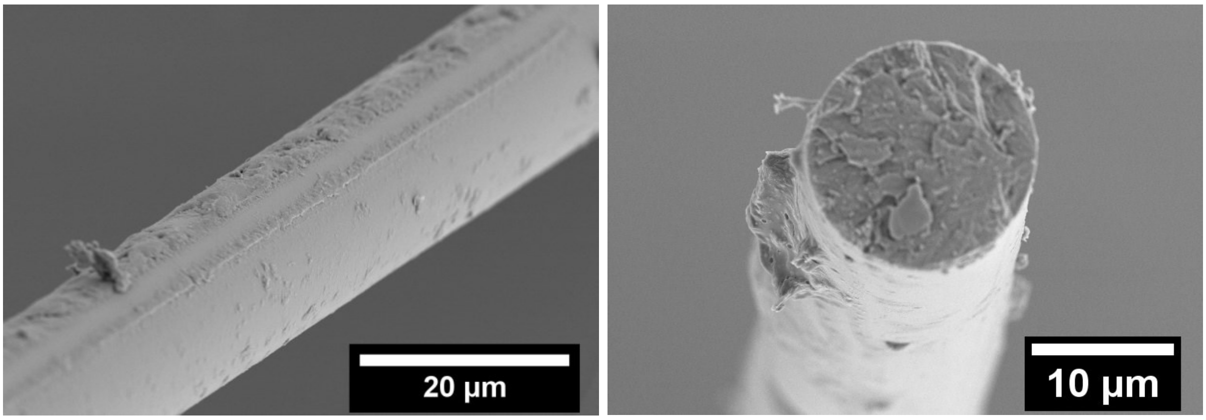

Figure 4.20. Fiber morphology of uncoated GF obtained by tensile test of few fiber reinforced epoxy composite.

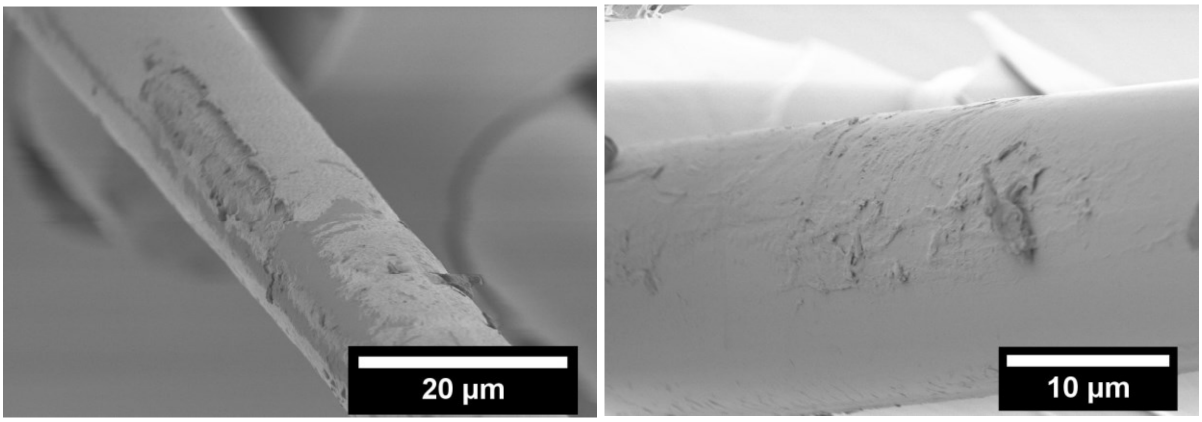

Figure 4.21. Fiber morphology of GO coated GF obtained by tensile test of few fiber reinforced epoxy composite.

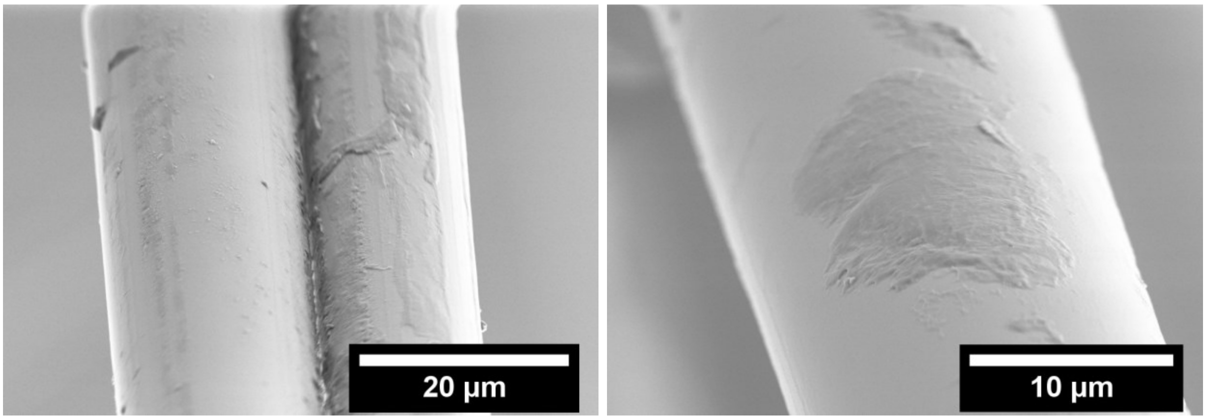

Figure 4.22. Fiber morphology of rGO coated GF obtained by tensile test of few fiber reinforced epoxy composite.

4.6 Macro-composite evaluation and testing

4.6.1 Macro-composite preparation

On the basis of the results obtained by SFFT on the microcomposites, it was decided to use 10V/cm as the electric field for the deposition of GO on the GF laminates during EPD process. To obtain rGO coated fibers laminates, GO coated GF laminates were subjected to the same reduction process as described in the section 3.1.3.3. These laminates were infused with epoxy resin during hand lay-up method as described in the section 3.3.2.

4.6.2 Fiber volume fraction

The fiber volume fraction of the composites was evaluated using the following formula:

$$V_f = \frac{1}{1+\frac{\rho_f}{\rho_m}\left(\frac{1}{W_f}-1\right)} \tag{4.1}$$

where V_f is the fiber volume fraction, ρ_f and ρ_m are the densities of the fiber and matrix while W_f is the fiber weight fraction of the composite. The fiber volume fraction in the composites was evaluated to be around 50% ± 10. The reason for the deviation from the mean was due to the creation of fiber laminate which was done manually using the GF yarns. Moreover, considering voids and resin rich areas in the composite, the deviation is quite obvious.

4.6.3 Deposition weight calculation

For quantitative analysis of epoxy/glass composites with GO and rGO interphase, the fibers before and after deposition were weighed. 4 fiber laminates as large as 100 mm × 100 mm were weighed and deposition of GO was then carried out as described in this work previously. After drying of the fibers under vacuum at 50°C, the fibers were again weighed to find the difference of the weight due to deposition. Eventually, epoxy resin was infused and cured. The final weight of the composite was measured and by taking the ratio of deposition and composite weight, the GO deposition weight content in Ep-GO-GF composites was calculated to be around 0.31% ± 0.03.

For rGO deposition content in the composite, the GO coated fibers were weighed and subjected to reduction process (**3.1.3.3**). rGO weight was evaluated in terms of percentage decrease in weight from GO due to reduction which was 0.11%, hence the final weight content of rGO in Ep-rGO-GF was practically the same.

4.6.4 Thermal stability

Figure 4.23 shows the TGA curves of the composites containing uncoated, GO and rGO coated fibers and resultant summary of the analysis is given in **Table 4-7**. The thermal stability of epoxy/glass fiber composites increases for both GO and rGO coated glass fibers where rGO interphase impart a better thermal stability (onset temperature for thermal degradation of 354.4°C) as compared to composites containing GO interphase (340.3°C). In case of composites containing GO coated fibers, the relatively lower thermal stability could be attributed to the decomposition of the oxygen functional moieties such as epoxy and hydroxyl which takes place around 250°C [188]. However, composites containing rGO coated fibers offer better thermal stability than others due to difficult path effect of graphene nanosheets (non-oxidized) which delays the escape of volatile degradation products favor char formation [188]. Similar trend was also observed in residual mass of the composites at 700°C after the test which supports the above results.

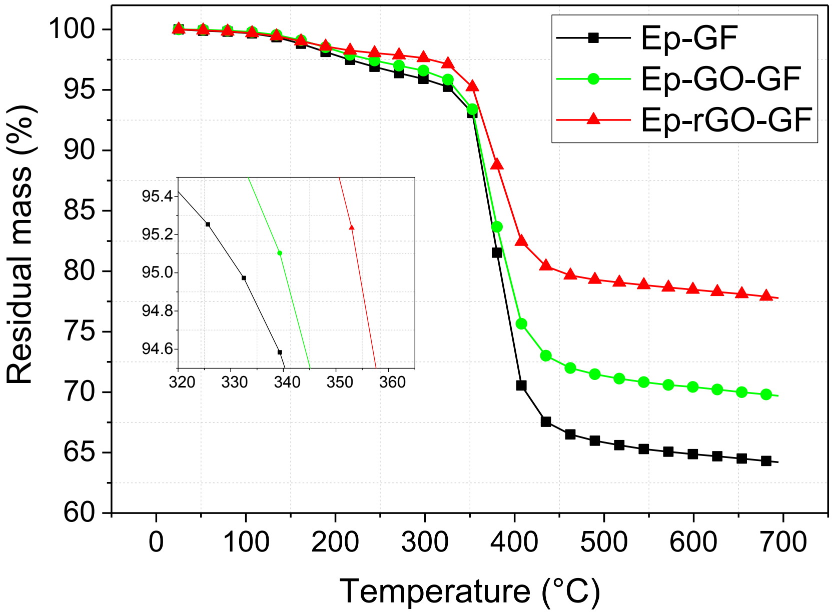

a)

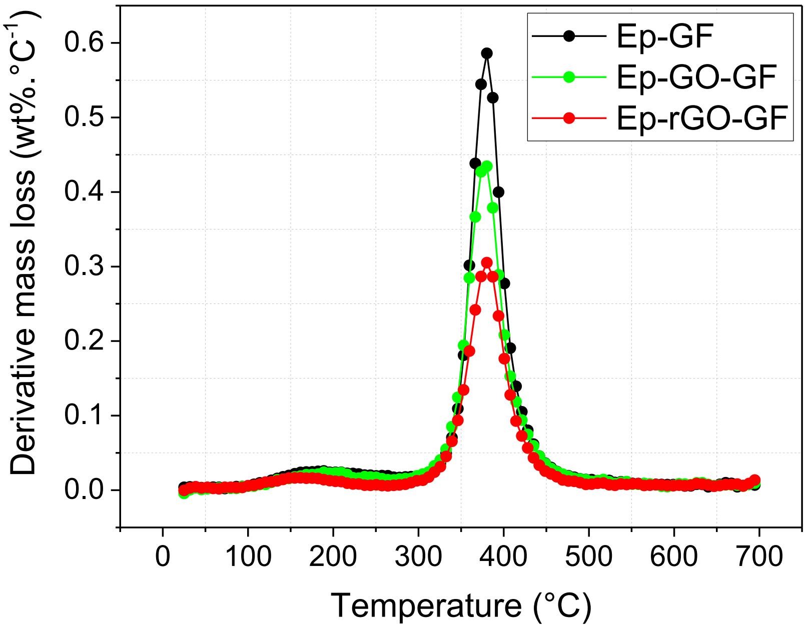

b)

Figure 4.23. TGA thermograms of uncoated and graphene coated fiber reinforced composites. (a)Residual mass as a function of temperature, (b) derivative of the mass loss.

Table 4-7. Results of TGA on composites with uncoated and coated fibers.

	Ep-GF	**Ep-GO-GF**	**Ep-rGO-GF**
Onset temperature (°C)	331.8	340.3	354.4
Residual mass at 700°C (%)	64.2	71.6	77.8
Peak. temperature (°C)	380.3	380.3	380.3

4.6.5 Microstructure evaluation

The cross-sectional views of the composites observed through OM and FESEM are shown in **Figure 4.24**. The images reveal a highly compact fiber arrangement embedded in epoxy matrix. Measuring the respective areas in the **Figure 4.24** for Ep-GF, Ep-GO-GF, Ep-rGO-GF yielded the fiber content percentage of 67%, 61% and 71% respectively.

4.6.6 Flexural properties

Figure **4.25a** and **b** reveal the typical load-displacement curves and respective flexural stress-strain curves are respectively reported. It is interesting to observe that the inclusion of the graphene interphase (GO and rGO) reinforced the composites: in fact they can sustain higher loads as compared to uncoated fiber based composite. **Figure 4.26** shows the resulting flexural modulus and flexural strength measured from the flexural tests of the composites. The flexural modulus increases by 19% and 9% for GO and rGO coated GF, respectively, as compared to neat composites. The increase of modulus is related to the results in previous experiment in which the ISS for composites containing GO interphase show improved bonding conditions and mechanical interlocking phenomena. The flexural strength of the composites containing GO showed an increase by 20%, again due to the better interfacial adhesion proven earlier but in case of rGO, the value is practically the same as compared to uncoated fiber based composites. This could be attributed to the weak interfacial adhesion between rGO and epoxy matrix thus slightly reducing the strength values in flexural mode.

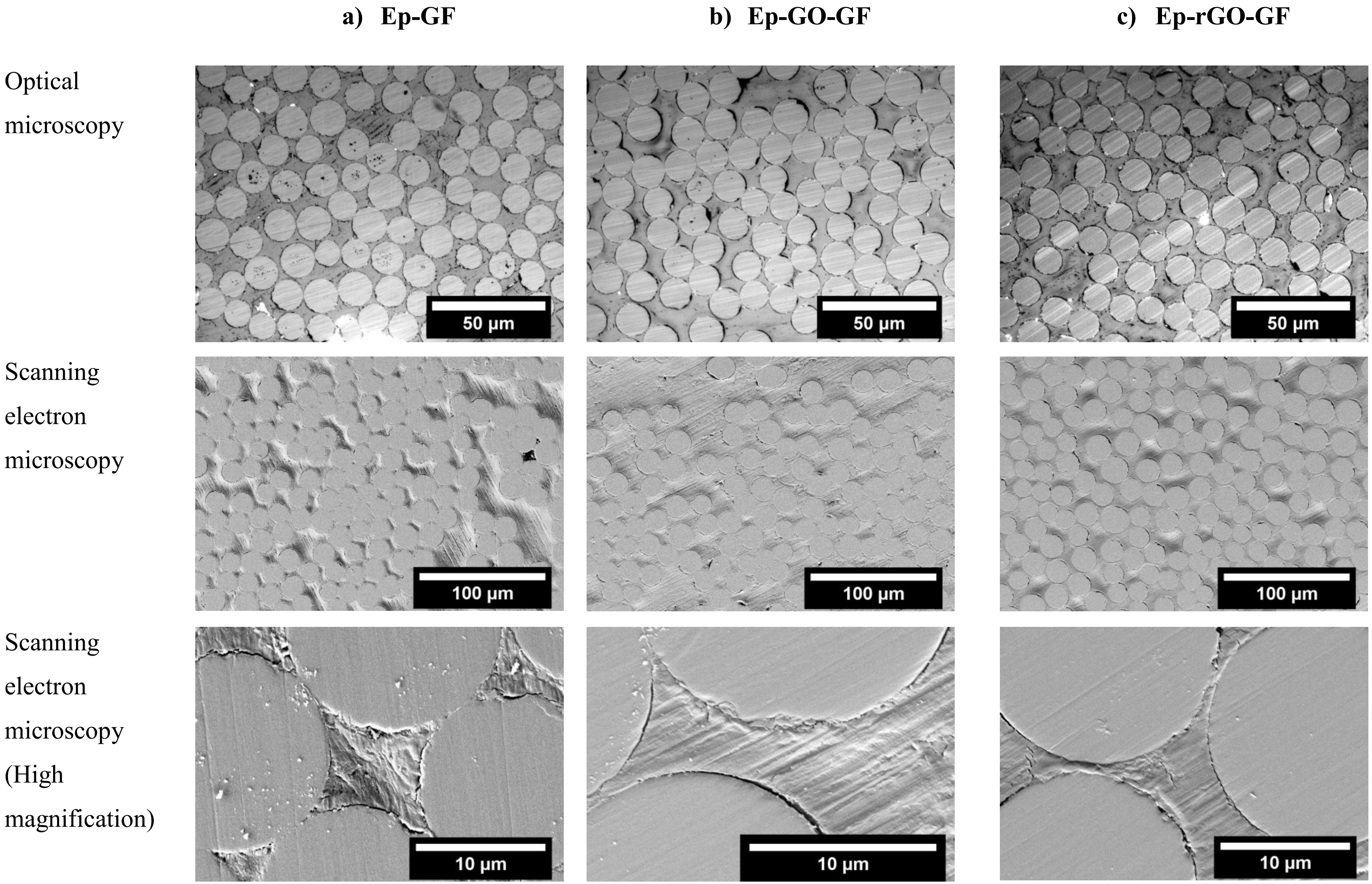

Figure 4.24. Composite cross-section visualization through optical and field emission scanning electron microscopy at different magnifications.

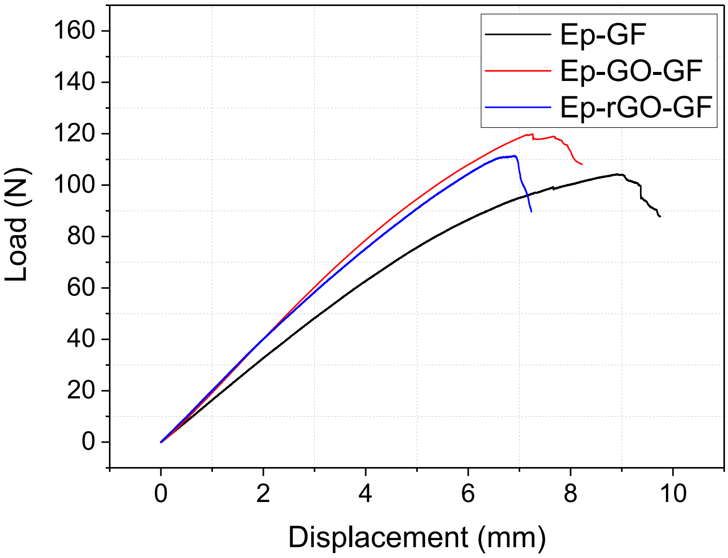

a)

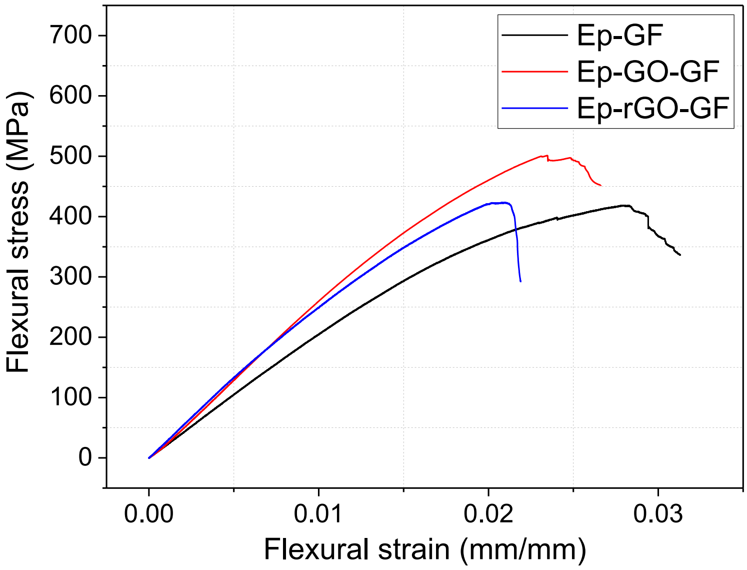

b)

Figure 4.25. Flexural tests data of composites where a) representative load-displacement curves and b) corresponding stress- strain curves.

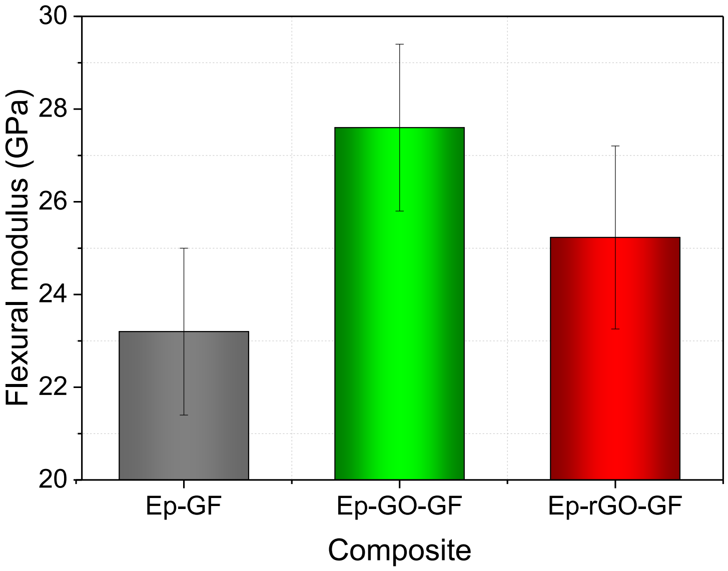

a)

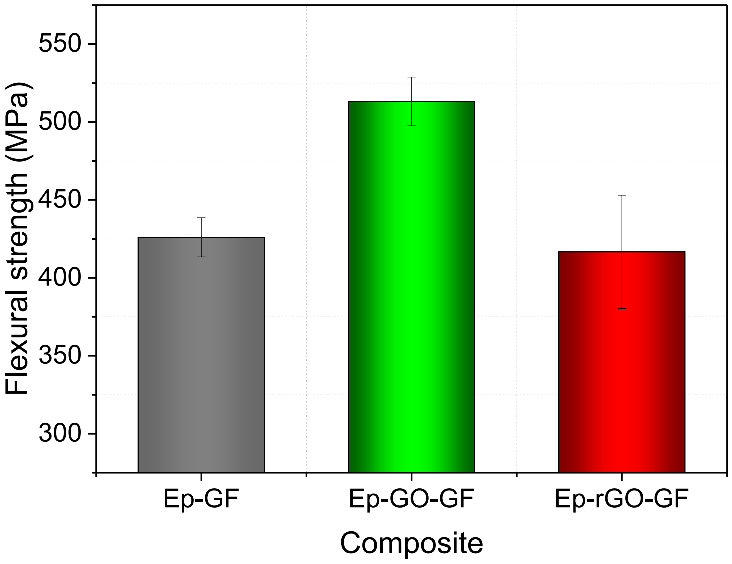

b)

Figure 4.26. a) Flexural modulus and b) flexural strength as determined by 3 point bending tests.

4.6.7 Interlaminar properties

4.6.7.1 Short beam shear strength

To investigate the transverse reinforcement of graphene coated fibers in epoxy based composite, interlaminar shear strength was investigated by short beam shear strength test. The test was performed on the three different composites (with uncoated, GO and rGO coated fibers). It was observed that the glass/epoxy composites having GO interphase presented a 15% increase in the ILSS as compared to uncoated fibers while a 9% increase was found for rGO based glass/epoxy composites (**Figure 4.27**). This result also conforms to our previous results that GO coated fibers offer dual reinforcing phenomena i.e. oxygen-based functional groups and mechanical interlocking together bridging the epoxy and glass fibers in the composite. This "cross-linking" via the interface caused an increased interfacial strength, which could be interpreted as an evidence for the enhanced ILSS. In case of rGO based glass/epoxy composites, the only reinforcing condition i.e. the mechanical interlocking was also responsible for increasing the ILSS but was not as high as for GO due to the lower amount of oxygen-based functional groups on the surface of rGO which expresses itself in the less effective influence on the ILSS. The images of the composite specimens failed during SBS test are shown in **Figure 4.28** where the interlaminar failure can be visualized. It is interesting to observe that the composite containing rGO (**Figure 4.28c**) showed many cracks between the laminas thus verifying the poor interlaminar adhesion due to rGO interphase.

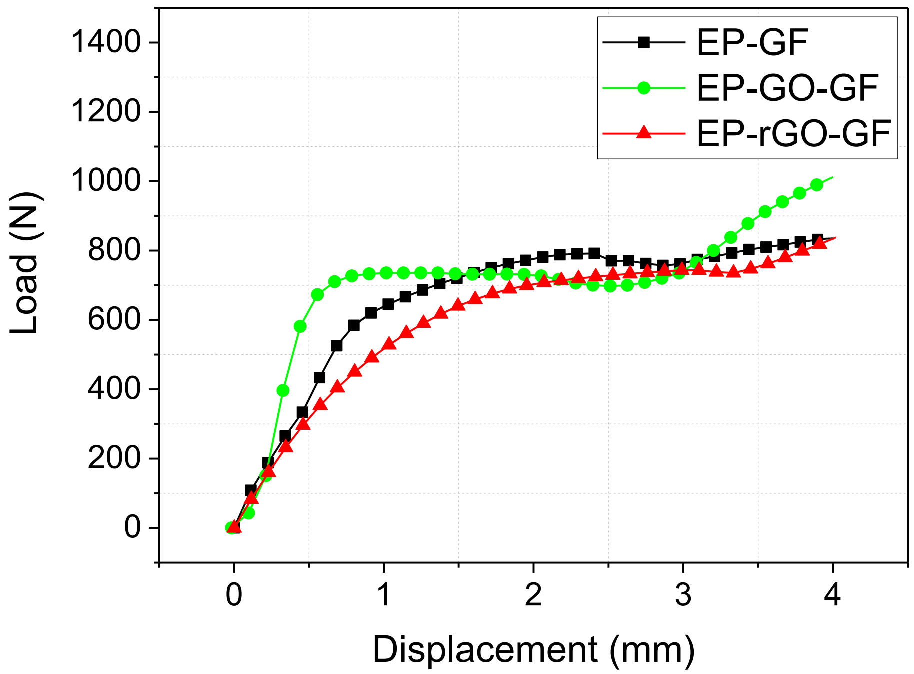

a)

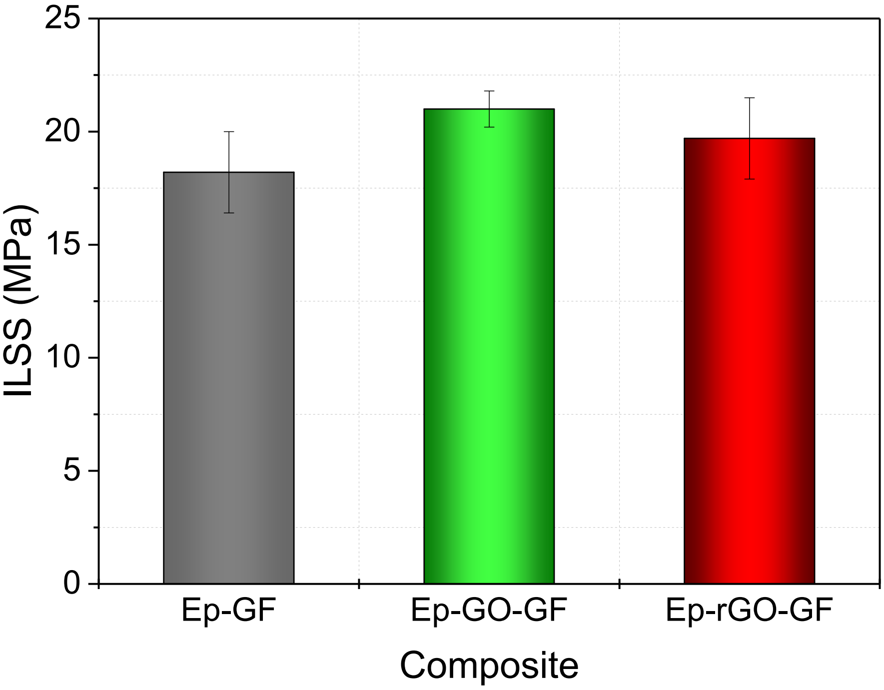

b)

Figure 4.27. Interlaminar shear strength as determined by short beam strength test.

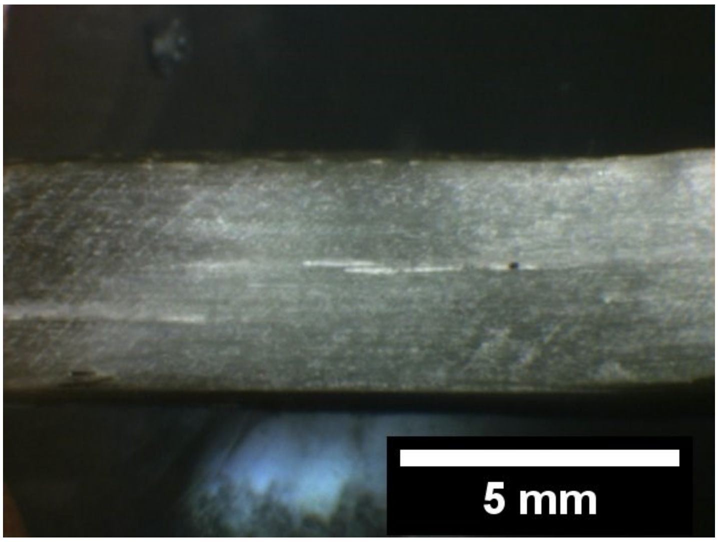

a)

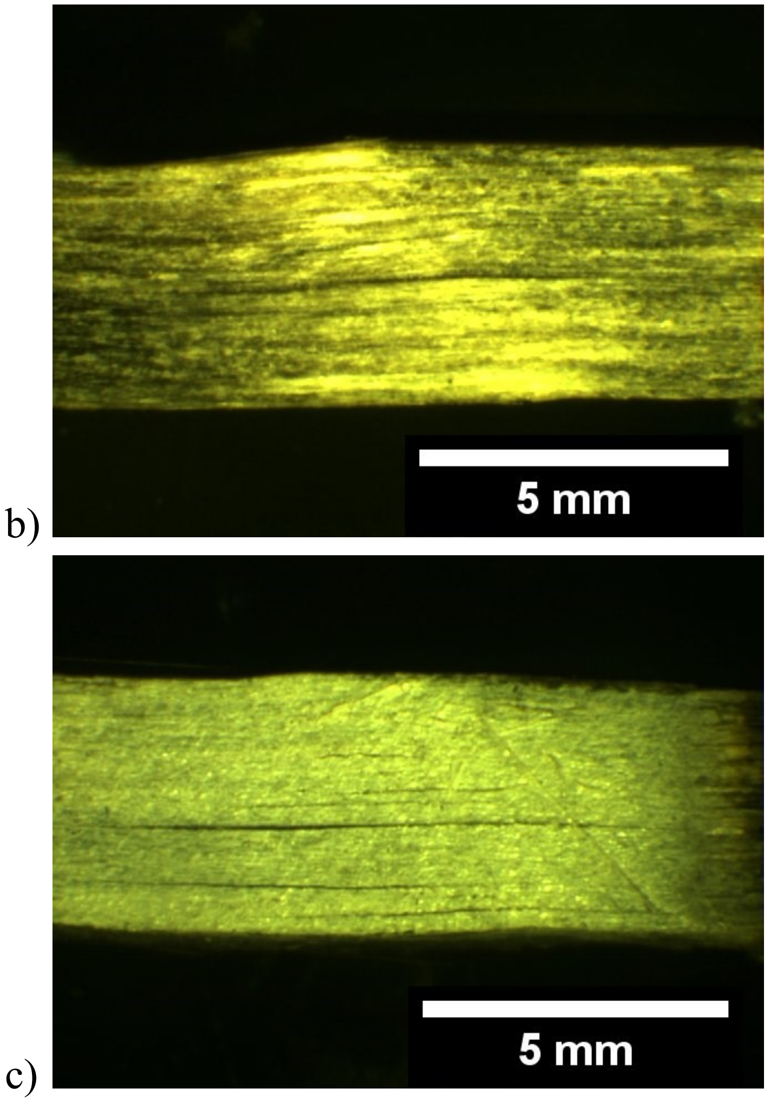

Figure 4.28. Optical microscopy images of composite specimens (side view) after being subjected to SBS test where a) Ep-GF, b) Ep-GO-GF and c) Ep-rGO-GF.

4.6.7.2 Mode I Interlaminar Fracture Toughness (DCB)

The G_I value was measured by considering the specimen width, the length of crack propagation and the strain energy loss as given in Equation 2.7. The strain energies for each composite were evaluated from their load-displacement plot (**Figure 4.29**) and were plotted as resistance curves (R-curves) as shown in **Figure 4.30**. **Table 4-8** shows the average G_{Ic} values of the three composites tested.

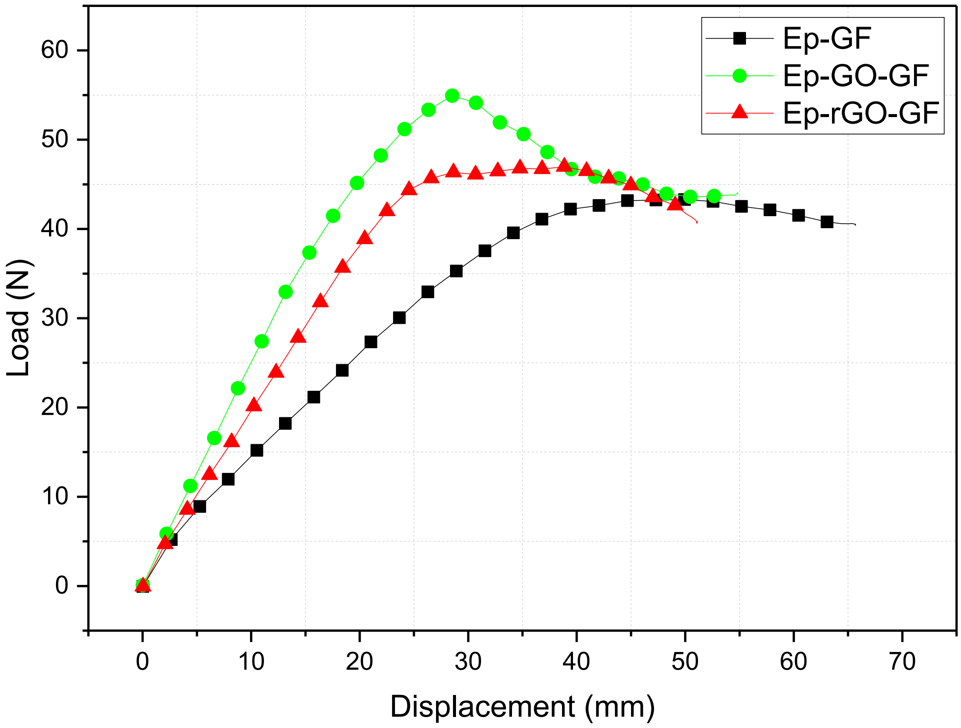

Figure 4.29. Typical load-displacement curves obtained during Mode I fracture toughness tests of multiscale composites.

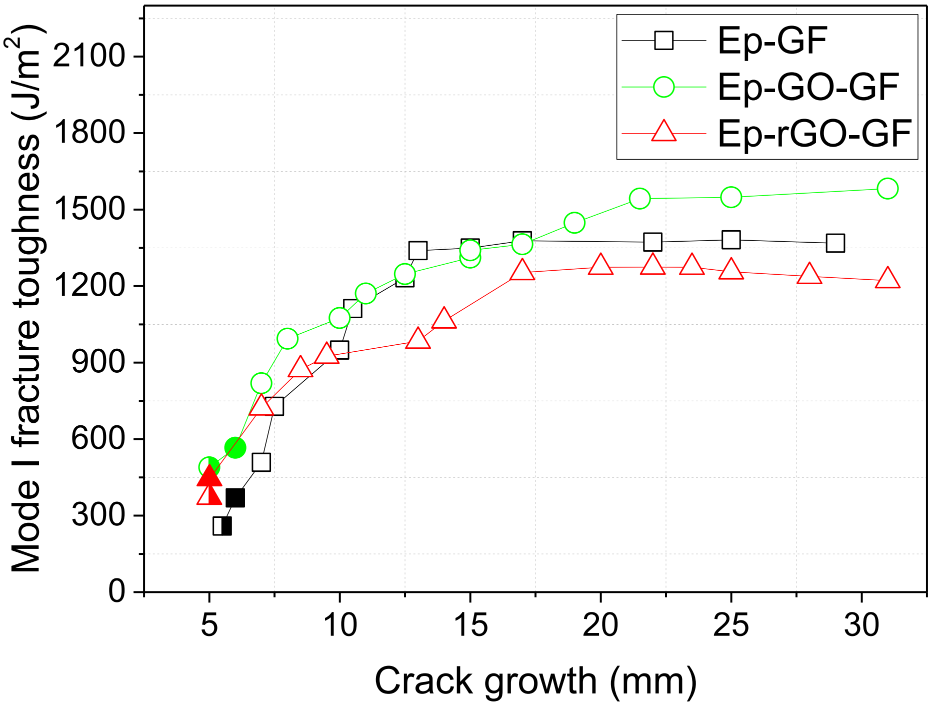

Figure 4.30. Delamination resistance curves (R-curves) from DCB test; where half-filled symbols representing NL (Non linearity) and completely filled symbols representing VIS (visual observation).

Table 4-8. Mode I fracture toughness (G_{Ic}) values of Ep-GF, Ep-GO-GF and Ep-rGO-GF composites.

Specimen	**Nonlinearity (NL)**	**Visual observation (VIS)**	**Maximum load (MAX)**
	(J/m²)	*(J/m²)*	*(J/m²)*
Ep-GF	243.5 ± 21.5	401.8 ± 46.3	1176.4 ± 244.9
Ep-GO-GF	384.3 ± 92.6	692.9 ± 145.1	1275.8 ± 180.5
Ep-rGO-GF	352.8 ± 27.0	407.9 ± 52.8	1153.2 ± 141.7

An explanation of the G_{Ic} values obtained can be best explained by doing a comparison with the ILSS values (as obtained in the SBS test). As it can be seen in **Figure 4.31**, composites reinforced with GO coated GF showed the highest values for the NL and VIS G_{Ic} values as compared to uncoated GF and rGO coated GF. The G_{Ic} value of MAX was however practically the same for the composites. rGO coated GF fibers also provided some resistance to crack propagation but not as compared to GO which is pretty consistent to the result of ILSS values. This investigation clearly shows the higher energy required for crack propagation when graphene was deposited on GF as a continuous reinforcing interphase in epoxy/glass composites.

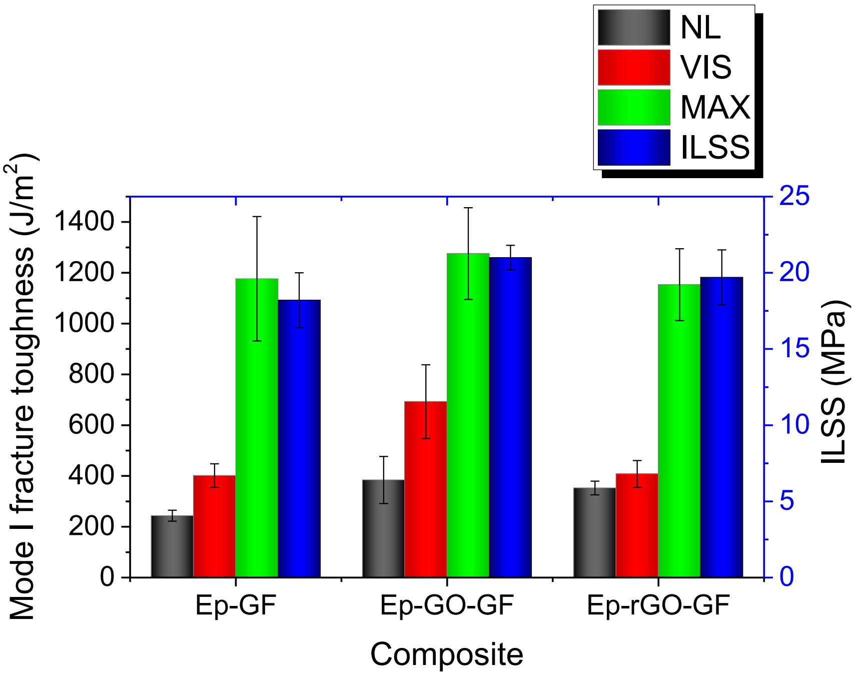

Figure 4.31. Comparison of mode I fracture toughness values with short beam strength values (NL: non-linear, VIS: visual observation, MAX: maximum load, ILSS: interlaminar shear strength.

The analysis of the fracture surfaces obtained during mode I fracture toughness test reveal interesting observations. Considering the fracture surfaces of Ep-GF composite (**Figure 4.32**), the interfacial areas between the epoxy and GF reveals a weak interaction between them. Observing the GF surfaces give us two different surface morphology, the one with clean surface means a clean debonding between the epoxy and GF while the other with slightly rough surfaces suggesting strong interfacial bonding between GF and epoxy and failure occurring in the epoxy matrix hence leaving the GF covered with remnant epoxy matrix. This could be safely attributed to the epoxy compatible sizing on GF.

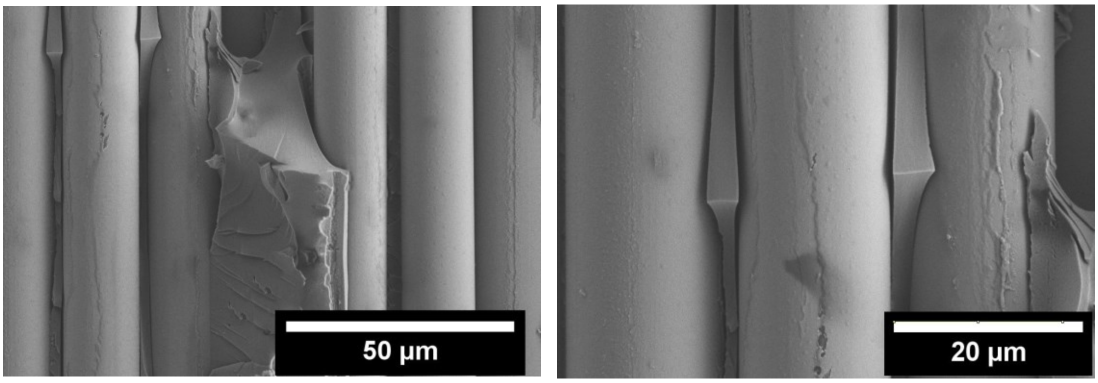

Figure 4.32. Fracture surfaces of Ep-GF composites obtained during Mode I fracture toughness test as observed by FESEM (crack propagation from top to bottom).

The fracture surfaces of Ep-GO-GF (**Figure 4.33**) shows a number of fibers coated with the remnant of epoxy matrix which could be associated with the epoxy/GO interfacial adhesion. Scan in other portions of the specimen revealed fiber coating with GO as well where the failure could be due to the debonding at the epoxy/GO interface. In addition, clear fracture surfaces could suggest that the debonding at GO/GF which has the highest interfacial adhesion as investigated in the FFM analysis (section 3.4.3.3). It can be visualized from the FESEM images that the fibers are bonded together with continuous epoxy resin hence suggesting the influence of GO coating on fibers promoting strong inter-fiber interactions due to epoxy/GO/GF system. A combination of all these failure modes thus increased the fracture toughness of the epoxy/glass composites containing GO interphase.

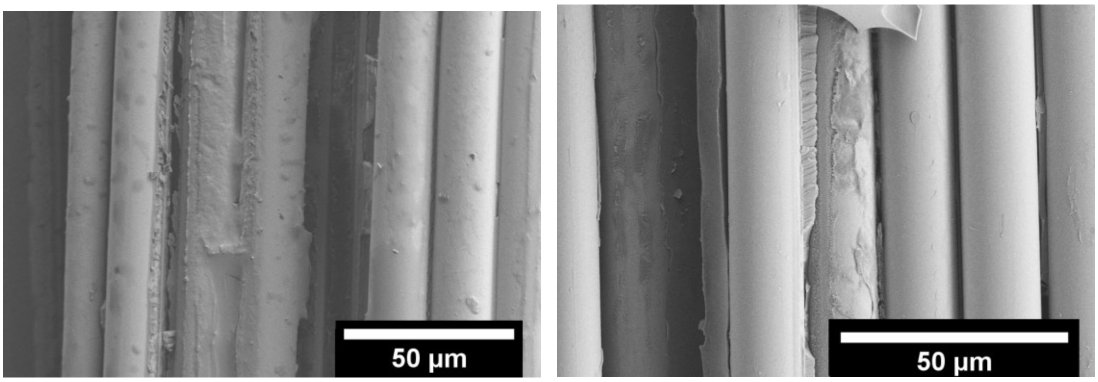

Figure 4.33. Fracture surfaces of Ep-GO-GF composites obtained during Mode I fracture toughness test as observed by FESEM (crack propagation from top to bottom).

The fracture surfaces obtained from the Ep-rGO-GF composite system gives us a different picture in which the fiber surfaces are covered totally with a continuous coating (**Figure 4.34**). A closer examination reveals it was the rGO coating which had a different morphology as compared to the epoxy matrix. The lower values of NL during mode I fracture toughness is a clear evidence that the debonding took place at the epoxy/rGO interface which is correlated to the reasoning found in this work that rGO sheets, due to unavailability of the oxygen based functional groups, offered weak interfacial adhesion towards the epoxy matrix.

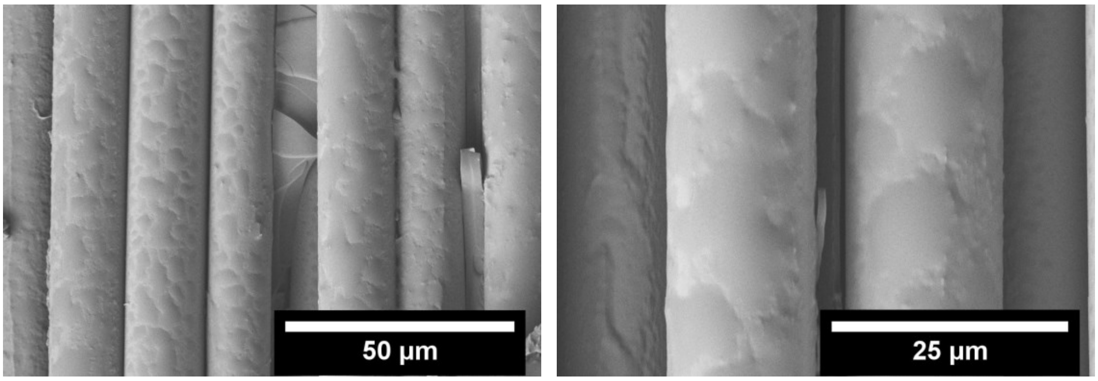

Figure 4.34. Fracture surfaces of Ep-rGO-GF composites obtained during Mode I fracture toughness test as observed by FESEM (crack propagation from top to bottom).

4.6.8 Dynamic mechanical thermal analysis (DMA)

A comparison of viscoelastic properties of the fabricated composites with uncoated GF and coated (GO and rGO) GF was performed using dynamic mechanical thermal analysis technique in dual-cantilever mode. The analysis was carried out between a temperature ranges of 0 to 150°C under a constant load of 5 MPa. For all composites specimens, the plots of storage modulus (E'), loss modulus (E") and tan delta (δ) are compared in **Figure 4.35** and **Figure 4.36**.

As compared to base composite (Ep-GF), the moduli increased in case of composites containing GO interphase however for rGO interphase, a decrease was observed which is consistent to the flexural properties obtained as discussed in section **4.6.6**. The increase in tan delta value for composites with GO coated fibers also show an increment which confirms the enhanced interfacial adhesion due to positive contribution of GO interphase between GF and epoxy. Similarly the decrease of the same in case of rGO interphase follows the similar behaviour offered by the weak interfacial interaction between rGO and epoxy.

A different behaviour is observed in case of the T_g of the composites evaluated by measuring the temperature corresponding to the E" peaks which shows that the rGO interphase increased the T_g by 7% due to better thermal stability of the composites. **Table 4-9** summarizes the values of viscoelastic properties obtained in this anaylsis.

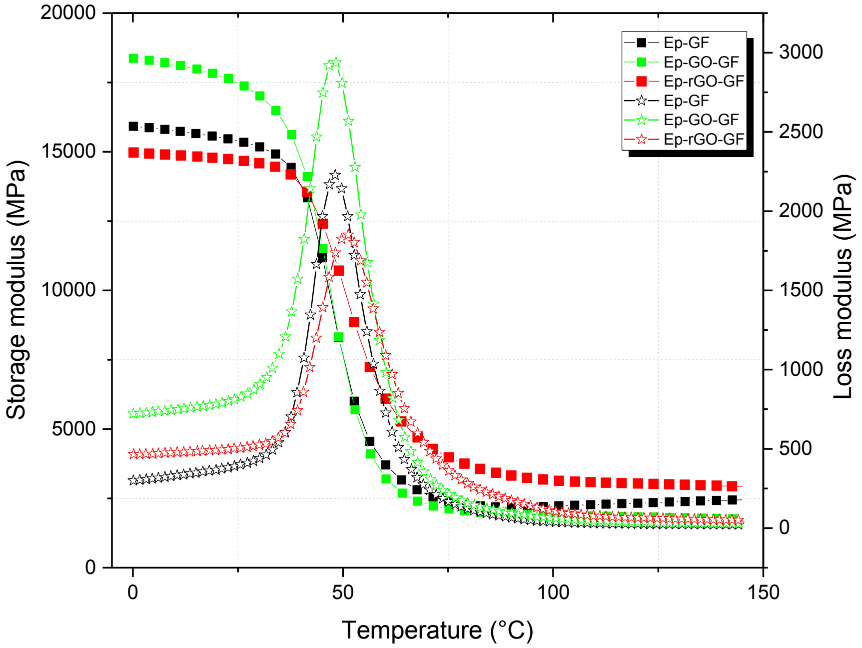

Figure 4.35. Storage modulus (square) and loss modulus (stars) plots obtained by dynamic mechanical analysis (DMA) in dual-cantilever mode of composites containing uncoated and coated (GO and rGO) GF.

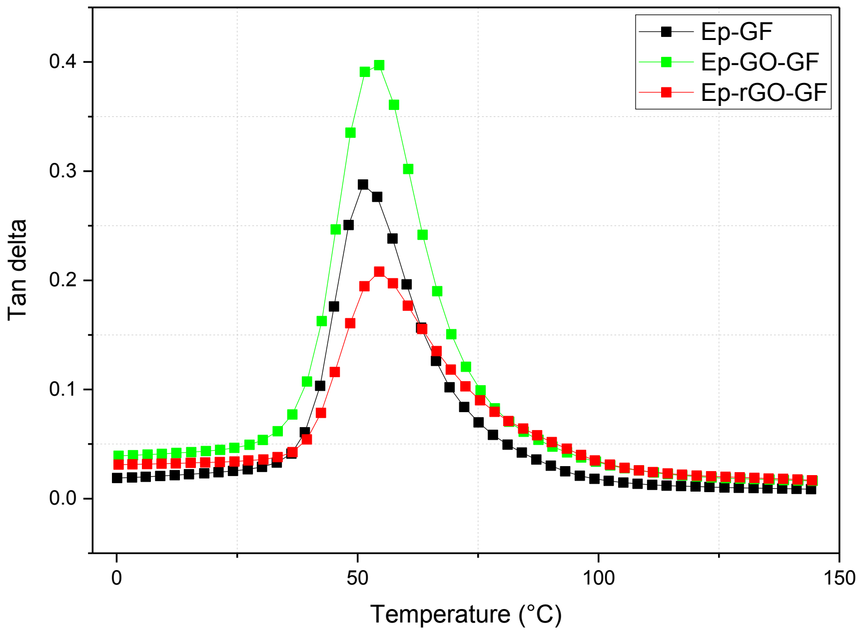

Figure 4.36. Tan delta plot obtained by dynamic mechanical analysis (DMA) in dual-cantilever mode of composites containing uncoated and coated (GO and rGO) GF

Table 4-9. Results of DMTA test on composites containing uncoated and coated (GO and rGO) GF.

Dynamic mechanical property	**Ep-GF**	**Ep-GO-GF**	**Ep-rGO-GF**
Storage modulus E’ (0°C) (MPa)	15915.0	18370.1	14970.3
Storage modulus E’ (23°C) (MPa)	15450.0	17607.4	14727.5
Loss modulus E” (23°C) (MPa)	385.6	802.6	499.4
Tan delta peak value	0.29	0.39	0.20
T_g at loss modulus peak (°C)	48.1	47.6	51.0

4.6.9 Creep behavior

Isothermal creep compliance curves of the composites Ep/GF, Ep/GO/GF and Ep/rGO/GF at a reference temperature of 30°C and applied stress of 5 MPa are shown in **Figure 4.37** while the values of the instantaneous creep compliance (D_e), of the viscoelastic component after 2000s (D_{ve2000}) and of the total creep compliance after 2000s (D_{t2000}) are reported in the **Table 4-10**. A significant reduction of the creep compliance can be noticed for coated fiber reinforced composites as compared to reference composite (with uncoated fibers). This improvement in the creep stability was based on a remarkable reduction of both the elastic and the viscoelastic components of the total creep compliance. This behavior is in agreement with the behavior observed under flexural conditions of the composites.

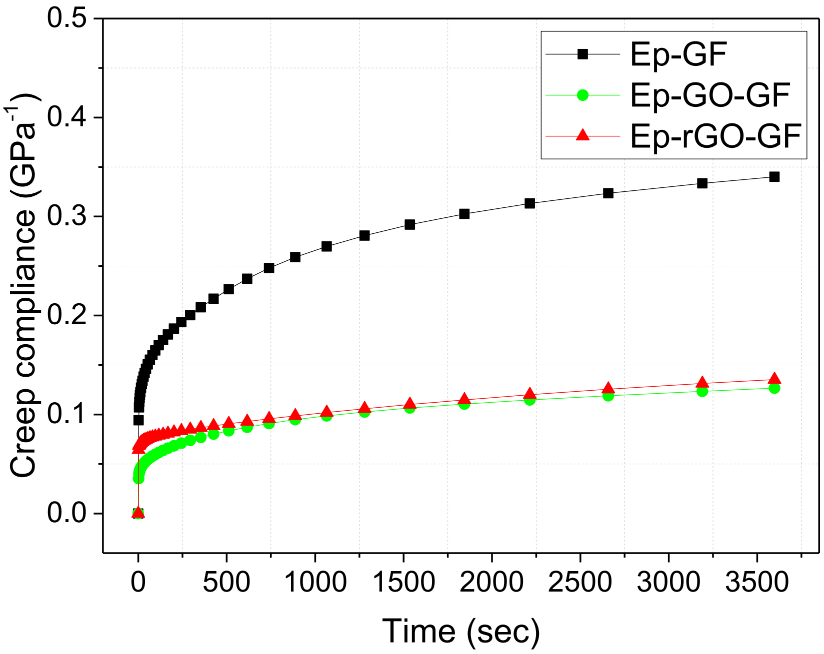

Figure 4.37. Creep compliance curves of the composites Ep-GF, Ep-GO-GF and Ep-rGO-GF (T = 30°C, σ = 5 MPa).

Table 4-10. Creep compliance components of the composites Ep-GF, Ep-GO-GF and Ep-rGO-GF (T = 30°C, σ = 5 MPa).

	D_e (GPa^{-1})	D_{ve2000} (GPa^{-1})	D_{t2000} (GPa^{-1})
Ep-GF	0.094	0.213	0.307
Ep-GO-GF	0.035	0.077	0.112
Ep-rGO-GF	0.064	0.053	0.117

The creep compliance curves of the composites Ep-GF, Ep-GO-GF and Ep-rGO-GF have been tentatively fitted with the Findley equation (Equation 3.3), and the results are shown in **Figure 4.38**. The parameters obtained from the best fitting of experimental creep data are summarized in **Table 4-11**, along with R^2 values. It can be noticed that the Findley model successfully fits all the creep curves, with R^2 values of around 0.99 for all the cases. It is interesting to observe that, as compared to neat composites, the reduction of the creep compliance due to the presence of the GO coating in Ep-GO-GF composites results in the substantial reduction of the instantaneous creep compliance term D_e and of the coefficient k, related to the strain retardation process of the macromolecules. Moreover the parameter n was not changed by the GO coating of the GF as compared to the uncoated GF based epoxy composite. For Ep-rGO-GF, however, there was a slight increase of the D_e as compared to the neat composite and at the same time the coefficient k drops very significantly which shows that the retardation of creep process increases tremendously afterwards.

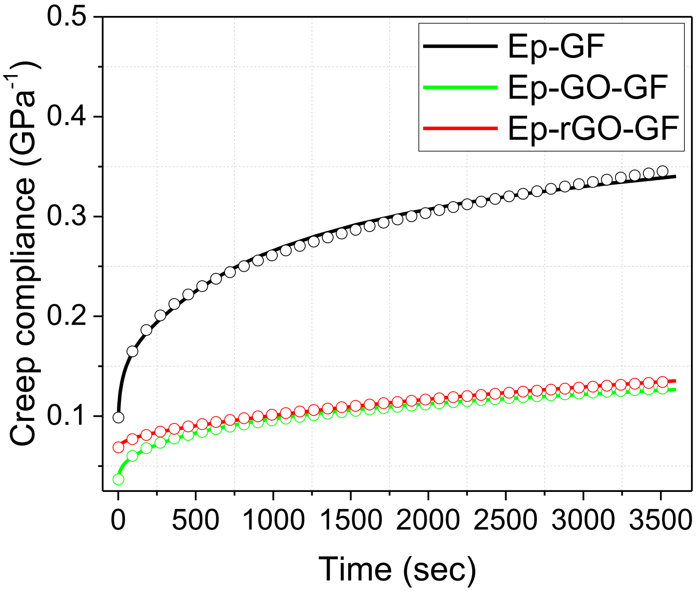

Figure 4.38. Experimental creep compliance curves (solid line) of the composites and theoretical prediction (open circles) according to the Findley model (T = 30°C, $\sigma = 5$ MPa).

Table 4-11. Fitting parameters of the creep compliance of different composites.

	D_e (GPa^{-1})	**k (GPa^{-1} s^{-n})**	**n**	**R^2**
Ep-GF	0.064	0.028	0.3	0.99832
Ep-GO-GF	0.025	0.009	0.3	0.99882
Ep-rGO-GF	0.067	0.0008	0.5	0.99745

4.7 Functional properties

4.7.1 Electrical resistivity

All composites (Ep-GF, Ep-GO-GF and Ep-rGO-GF) were subjected to electrical resistivity measurement. As a base test, the uncoated fiber composite showed a higher resistivity (around 10^{14} Ω.cm) which was due to the insulating nature of both the epoxy matrix and glass fibers. The presence of GO interphase in Ep-GO-GF also did not improve the conductivity behavior (around 10^{13} Ω.cm) which was in accordance to the fact that GO nanosheets are insulating in nature due to the presence of substantial electronic disorder arising from variable sp^2 and sp^3 bonds (**Figure 4.39**) [189]. However in case of Ep-rGO-GF composites, the presence of a conductive rGO coating on GF gave the entire system a conductive nature ($<10^2$ Ω.cm). This analysis confirms the successful reduction of GO to rGO [190].

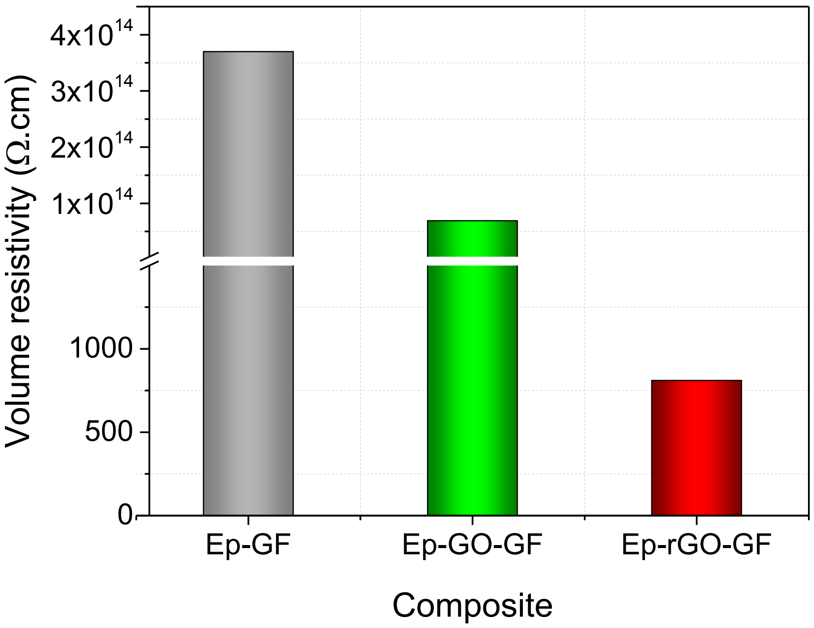

Figure 4.39. Volume resistivity of Ep-GF, Ep-GO-GF and Ep-rGO-GF composites [190].

In order to investigate the effect of having a continuous interphase oriented along the fibers direction, the electrical conductivity of the composites was tested along three mutually orthogonal directions i.e. x-axis, y-axis and z-axis as clarified in the **Figure 4.40**. The x-axis being the direction along which the fibers were aligned and therefore the conductive interphase was continuous while it is worthwhile to mention that in y and z-axes, the continuous interphase was separated by insulating layers of epoxy matrix.

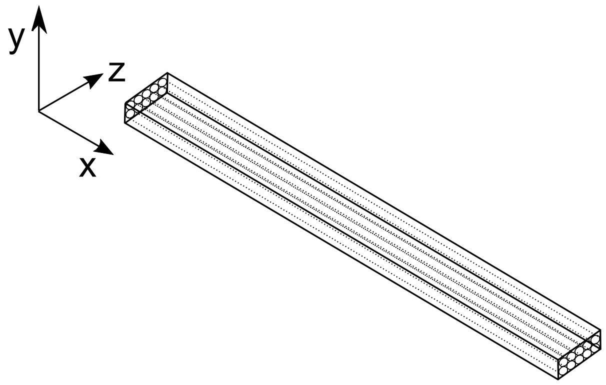

Figure 4.40. Description of directions in terms of orientation of electrical conductivity measurement.

In the **Figure 4.41**, the volume resistivity along the three directions of rGO coated composite are compared. The composites showed a very low resistivity along the x-axis which contains the continuous path for electrons to travel through the structure. On the other hand, the y-axis and z-axis showed a higher resistivity because of the alternating conductive (graphene) and non-conductive (epoxy) layers. Between these, y-axis had less resistivity as compared to z-axis as the load was applied on this direction during the composite manufacturing hence compressing the fibers and providing better tunneling effect or possibly direct contact between the fibers.

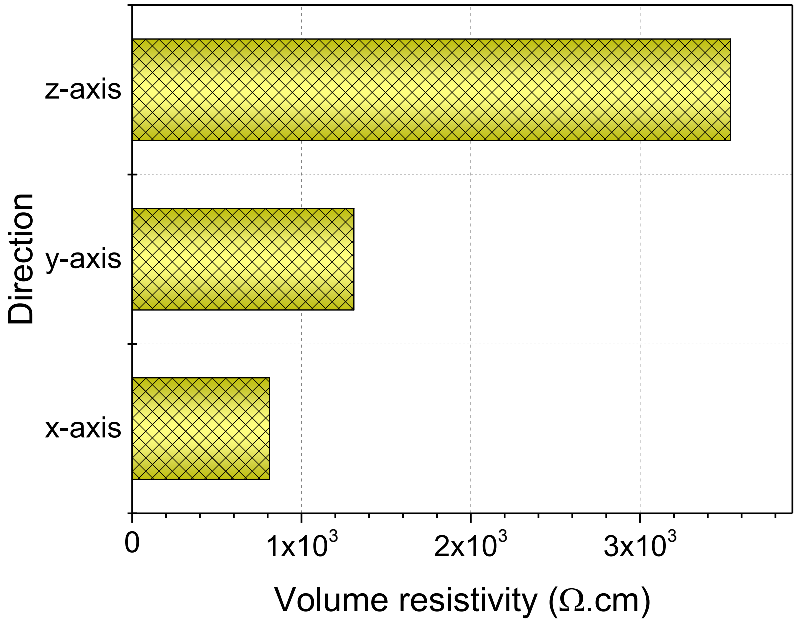

Figure 4.41. Volume resistivity of Ep-rGO-GF composites measured along three different directions of the sample with respect to fiber orientation.

4.7.2 Piezoresistivity

To investigate the effect of applied strain on the conductivity behavior, the composite specimens were tested in various mechanical loading modes and their absolute resistances were monitored simultaneously by two probe contact method.

In case of quasi-static tensile mode (**Figure 4.42**), it is interesting to note that the electrical resistance decreased within initial 0.1% strain, which could be due to the rearrangement of the coated fibers at the microscale that lead to better electrical coupling among each other thus the observed decrease in resistance. At higher levels of strain, the change in resistance increased progressively till it became steep after 0.2% tensile strain. Considering this, a gage factor (k) of about 11 was calculated by applying a tangent line in the elastic portion and using the formula $\left(k = \left(\Delta R / \mathrm{R}_0\right) / \varepsilon\right)$. Since the Poisson's ratio of the composite analyzed was 0.36 (as measured by a biaxial extensometer), the factor $(\Delta\rho / \rho)$ came out to be approximately 0.01 (equation 3.5).

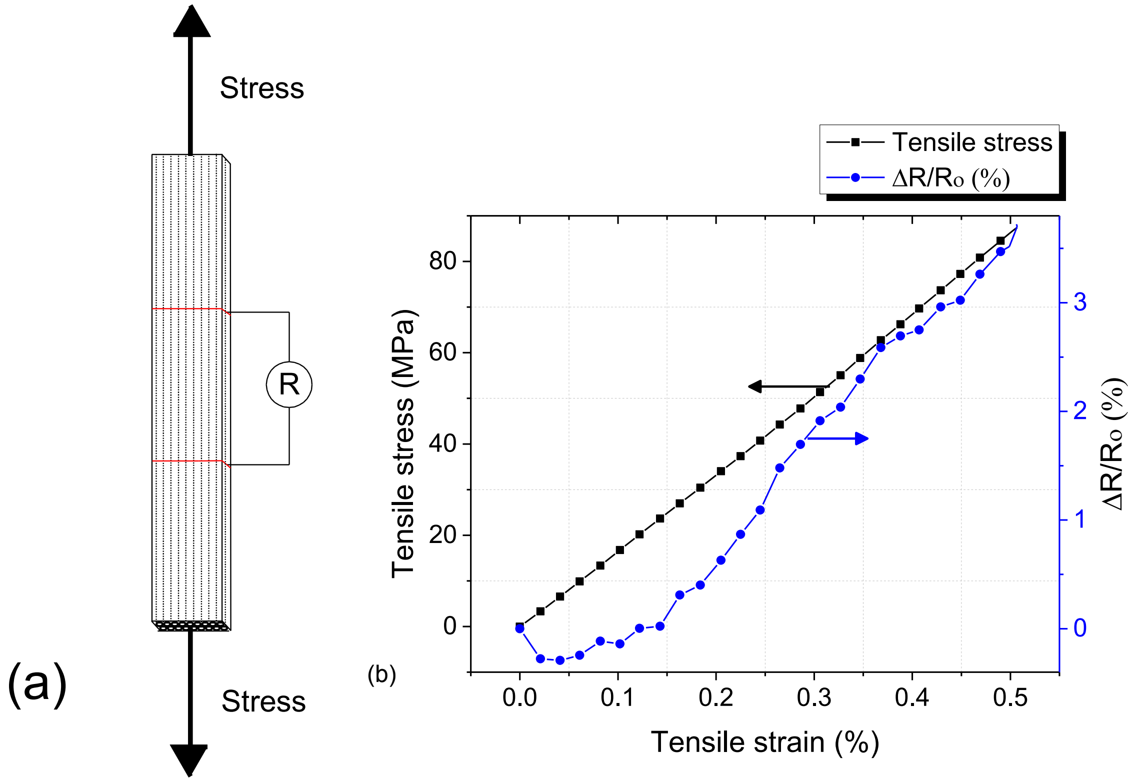

Figure 4.42. Piezoresistivity of GF/rGO/Ep composites under tensile loading condition [190].

Similar kind of behavior was also observed when flexural loading was applied as shown in **Figure 4.43**. A sample loaded under flexure experiences both tensile and compressive stresses below and above the neutral axis, respectively. In this regards both upper and lower surfaces were separately monitored on different test specimens.

Figure 4.43a shows the schematic diagram of the flexural test wherein the piezoresistivity was monitored on the bottom side of the specimen which experiences the tensile stresses. The **Figure 4.43b** demonstrates the piezoresistivity of the specimen's surface which experienced the compressive stress. The piezoresistivity on this surface could be visualized when considering the influence of stresses acting on the fibers. A steady resistance change can be observed till 2.5% of flexural strain, the resistance change was steady until the fibers started to break resulting in failing of the specimen which consequently had a dramatic effect on the relative change of resistance. Similar kind of behavior can be also observed from the analysis of the compressive stress zone of the specimen (**Figure 4.43c**, **Figure 4.43d**).

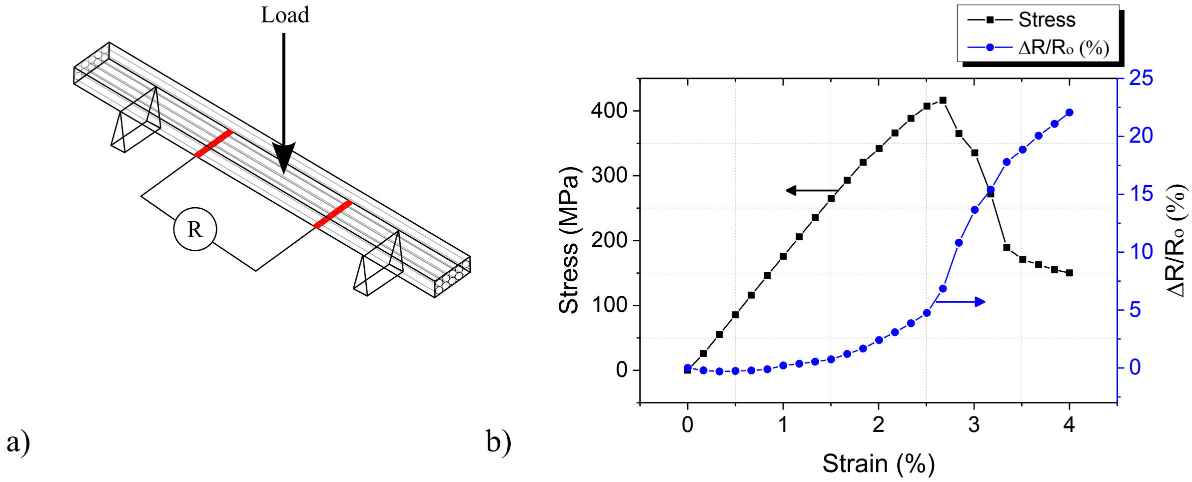

a)   b)

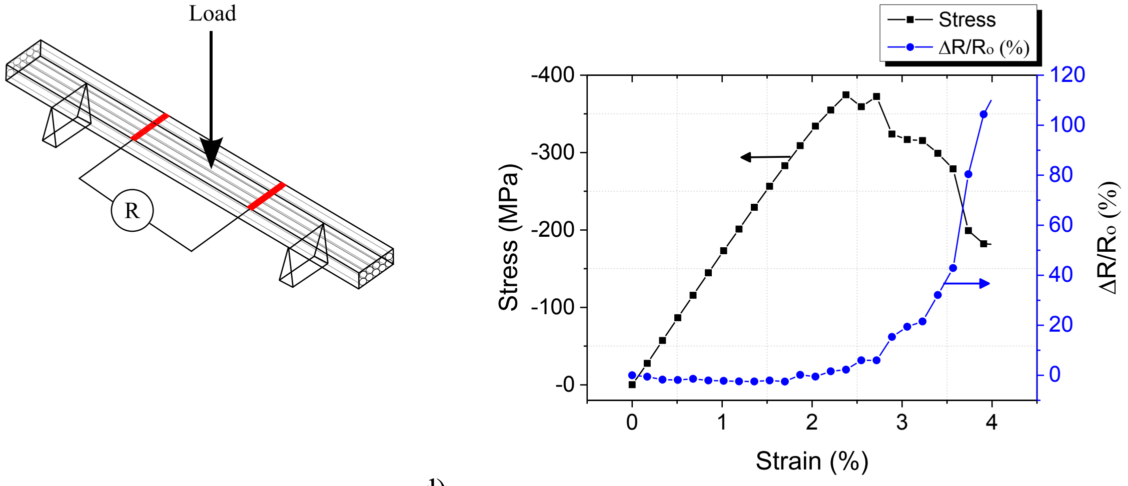

c) d)

Figure 4.43. a) Schematic diagram of piezoresistivity test conducted under flexural mode where change in resistance was monitored on the surfaces experiencing a) tensile and b) compressive stresses respectively.

A comparison of the relative resistance change experienced during the initial 2% elastic flexural strain in both cases (tensile and compressive) (**Figure 4.44**) reveal the piezoresistivity behavior of the composite specimens. The surface experiencing tensile stresses exhibit an increasing relative resistance change with respect to applied strain (after initial 0.5% strain) which could be attributed to the increase in length of the fibers hence the increase in the resistance can be seen. On the other hand, the compressive side experiences a decrease in relative resistance change until 1.5% after which a steep increase in relative resistance change can be observed, the decrease could be associated to compression of the fibers first afterwards which the fiber breaking take place thus contributing to the resistance increase.

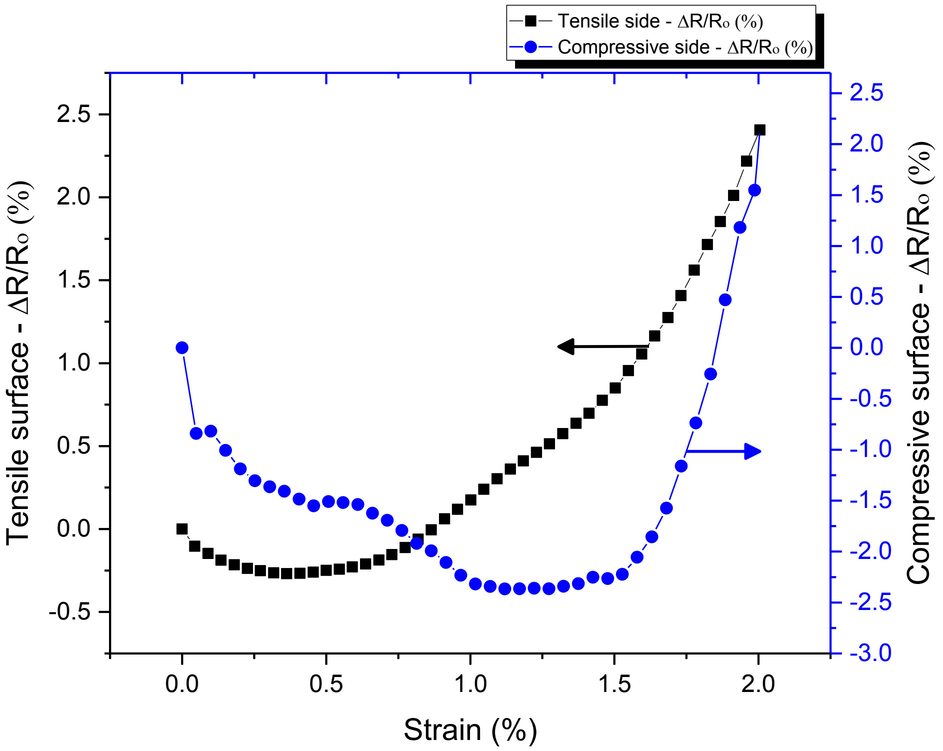

Figure 4.44. Comparison of piezoresistivity of Ep/rGO/GF composites observed during flexural loading between surfaces experiencing tensile stress (tensile surface) and compressive stress (compressive surface).

In another testing protocol, the reversibility of electrical network was tested by subjecting the hybrid composite specimen under repeated loading-unloading cycles in the strain range of 0.1% < ε < 0.5% and the electrical resistance was monitored during each loading and unloading part of the cycle. **Figure 4.45** show the results obtained under cyclic conditions in which the reversible piezoresistivity can be confirmed. The gage factor and the factor $(\Delta\rho / \rho)$ calculated here were about 3.8 and 0.006, respectively.

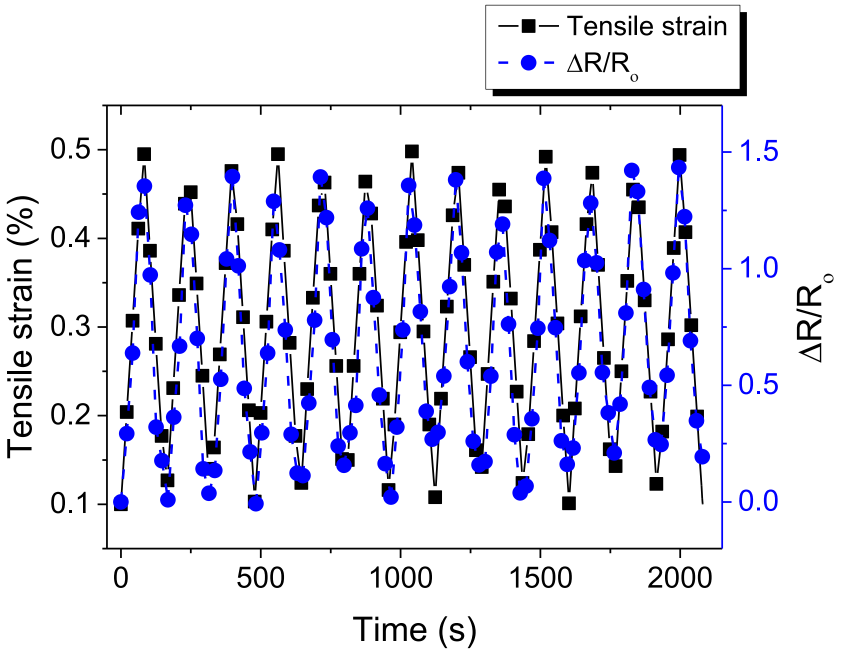

Figure 4.45. Reversibility of the electrical response during a strain controlled test [190].

A similar test method was also applied in which the specimen was loaded in cyclic flexural mode under load control (0-25 MPa). As shown in **Figure 4.46**, the piezoresistive behavior the multiscale composite is also replicated in flexural mode which confirms the rGO coating on GF can provide the possibility of a strain monitoring based on the control of the electrical resistance variations.

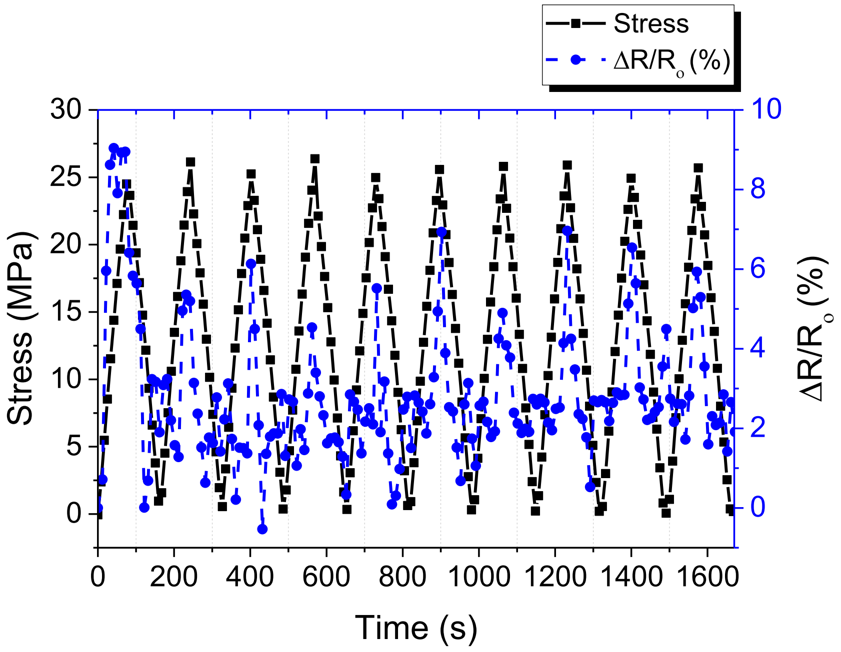

Figure 4.46. Reversibility of the piezoresistive behavior under flexural loading.

4.7.3 Dielectricity

As a control test, the permittivity of uncoated fiber composite was measured at room temperature and, as it can be seen in **Figure 4.47a**, it did not show any change in permittivity level with the change in applied frequency which is in accordance to the permittivity of common polymers (<10) [191]. The coating of GF with GO did not provide any capacitive properties at room temperature either due to the insulating nature of GO. In the case of rGO coated fibers, however, the composite showed an improvement over the entire frequency range. At 100 Hz the permittivity value increased by a factor of 3.6 when compared to the value measured on the composite with uncoated fibers. The induction of permittivity in glass/epoxy composites was due to the presence of rGO interphase which possesses a conductive nature. This was proved in our electric conductivity measurement of the composites based on rGO interphase as in the section 4.7.1. A similar trend was also obtained in the case of dissipation factor of the composites while being tested for their capacitive properties as shown in **Figure 4.47b**

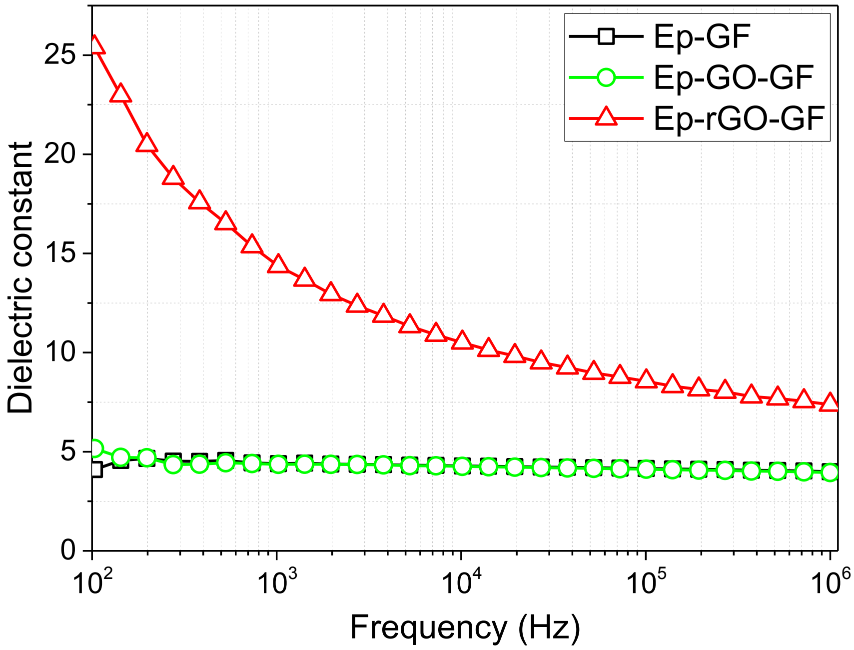

a)

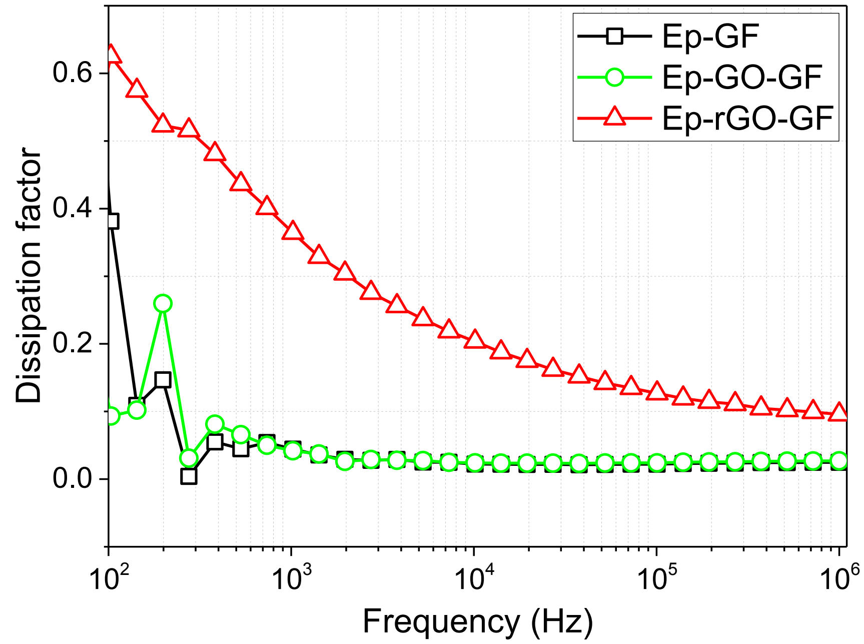

b)

Figure 4.47. Dielectric properties of the composites (EP-GF, Ep-GO-GF and Ep-rGO-GF) where a) shows the permittivity (or dielectric constant) related to the applied frequency and b) is the associated dissipation factor (or dielectric loss) when compared to the value measured on the composite with uncoated fibers.

4.7.4 Thermal conductivity

The influence of having a unidirectional interphase in the form of GO and rGO on the thermal conductivity of samples was evaluated by testing the composite samples without and with graphene interphase (GO and rGO). The samples were tested on three different temperatures i.e. 25, 50 and 75 °C in order to validate our argument of having better thermal conductivity in fiber direction. **Figure 4.48** reveals the effect of the presence of an interphase along the direction of fiber (i.e. x-axis of the composite) in the fiber reinforced composites produced. It is interesting to observe that for all investigated temperatures, thermal conductivity of composites containing GO and rGO coated fibers was significantly higher that of composites with uncoated fibers. Moreover, as expected, the thermal conductivity values of composites with rGO coated fibers were higher than that prepared with GO coated fibers. This increase in conductivity was based on the high thermal conductivity of rGO as compared to GO nanosheets which confirms the successful reduction of GO during chemical treatment with hydrazine hydrate (as described in the section **3.1.3.3**). This also shows the advantage of aligning the nanosheets as a continuous interphase between the matrix and fiber, even with a very low content of rGO nanosheets, which improved the thermal conductivity by 20% as compared to neat composites (without any interphase).

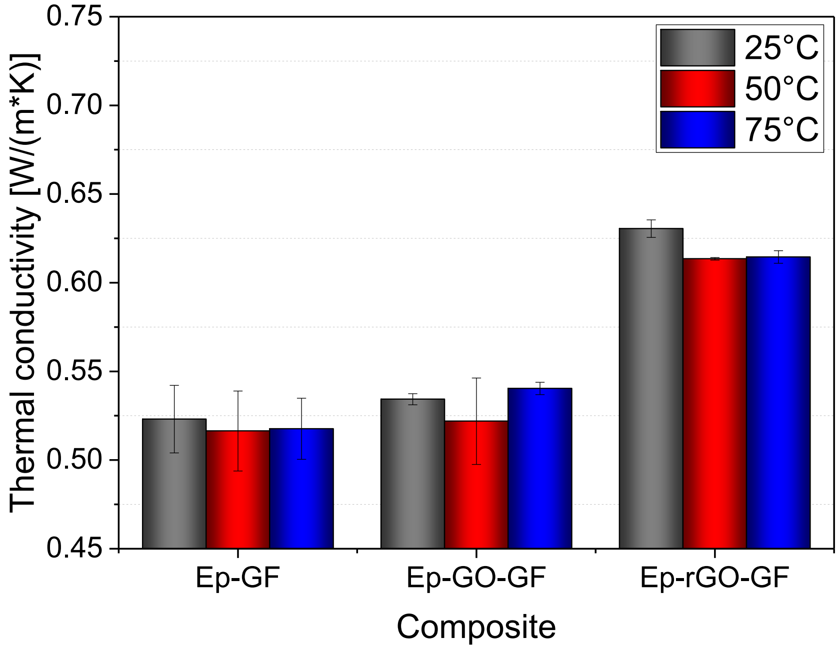

Figure 4.48. Thermal conductivity of three composites in x-axis direction with respect to fiber orientation.

Along the y- and z-axis of the composites, which do not have any continuous interphase, the thermal conductivity did not showed any significant change (**Figure 4.49** & **Figure 4.50**). This was due to the very low content of GO or rGO nanosheets along these two directions which makes it impossible to create a percolation threshold enough to improve the thermal conductivity as like in the x-direction (along the fiber) which contains a continuous interphase.

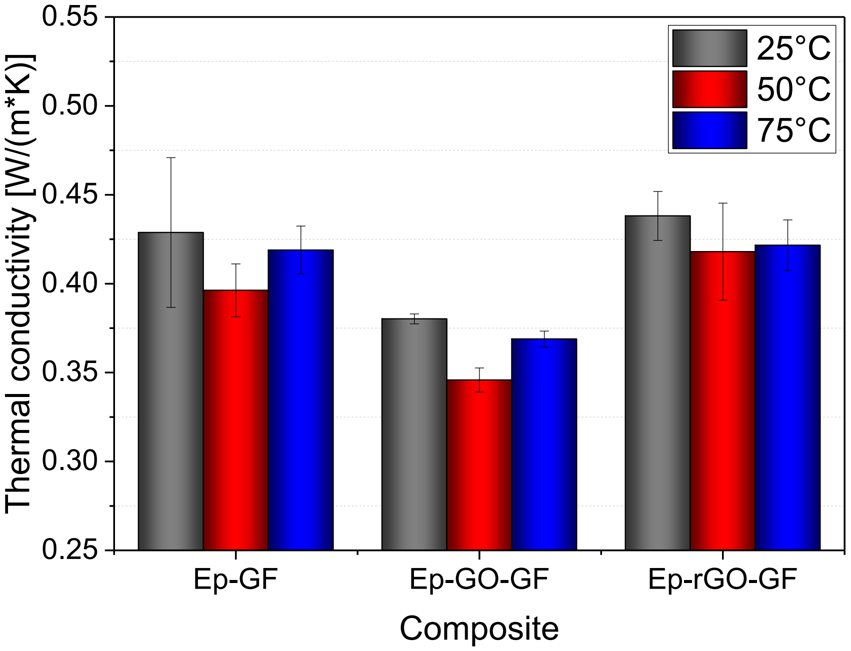

Figure 4.49. Thermal conductivity of three composites in y-axis direction with respect to fiber orientation.

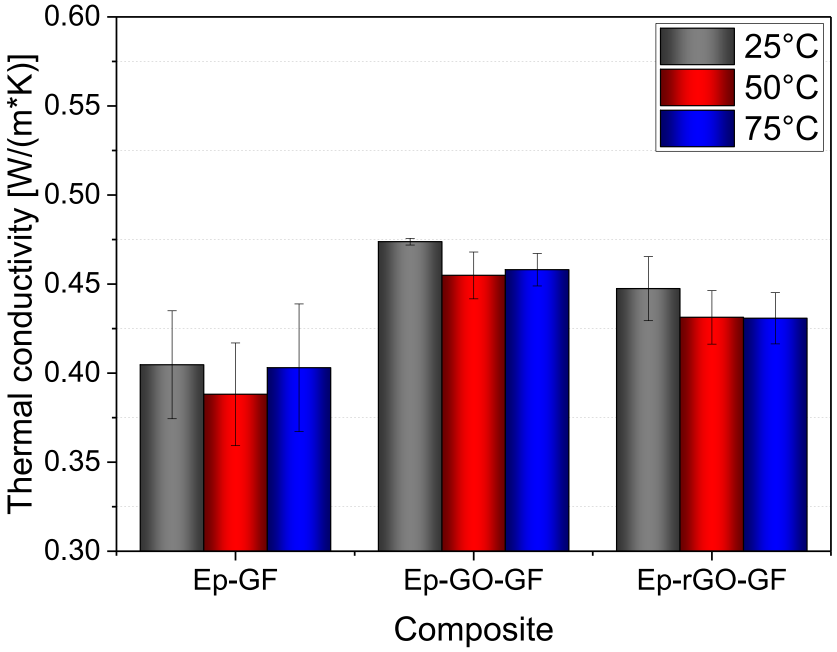

Figure 4.50. Thermal conductivity of three composites in z-axis direction with respect to fiber orientation.

A comparison of thermal conductivity obtained in the composites containing GF (uncoated, GO and rGO coated fibers) along all orientations of the composite specimen at 25°C summarizes the improvement of thermal conductivity. The improvement was achieved because of the presence of rGO nanosheets only when the filler was aligned along the fiber direction thus creating a continuous network of rGO coating which is in agreement to the result obtained during the electrical conductivity measurement (**Figure 4.41**).

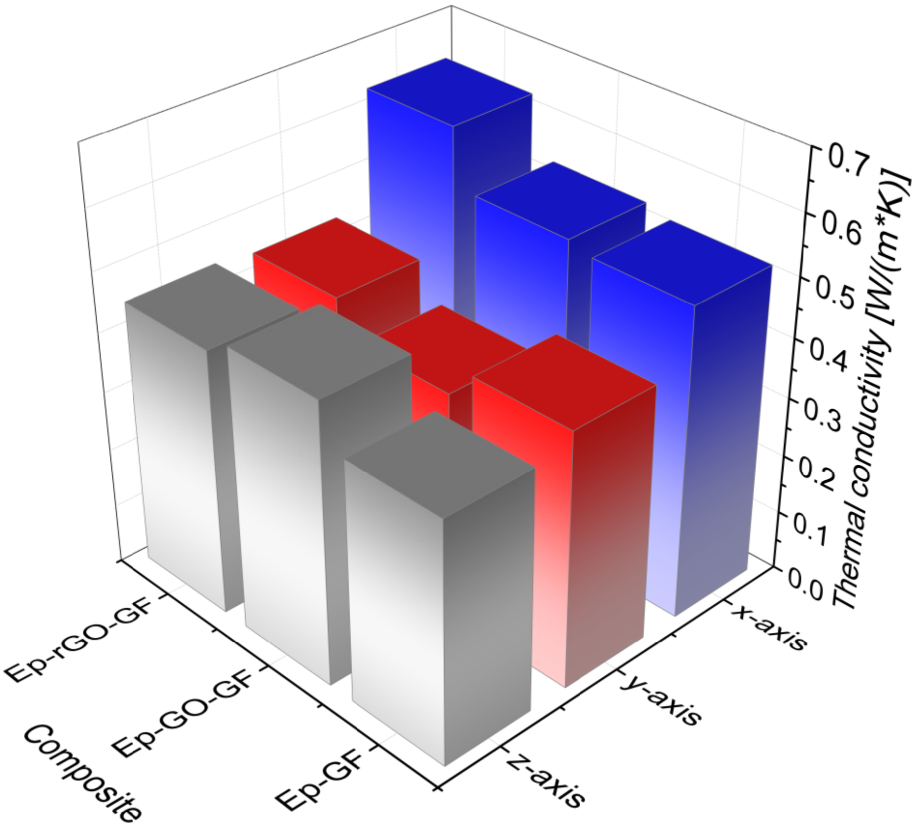

Figure 4.51. Thermal conductivity of three composites at 25°C along three mutually orthogonal directions.

Chapter 5 - Conclusions and future developments

In this study, graphene oxide (GO) and reduced graphene oxide (rGO) based epoxy/glass composites were prepared in which the glass fibers (GF) were coated with GO and rGO. The coating of GO on GF was performed using electrophoretic deposition (EPD) of GO at optimized parameters to obtain a homogenous coating of GO. While to obtain rGO coated GF, the GO coated fibers were subjected to chemical reduction at elevated temperature to produce rGO coated GF. Both these types of fibers were used to create micro- and macro-composites to evaluate various mechanical and functional properties induced to the presence of a graphene-based interphase.

Conclusion on micro-analysis of coated fibers and their composites

Single fiber fragmentation tests of epoxy microcomposites based on single uncoated, GO coated and rGO coated glass fiber revealed that microcomposites containing GO interphase deposited at 10V/cm offered a higher interfacial shear strength (ISS) with the value being 218% than that obtained with uncoated fibers. The factors associated to the increase in adhesion strength were evaluated to be related to the physical and chemical nature of the GO based interphase. For the prior case, it was found that the higher the thickness of the GO coating, the higher was the roughness value of the coating hence contributing towards the "physical" bonding between the fiber and matrix. Moreover, the friction force microscopy (FFM) analysis on GO coated fiber revealed that the coating possessed an interfacial strength of 130 MPa which was 4 times higher than the highest ISS value of the microcomposite thus confirming the positive effect of enhanced interfacial adhesion in epoxy/glass composites. The "chemical" contribution towards the improvement of ISS was governed to be the oxygen functional groups attached to the GO nanosheets which was confirmed by x-ray diffraction (XRD), x-ray photoelectron spectroscopy (XPS) and Fourier transform infrared spectroscopy (FTIR) analysis.

In case of rGO based microcomposites, a 70% increase in ISS was observed for the highest electrical field used for the EPD process. The absence of oxygen based functional groups precluded any chemical bonding between the matrix and the rGO coating on the GF hence the load-transfer was less efficient through the rGO interphase. The increase of ISS as compared to epoxy/glass microcomposite can therefore be attributed to the roughness of rGO nanosheets coated on GF.

Conclusion on mechanical tests of composites

To further evaluate the enhanced mechanical properties due to the deposition of a graphene based interphase, epoxy composites prepared by using uncoated, GO coated and rGO coated fibers were produced by a hand lay-up method. These composites were subjected to various mechanical tests and it was observed that:

- GO and rGO interphase in composites improved the flexural stiffness and strength which was confirmed in mechanical tests performed in 3 point bending configuration. It was observed that epoxy/glass composites with GO interphase possessed higher flexural modulus and flexural strength while rGO showed mild improvement in flexural properties which is consistent with the ISS investigation tests on microcomposites hence confirming the hypothesis of GO being a load-transferring bridge in epoxy/glass composites.
- Short-beam shear (SBS) tests provided similar information. In fact, composites based on GO interphase showed an increased interlaminar shear strength while rGO coating only slightly improved the interlaminar shear strength. A closer look at the samples failed under SBS tests through optical microscope revealed the interlaminar shear failure where rGO based composites contained more cracks as compared to GO based composites.
- Mode I fracture toughness tests on the composites confirmed the positive influence on the interfacial adhesion between epoxy/glass composites exerted by GO interphase. On the other hand, rGO based epoxy/glass composites suffer from poor strength in opening mode loading in which the failure occurred at epoxy/rGO interface as revealed by fractographic analysis.
- An investigation of the creep behavior of the composites reveal that graphene interphase in epoxy/glass composites offers excellent resistance to creep deformation. Here, again the GO interphase offers best results in creep stability and fitting of the creep data using Findley’s model was effective in modelling the creep behavior in which the parameters D_e and k being substantially reduced by the presence of the interphase.

Thus in a nutshell, it is confirmed and proved that GO nanosheets possess excellent load-transfer capabilities when combined in epoxy/glass composites as a continuous interphase hence offering the possibility of creating high end multiscale composites for many engineering applications.

Conclusion on functional properties of composites

Graphene being an “active” nanomaterial offers diverse range of possibilities of creating multifunctionality in polymer composites. In this work, different type of analysis were performed to analyze the functionalities present in the composite material. It was shown that:

- Electrical resistivity measurements revealed that rGO based epoxy/glass composites offer little resistance due to the conductive nature of rGO nanosheets, whereas there was no difference between the composites based on uncoated and GO coated fibers (which showed insulating behavior). An in-depth analysis revealed that the directional orientation or rGO nanosheets along the length of the fibers offered the lowest resistivity as compared to other orientations hence confirming the advantage of oriented and aligned rGO interphase for tailored functional properties.
- To verify the possibility of using rGO coated GF as strain sensing device, the composites were tested for their piezoresistivity behavior. The composites showed change in absolute resistance with the applied load or applied strain, thus the strain monitoring phenomenon was confirmed in the rGO based epoxy/glass composites.
- The conductive behavior of epoxy/glass composite containing rGO interphase also induced the property of permittivity in the composites. This was verified along with the other composites containing uncoated and GO coating fibers. This functionality offers the possibility to use such composites for electromagnetic interference shielding in advanced applications.
- Other than electrical functionalities, aligned rGO interphase along with the fibers in epoxy/glass composites offered better thermal conductivity. This was verified by comparing the thermal conductivity values along other orientations of the composite based on either uncoated, GO or rGO coated GF. This result supports the advantage of aligning graphene interphase in epoxy/glass composites for improved functional properties.

Overall, the presence of an aligned and oriented graphene interphase in fiber reinforced polymer composites offer multitude of possibilities in improving the engineering and technical aspects of the composites not only limited to mechanical terms but also in other functional areas where the idea of weight reduction and hence achieving even better strength-to-weight ratio could be realized. The mechanical properties of functional composites (rGO based) is the area to further explore, the limitation that could restrict the use of reduced graphene oxide in the world of composite materials.

Publications in peer reviewed journals and books

- Karger-Kocsis, J., **Mahmood, H.**, & Pegoretti, A. (2015)., Recent advances in fiber/matrix interphase engineering for polymer composites. *Progress in Materials Science*, *73*, 1-43.
- **Mahmood, H.**, Tripathi, M., Pugno, N., & Pegoretti, A. (2016). Enhancement of interfacial adhesion in glass fiber/epoxy composites by electrophoretic deposition of graphene oxide on glass fibers. *Composites Science and Technology*, *126*, 149-157.
- Pegoretti, A., **Mahmood, H.**, Pedrazzoli, D., & Kalaitzidou, K. (2016, July). Improving fiber/matrix interfacial strength through graphene and graphene-oxide nano platelets. In *IOP Conference Series: Materials Science and Engineering* (Vol. 139, No. 1, p. 012004). IOP Publishing.
- Fakhri, P., **Mahmood, H.**, Jaleh, B., & Pegoretti, A. (2016). Improved electroactive phase content and dielectric properties of flexible PVDF nanocomposite films filled with Au-and Cu-doped graphene oxide hybrid nanofiller. *Synthetic Metals*, *220*, 653-660.
- Karger-Kocsis, J., Kékic S., **Mahmood H.**, Pegoretti A., Interphase engineering with nanofillers in fiber-reinforced polymer composites, in: K. Mittal, A. Netravali (Eds.) Interface/Interphase in Polymer Nanocomposites. John Wiley & Sons, 2016.
- **Mahmood, H.**, Unterberger, S.H & Pegoretti, A. Multifunctionality in epoxy/ glass composites by a deposited graphene interphase. *In-preparation*.
- **Mahmood, H.**, Venzetti, L, Bersani, L, & Pegoretti, A. Strain monitoring in glass-epoxy composites with graphene-coated fibers. *In-preparation*.
- Tripathi, M., **Mahmood, H.**, Novel, D., Iacob, E., Venzetti, L, Pegoretti, A., Pugno, N. Nanoscale friction and wear analysis of graphene oxide over glass-fiber and polystyrene. *In-preparation*.

Participation to congresses, schools and workshops

- **Mahmood, H.**, Pegoretti, A., Enhancement of interfacial adhesion in glass fiber/epoxy composites using graphene nanosheets. *20th International Conference on Composite Materials, Copenhagen*, 19-24th July 2015
- **Mahmood, H.**, Bersani, M., Pegoretti, A., Strain monitoring of glass fiber epoxy composites using a reduced graphene oxide deposited interphase, *ECCM17 - 17th European Conference on Composite Materials, Munich, Germany*, 26-30th June 2016
- Dul, S., **Mahmood, H**., Fambri, L., Pegoretti, A., Graphene-ABS nanocomposites for fused deposition modelling, *ECCM17 - 17th European Conference on Composite Materials, Munich, Germany*, 26-30th June 2016
- **Mahmood, H.,** Pegoretti, A., Tailoring the interphase in glass fiber/epoxy composites through electrophoretic deposition of graphene oxide, *3a Giornata sul Grafene e Ossido di Graphene, Salerno, Italy,* 9 September 2016
- **Mahmood, H.**, Birhane, G., Pegoretti, A., Inducing multifunctionality by graphene interphase in fiber reinforced epoxy composites. *ICNN4 – 4th International Conference on Nanomechanics and Nanocomposites, Vicenza, Italy*, 14-17 September 2016

Chapter 6 - Collateral research activities

6.1 Inducing multifunctionality by graphene interphase in fiber reinforced epoxy composites.

Part of this paragraph has been published in:

Haroon Mahmood, Gashaw Birhane, Alessandro Pegoretti

"Inducing multifunctionality by graphene interphase in fiber reinforced epoxy composites" In *'Proceedings of ICNN4 – 4th International Conference on Nanomechanics and Nanocomposites' 14-17 September 2016, Vicenza, Italy,*

This study presents the opportunity of creating epoxy/basalt fiber hierarchical composites by depositing graphene nanosheets on continuous basalt fiber (BF) using an electrophoretic deposition technique. Graphite oxide was prepared by modified Hummer's method and using ultrasonication technique, graphite oxide was exfoliated in deionized water to create a stable suspension of graphene oxide (GO). This suspension was used as a bath to deposit GO on BF at a particular applied electric field (V/cm) for 5 min. After deposition of GO on both sides of BF, the coated fibers were dried and used to create single fiber reinforced epoxy composites for adhesion analysis. Single fiber fragmentation test revealed an increased interfacial shear strength (ISS) value by 87% thus suggesting the effect of GO interphase creating favorable load-transferring conditions between matrix and fiber.

In another case, the coated fibers were subjected to chemical reduction process to reduce the GO coating. These reduced graphene oxide (rGO) coated fibers were used to create multifiber reinforced epoxy composites. Electrical conductivity tests revealed lowering of electrical resistivity by a factor of 10^{12} in case of rGO interphase reinforced composite as compared to uncoated fiber reinforced composites. The change in electrical resistance was observed with the variable applied strain confirming the possibility of graphene coated fibers to be used as strain monitoring sensors in load-bearing components.

Modern era of engineering and technology has compelled material scientist to create load bearing structures with advance properties. These properties are not only limited to mechanical performance of the composites but also in terms of ‘active’ nature of the structures created. An example of this is the aerospace industry where importance is given primarily to the safety. A crucial aircraft structure requires not only to have exceptional mechanical properties but also sees to have advanced multifunctional properties to detect flaw and defects during service with ease. Recent years have observed a growing importance in the incorporation of graphene nanosheets in polymer based composites due to its exceptional properties like mechanical properties, high thermal and electrical conductivity [63, 65]. Recent studies has confirmed the synergetic effects, both in terms of structural and functional properties, by polymer nanocomposites with graphene loading [60, 192]. This current report shows different types of graphene-based nanosheets in epoxy/basalt composites in which an interphase was created by these graphene nanosheets (graphene oxide and reduced graphene oxide) between the continuous fiber and matrix. The resultant composites are tested for their mechanical and functional properties.

6.1.1 Microcomposite preparation and testing:

The matrix used in this work was a bicomponent epoxy resin (epoxy base EC 252 and hardener W 241) provided by Elantas Italia S.r.l. The physical properties of the epoxy resin after curing at room temperature for at least 3 h followed by 15 h at 60°C are summarized in **Table 6-1**. Basalt fibers were provided by RG Faserverbundwerkstoffe GmbH (Waldenbuch, Germany) and had a diameter of 15.0 ± 0.1 μm. These fibers were used as received without any further treatment.

Table 6-1. Physical property of the selected epoxy resin.

Physical property	**Value**
Glass transition temperature (T_g)	27.9°C
Thermal degradation	375°C
Tensile strength (σ_T)	26.1 ± 1.1 MPa
Young’s modulus	738 ± 14 MPa

Mechanical properties of fibers was evaluated by single fiber tensile testing. Around 31 single fiber specimens were subjected to tensile testing using an Instron® 4502 universal tensile tester fitted with a 10 N load cell. A common gage length of 20 mm was applied and tests were performed at 0.2 mm/min. **Table 6-2**. shows the summary of data reduction obtained for basalt fiber through the iterative procedure proposed by Gurvich et al [176].

Table 6-2. Mechanical properties of basalt fiber determined from single fiber tensile tests. (N = number of specimens, $\overline{R}$ = average strength at L = 20 mm, σ_0 = scale parameter at L_0 = 5 mm, m = shape parameter, ν= coefficient of variation).

Physical property	**Value**
N	31
$\overline{R}$	1604 MPa
σ_0	2282 MPa
m	5.1
ν	21.5 %

Modified Hummer's method was utilized to synthesis graphene oxide [173]. The obtained product was dried in an oven under vacuum at 40°C to get a brown colored graphite oxide cake. The obtained graphite oxide was dispersed in deionized water at a concentration of 1 mg/ml using a powerful tip ultrasonication device for 1h. This resulted in a stable homogenous GO dispersion which was later used for deposition on basalt fibers.

Since the fibers are non-conductive in nature, two copper plates were used as electrodes in the EPD process in which fibers (fixed on a window frame) were placed near the anode. This was due to the fact that GO contains negative charges due to oxygen based functionalities attached during the GO synthesis reaction. In the EPD process, hence, GO migrated towards the anode and got deposited on the fibers. Deposition was carried out at a determined voltage of 20 V with a constant deposition time of 5 min and electrodes gap of 2 cm (overall electrical field of 10V/cm). To coat the fibers homogenously, a second EPD cycle was performed under the same conditions while reversing the fibers. Drying of the fibers was carried out in an oven under vacuum at 40°C for 12 h.

Scanning electron microscopy (SEM) analysis coated fibers revealed the morphology of the fibers after deposition as shown in **Figure 6.1**. The GO coating almost spread along the length of the fiber with homogenous thickness. Some rough spots can be seen due to the multilayer coating of the GO sheets due to stacking and also because of the characteristic wrinkling of the 2D nanosheets and membranes.

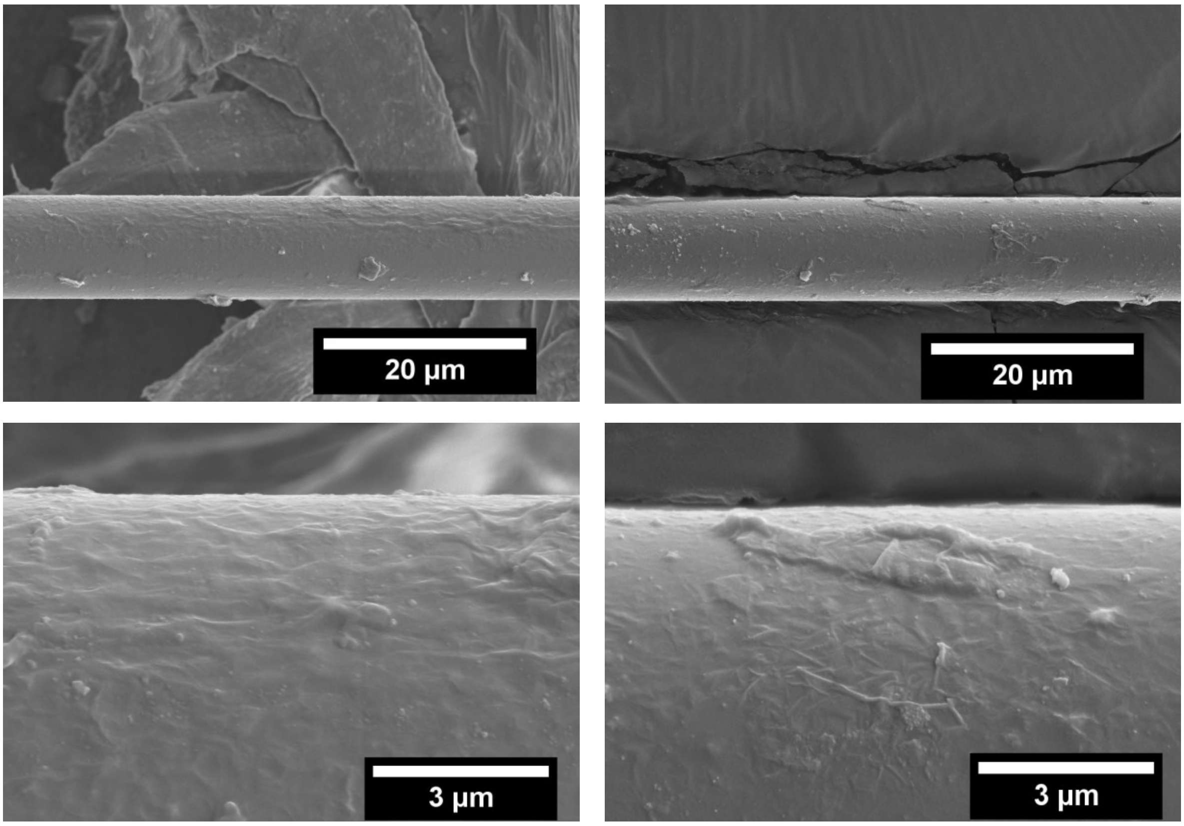

Figure 6.1. SEM images of basalt fiber coated by GO.

Interfacial shear strength (ISS) between fiber and matrix was evaluated by single fiber fragmentation tests (SFFT). For this, a tensile tester (Minimat, by Polymer Laboratories, Loughborough, UK) was employed to perform tests at room temperature while a polarized optical stereo-microscope (Wild M3Z by Leica) was used to monitor the fiber fragmentation process during the tensile test. The test was conducted at a cross-head speed of 10 mm/min up to 10% strain, necessary to guarantee the saturation of the fragmentation process. The mean fiber length at saturation, L_S, was measured by an image analysis software (Image J) where the critical fiber length value, L_C, was considered to be equal to (4/3) L_S. ISS values were measured following the simplified micromechanical model of Kelly and Tyson [29]. The static equilibrium between the tensile force acting on a fiber and the shear force transferred through the fiber-matrix interface equates to an average value of ISS according to the following equation:

$$ISS = \frac{\sigma_{fb(L_c)} d}{2L_c} \tag{6-1}$$

where d is the fiber diameter and $\sigma_{fb(L_c)}$ is the tensile strength of the fiber at the critical length. This latter value can be calculated by considering a Weibull distribution for the fiber strength, i.e.:

$$\sigma_{fb(L_c)} = \sigma_0 \left(\frac{L_c}{L_0} \right)^{-\frac{1}{m}} \Gamma\left(1 + \frac{1}{m} \right) \tag{6-2}$$

where Γ is the Gamma function, σ_0 and m and the scale and shape parameters of the Weibull strength distribution at the reference length L_0, respectively. These parameters were evaluated above for single fiber tensile test at single gage length. The single-fiber fragmentation test revealed that the GO coating on the fibers has a positive effect on the load-transfer ability at the fiber/matrix interphase. As revealed in the **Figure 6.2**, the ISS values significantly improved by 87% when a GO coating was applied on fiber as compared to neat fiber. This could be attributed to oxygenated functional groups attached to GO which improve the load transfer phenomenon between the fiber and epoxy collectively. This positive effect could be also credited to the mechanical interlocking due to an increased surface roughness and good adhesive compatibility between GO and epoxy [187].

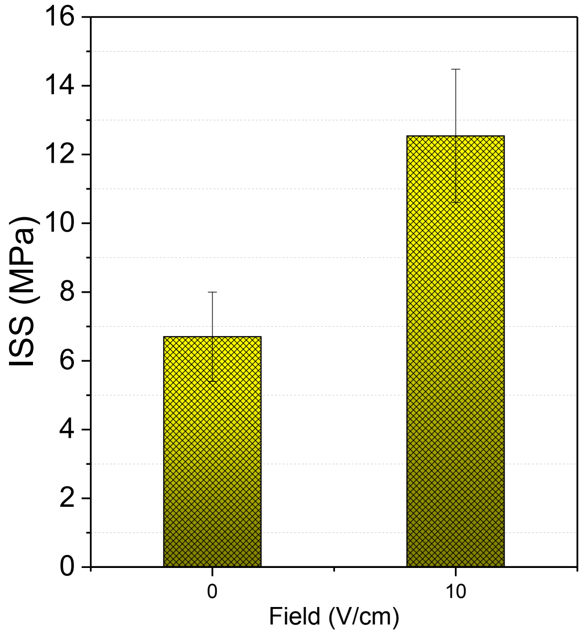

Figure 6.2. ISS values of GO coated BF reinforced epoxy composite as determined by SFFT.

6.1.2 Functional properties

The electrical resistivity was measured by 2 probe method and by varying the measurement orientation with respect to the specimen. In this work, electrical characterization and strain monitoring phenomenon were tested on BF/rGO reinforced epoxy hybrid composites. The volume resistivities of BF/rGO/Ep macrocomposite were calculated and compared as displayed in **Figure 6.3**. It can be visualized that the resistivity values in the longitudinal direction are pretty lower as compared to measurements in the transversal direction which basically shows the benefit of having continuous coating in unidirectional path. The network of graphene sheets, connected together end to end, provide a neat path with less hurdles.

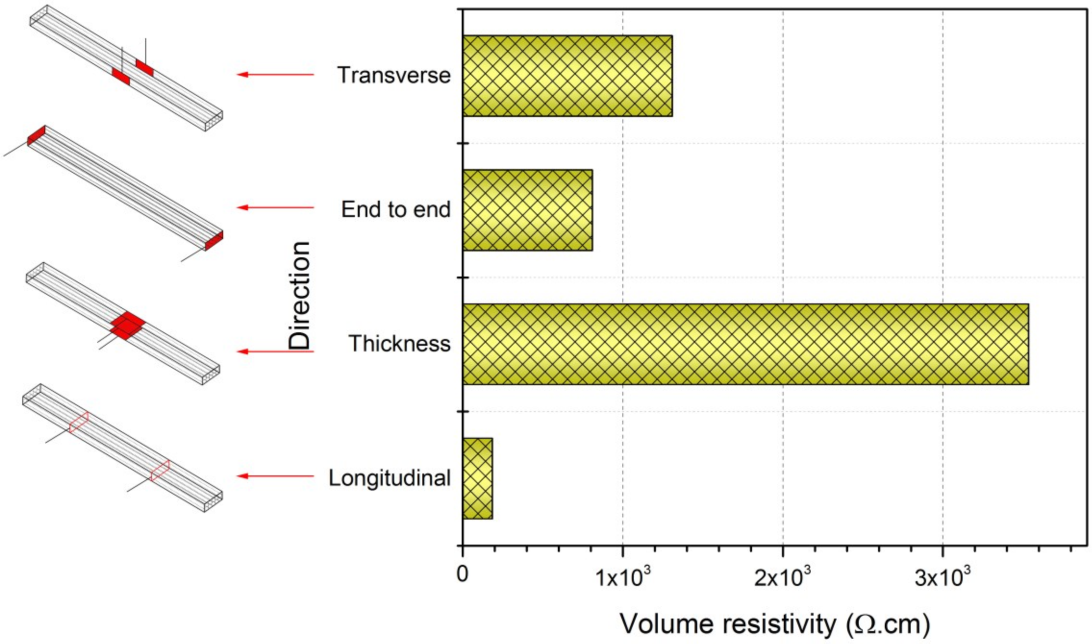

Figure 6.3. Electrical resistivity of BF/rGO/Ep macrocomposite along various direction as demonstrated by the schematic diagram of specimen being tested by applying 2 probe electrical resistivity measurement method.

To evaluate the piezoresistivity of such multiscale macrocomposites, a BF/rGO/Ep macrocomposite specimen was subjected to flexural loading and the change in electrical resistance was monitored on both surfaces of the specimen separately. In case of the base portion of the specimen which experiences tensile stress during flexural loading, piezoresistivity can be visualized with the aid of the stress curve in **Figure 6.4**. Until 1.5% of the flexural strain, the resistance change was increasing gently until the fibers of the specimen started to break which resulted in a massive change in the relative change of resistance. In the same respect, the piezoresistivity of the top surface of the specimen experiencing the compressive stresses can be visualized in figure 5b. Till the initial 1.5% flexural strain, the resistance decreased presumably that the compression stresses tend to improve the electrical contacts among the fibers and decrease in resistance but as soon as the fibers started to break, it had an intense effect on the relative change of resistance.

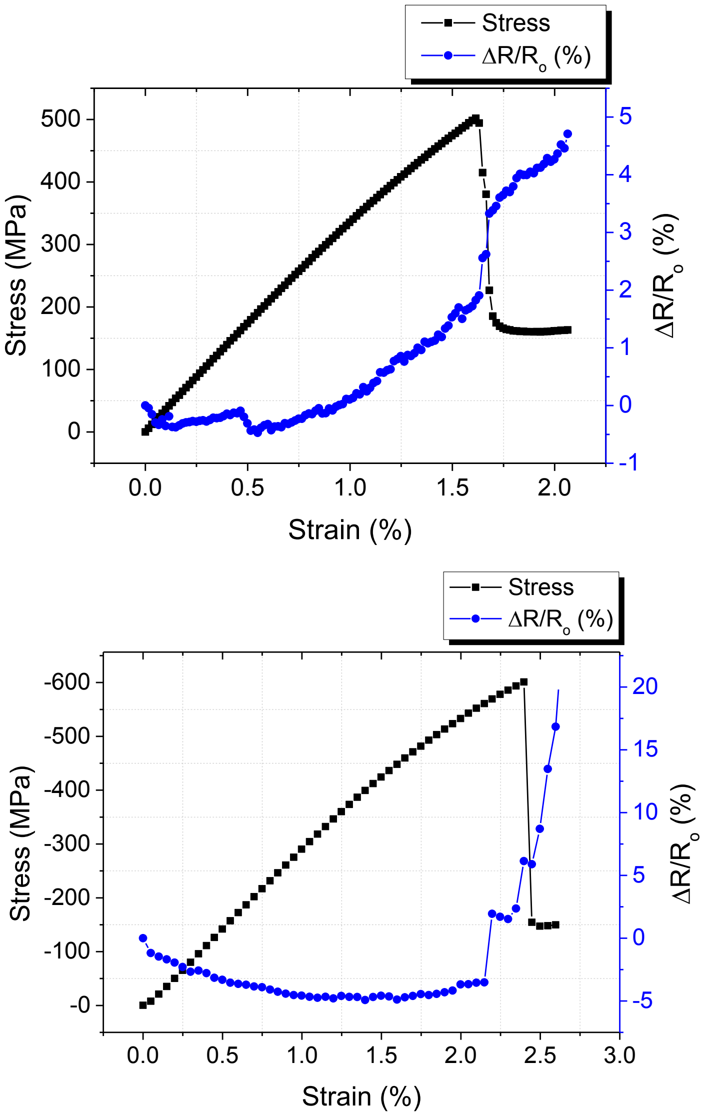

a)

b)

Figure 6.4. Piezoresistivity of BF/rGO/Ep composites under flexural loading with electrodes on: a) tensile subjected side, b) compression subjected side.

To evaluate the reversibility of the piezoresistivity, a cyclic compression loading was applied with at least 10 cycles of predetermined load. The resistance was measured by connecting the two terminals of the electrometer to the longitudinal ends of the specimen. **Figure 6.5** demonstrates the reversible piezoresistive behavior of the macrocomposites under compressional loading mode. It is interesting to note that the variation in the loading condition in cyclic manner can be recorded by the resistance change method which offers the possibility of using such multiscale composites for strain monitoring applications.

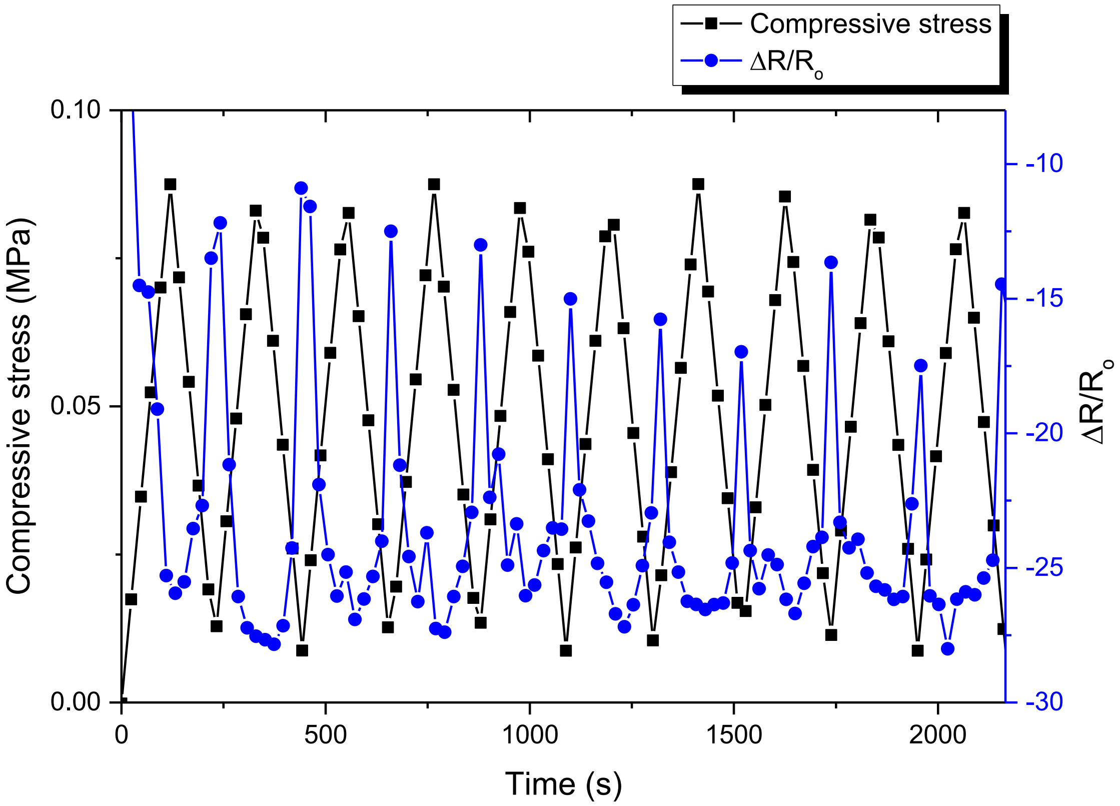

Figure 6.5. Reversible piezoresistivity of BF/rGO/Ep composites under compressional loading.

6.2 Improved electroactive phase content and dielectric properties of flexible PVDF nanocomposite films filled with Au- and Cu-doped graphene oxide hybrid nanofiller

Part of this paragraph has been published in:

Parisa Fakhri, Haroon Mahmood , Babak Jaleh, Alessandro Pegoretti
"Improved electroactive phase content and dielectric properties of flexible PVDF nanocomposite films filled with Au- and Cu-doped graphene oxide hybrid nanofiller"
Synthetic Metals 220 (2016) 653–660

In the present work, new and flexible poly(vinylidene fluoride) (PVDF) based nanocomposites containing Au- and Cu-doped graphene oxide (GO/Au and GO/Cu) nanosheets were prepared by solution casting. The resulting nanocomposites present a high content of electroactive phases and high dielectric constant accompanied with low dielectric loss which make them interesting for possible applications in sensors and electronic devices. Fourier transformed infrared spectroscopy (FTIR) was used to study the crystalline structure of nanocomposites which showed no absorption band related to non-polar a phase. FTIR confirmed an enhancement of the electroactive phase with the increase in nanofiller concentration due to the electrostatic interactions among the CH2-CF2 dipoles of PVDF and nanofiller. Electroactive phase content as calculated from FTIR spectra presented a maximum value of about 95% for PVDF filled with 1% GO/Au nanofiller. This value is about 2.5 times higher than that of neat PVDF. For a given filler concentration, nanocomposites filled with GO/Au showed a higher increase of electroactive phase in comparison with those containing GO/Cu. This trend was also confirmed by X-ray diffraction (XRD) spectra. From inductance, capacitance, and resistance (LCR) measurement, nanocomposites display high dielectric constant, increasing with the nanofiller content, and low dielectric loss which is favorable to fabricate flexible and simple high performance nanodielectric materials.

6.2.1 Nanocomposite phase analysis

6.2.1.1 Fourier Transform Infrared Spectroscopy

FTIR spectroscopy provides information about the structure of PVDF matrix that enables us to distinguish between the various possible crystalline forms. FTIR spectra of PVDF and related nanocomposites are reported in **Figure 6.6**. In the FTIR spectrum of neat PVDF, the peaks located at 530 cm^{-1} , 615 cm^{-1} , 763 cm^{-1} , 795 cm^{-1} , and 975 cm^{-1} represent the characteristic bands of the α phase, the absorption band at 510 cm^{-1} is related to β phase and the peak at 838 cm^{-1} is associated to γ phase [193, 194]. The peaks in the range 833-840 cm^{-1} can be related to both β and γ phase and is often difficult to distinguish. As both of these phases correspond to the polar electroactive phases of PVDF, for simplicity, it can be considered as a single polar phase [195]. However, in the present work the combination information coming from XRD analysis allowed used to establish that they are related to the γ phase. The peaks at 873, 1066 and 1163 cm^{-1} are not reported in the literature. In PVDF films loaded with GO/Au nanofillers whose FTIR spectra are reported in **Figure 6.6a**, all characteristic bands related to α-phase completely disappear and the absorption intensity of peaks related to γ phase increase. Moreover, also a new peak at 1232 cm^{-1} related to γ phase appears. These results reveal that the addition of GO/Au nanoparticles to PVDF can induce a transition from nonpolar α-phase to polar γ phase. In fact, none of the characteristic α-phase absorption bands can be observed in the GO/Au-PVDF nanocomposite films. A decrease of the the intensity of all peaks of 5.0GO/Au-PVDF is related to an increase in the thickness and opacity of nanocomposite films at the maximum percentage of nanofiller loading and does not reflect changes in the crystalline structure of PVDF. FTIR spectra of GO/Cu-PVDF nanocomposites are shown in **Figure 6.6b**. For low filler concentration, no appreciable changes have been found for absorption intensity of nonpolar α phase of nanocomposites as compared to neat PVDF spectrum. Increasing nanofiller loading led to a conversion of the nonpolar α phase to γ electroactive phase. In fact, the 5.0GO/Cu-PVDF nanocomposite exhibited predominantly the polar phase as documented by a peak centered at ~838 cm^{-1}. Compared with the GO/Cu nanoparticles, GO/Au nanoparticles show a higher efficiency in promoting the polar phase at the same amount of nanofiller. The transformation of α phase into electroactive γ phase can be explained by the electrostatic interactions between surface charge of nanofillers and CF_2 dipoles of PVDF. Indeed, due to the presence of charge dissimilarity in the surface of nanofillers, some CH_2–CF_2 dipoles are attracted and some of them are repelled, that results in the formation of γ phase. It may be also possible that, the functional groups presents in GO/Au and GO/Cu can interact with the F and H atoms of PVDF via hydrogen bonding [194, 195].

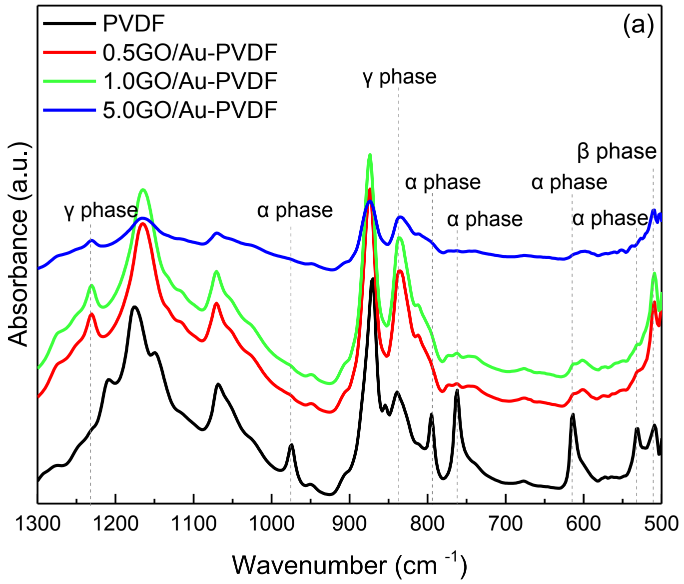

a)

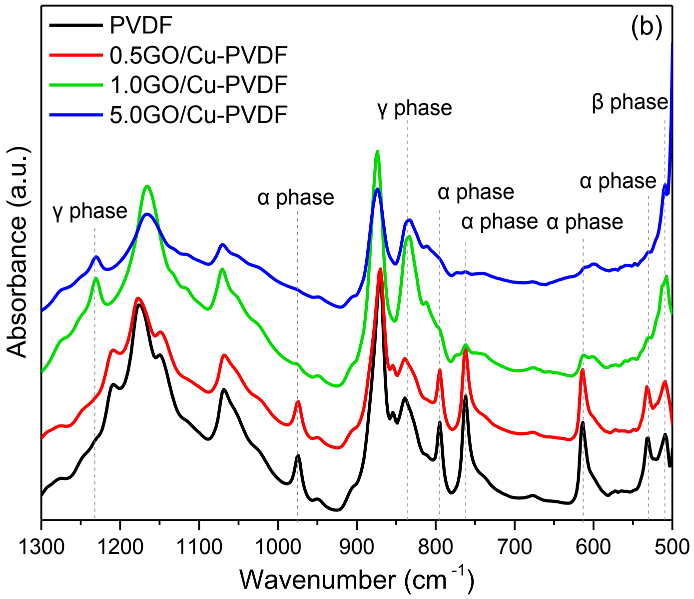

b)

Figure 6.6. FTIR spectra of pure PVDF and PVDF nanocomposite containing various amounts of (a) GO/Au and (b) GO/Cu nanofillers.

FTIR spectroscopy can also be used to determine the relative amount of γ phase using the following equation [193]:

$$F(\gamma) = \frac{A_\gamma}{\left(K_\gamma / K_\alpha\right) A_\alpha + A_\gamma} \tag{6-3}$$

where A_α and $A\gamma$ are the absorbance at 763 cm^{-1} (α-form) and 838 cm^{-1} (γ-form), Kα and Kγ are the absorption coefficient at the respective wavenumbers, with the value of 0.365 and 0.150μm^{-1} . Using Equation 6.3, the γ phase content of the nanocomposites were calculated. The relative γ phase content of neat PVDF was 41%. For GO/Cu-PVDF nanocomposites, this amount increased to reach a maximum of ≈95% for nanocomposite loaded with 0.5% and 1.0% GO/Au. Also, in nanocomposite filled with GO/Cu, γ-phase content was calculated to be 66% and 90% for 5.0GO/Cu-PVDF and PVDF-1% GO/Cu respectively. This increase of polar phase due to such low filler loading has not been reported yet in literature.

6.2.1.2 X-ray diffraction

The XRD patterns of neat PVDF and PVDF nanocomposite films are reported in **Figure 6.7**. The peaks of neat PVDF appear at 2θ of ≈ 17.8°, 18.4°, 19.93° and 26.9° which correspond to the diffraction planes of (100), (020), (110) and (021) generally attributed to nonpolar a phase [193]. These indicate that α phase is predominantly formed during the crystallization process of neat PVDF. From **Figure 6.7a** it can be seen that by adding GO/Au nanoparticles to PVDF, two diffraction peaks at 2θ of ≈ 17.8°, 18.4°, related to a phase, completely disappear and a single peak at 20.6° is seen, which corresponds to the diffraction from (100) plane indicating the stabilization of polar γ phase in the nanocomposite. All α, β or γ phases have an intense peak around 20°, thus it is difficult to distinguish from each other by only XRD analysis. In general, the β phase can be characterized by the presence of only one peak at 20° in the whole XRD spectra [193]. The combination of XRD result with FTIR technique (explained in previous section) confirms the remarkable transformation of nonpolar α phase to polar electroactive γ phase induced by the addition of GO/Au to the PVDF and also indicates a good interaction between nanofiller and matrix. The peaks at 2θ values of 38.1° (111), 44.3° (200), 64.5° (220), 77.5° (311) and 81.7° (222), that are observable only in 5.0GO/Au-PVDF spectrum, are consistent with the standard XRD data for Au (JCPDS 89-3697). From **Figure 6.7b**, by increasing Cu/GO amount in the nanocomposite, the peak intensity of the nonpolar α phase (at ≈ 17.6 and 26.6°) gradually decreases and finally in nanocomposite with 5.0%

nanofiller, these two peaks completely disappear. Also the peak at 19.93°, which is related to the γ phase, shifted to 20.4°. The peaks of **Figure 6.7b** located at 36.2°, 42.6° and 61.7° are attributed to copper oxide [196].

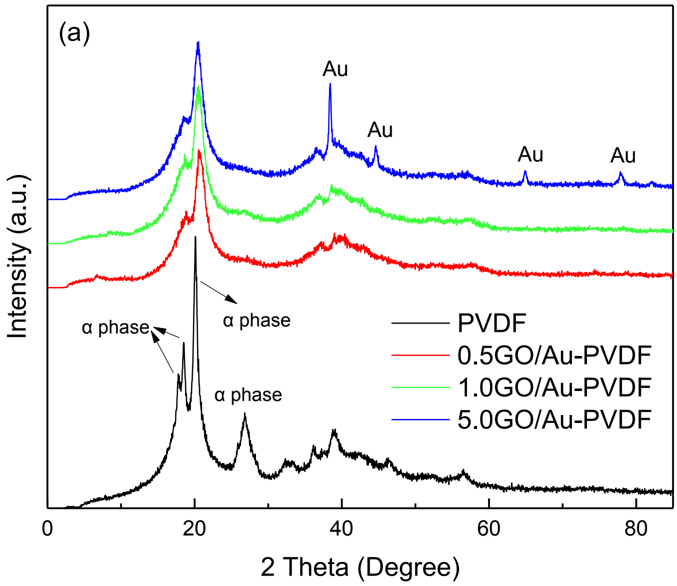

a)

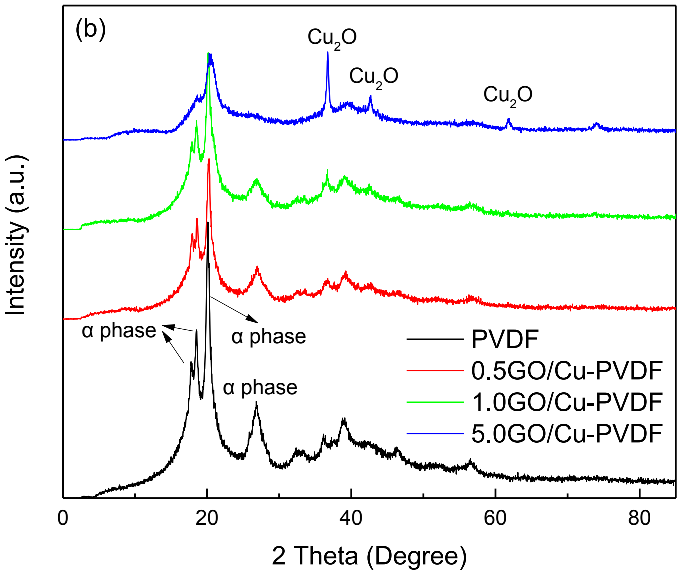

b)

Figure 6.7. X-ray diffraction patterns of neat PVDF and PVDF nanocomposites containing various amounts of a) GO/Au and (b) GO/Cu nanofillers.

By comparing **Figure 6.7a** and **Figure 6.7b**, it can be seen that in PVDF nanocomposite films filled with GO/Au nanoparticles, even by the inclusion of 0.5 wt.% of nanofiller, significant changes in the crystal structure of the polymer phase can be observed while these changes are less pronounced in GO/Cu-PVDF nanocomposite films.

6.2.2 Nanocomposite thermal analysis:

6.2.2.1 Differential scanning calorimetry

The electroactive property of PVDF strongly depends on the crystalline structure of the polymer, as well as on the electroactive polar phase formation in the nanocomposite [194]. Hence, the crystallization process of the neat PVDF and GO/Au- and GO/Cu-PVDF nanocomposite films was also investigated by DSC. The DSC thermograms under heating and cooling conditions of neat PVDF and its nanocomposites are presented in **Figure 6.8**. The crystallinity content (χ_c) of samples was calculated using the following equation:

$$X_c = \frac{\Delta H_m}{\Delta H^0{}_m \times \omega} \times 100 \tag{6-4}$$

where, ΔH_m is the melting enthalpy of the nanocomposite, $\Delta H^0{}_m$ m is the melting enthalpy of the 100% crystalline PVDF (104.7 J/g [197]) and ω is the weight fraction of PVDF in the nanocomposites [197]. χ_c values are listed in **Table 6-3.** Tm, Tc and χc values of PVDF and GO/Au-PVDF and GO/Cu-PVDF nanocomposite film at different nanofiller loadings along with the melting temperature (T_m) and crystallization temperature (T_c). It can be seen that the melting temperature and crystallization temperature gradually shifted to higher temperature in the nanocomposites by the increase of filler loading. This is related to well-dispersed nanofillers in the polymer matrix that acts as nucleating agent and inhibits the movement of polymer chain segments, resulting in improvement of the crystallization temperature of nanocomposite films. Moreover, it is observed that by adding GO/Au and GO/Cu, no remarkable changes in the crystallinity percentage of PVDF was observed. These observations indicate that the addition of nanofiller has little influence on the crystallization process of PVDF. Furthermore, electroactive properties of the PVDF depend on promotion of polar crystalline phases (i.e. β and γ phases) in polymer matrix. By addition of nanofillers, the relative percentage of γ phase in PVDF progressively increases, and a maximum extent of γ phase formation was achieved at 1.0 wt.% of the GO/Au loading [194].

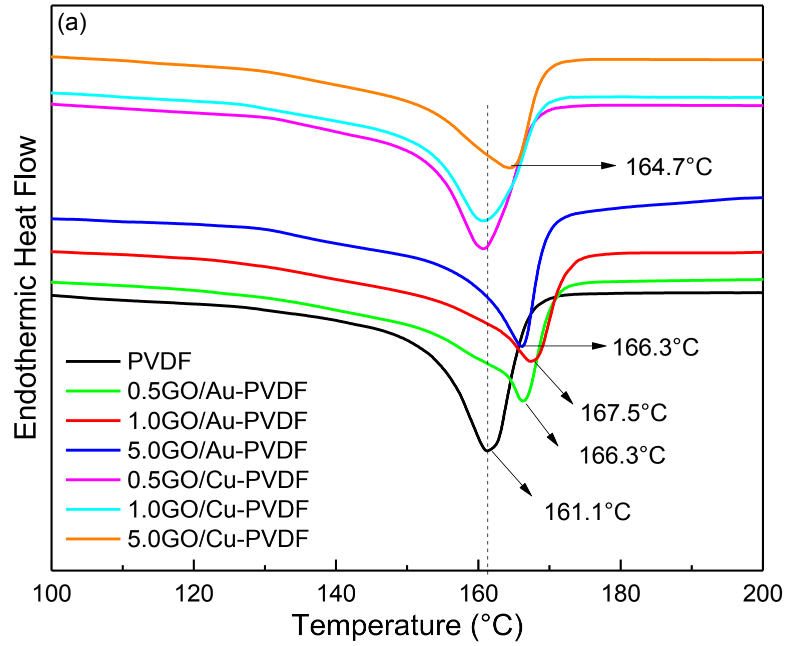

a)

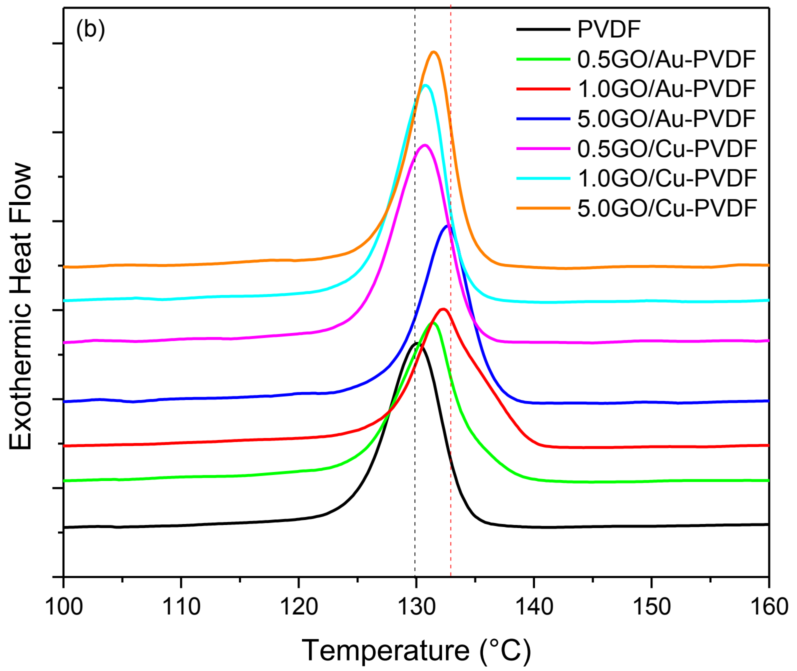

b)

Figure 6.8. DSC thermograms under a) heating and b) cooling conditions of pure PVDF, GO/Au-PVDF and GO/Cu-PVDF nanocomposite films at different nanofiller loading.

Table 6-3. T_m, T_c and χ_c values of PVDF and GO/Au-PVDF and GO/Cu-PVDF nanocomposite film at different nanofiller loadings.

Sample	T_m(˚C)	T_c(˚C)	X_c(%)
Neat PVDF	161.1	130.0	58
0.5GO/Au-PVDF	166.3	131.3	56
1.0GO/Au-PVDF	167.5	132.5	52
5.0GO/Au-PVDF	166.3	133.0	52
0.5GO/Cu-PVDF	161.0	130.5	55
1.0GO/Cu-PVDF	161.0	130.7	52
5.0GO/Cu-PVDF	164.7	131.5	53

6.2.2.2 Thermogravimetric analysis

TGA was performed to investigate the thermal stability of the neat PVDF and PVDF nanocomposites and the related thermograms are reported in **Figure 6.9**. As evidenced in the figure, a major weight loss occurs in the range from 450°C to 550°C which can be ascribed to the degradation of PVDF matrix. The onset degradation temperature, T_{onset}, was 490°C for neat PVDF, while the introduction of the nanofillers slightly increased the onset degradation temperature. In case of 0.5GO/Cu-PVDF, 1.0GO/Cu-PVDF and 5.0GO/Cu-PVDF, the degradation temperature onset shifted to 491°, 496°and 492°C respectively, while the degradation temperatures for nanocomposite containing GO/Cu were found to be 494°C, 499° C and 501°C for nanocomposites filled with 0.5% wt, 1.0% wt and 5.0% wt. respectively. The enhancement of thermal stability can be explained by the better packing of the polar crystallites in PVDF composites compared to the non-polar a phase of neat PVDF. Moreover, the interaction between the nanofiller and PVDF may result in the enhancement of the thermal stability of nanocomposites compared to neat PVDF [198].

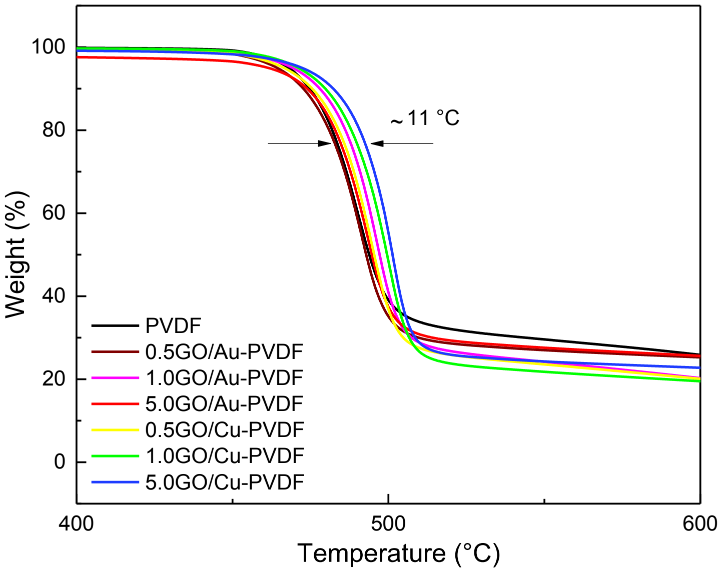

Figure 6.9. TGA thermograms of neat PVDF and relative nanocomposites with various amounts of GO/Au and GO/Cu.

6.2.3 Scanning electron microscopy

The fracture surfaces of GO/Au- and GO/Cu-PVDF nanocomposite films were analyzed using field emission scanning electron microscopy. **Figure 6.10** reveals the fracture surfaces of the neat PVDF and respective GO/Au and GO/Cu nanocomposite films. It is interesting to note that in case of GO/Au-PVDF films (**Figure 6.10b–d**), the nanofiller cannot be visualized thus indicating a good adhesion level between matrix and the filler. On the contrary, PVDF and GO/ Cu have poor adhesion between each other (**Figure 6.10e–g**).

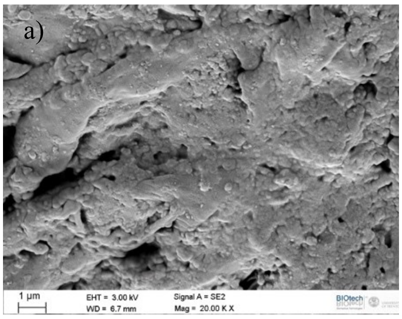

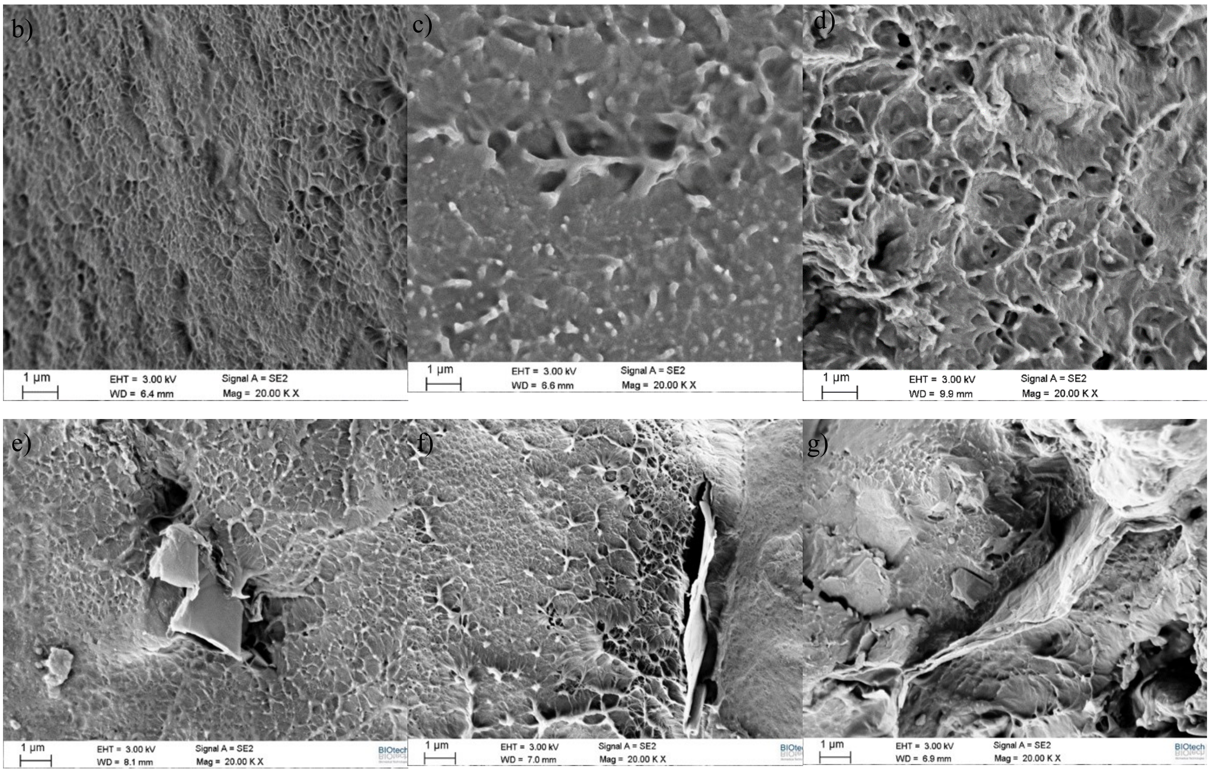

Figure 6.10. SEM observations on the cross section of a) neat PVDF, b) 0.5GO/Au-PVDF, c) 1.0GO/Au-PVDF, d) 5.0GO/Au-PVDF e) 0.5GO/Cu-PVDF, f) 1.0GO/Cu-PVDF and g) 5.0GO/Cu-PVDF.

6.2.4 Dielectric properties

Plots of relative permittivity (commonly known as dielectric constant) of the neat PVDF and PVDF nanocomposites measured at room temperature in a frequency range between 10^2 and 10^6 Hz are shown in **Figure 6.11a and b**. As it can be seen in **Figure 6.11a**, a remarkable improvement in relative permittivity in comparison to neat PVDF is observed even when only 0.5%wt of GO/Au nanoparticles are added to PVDF. It is worthwhile to observe that the increase of the dielectric constant values is proportional to the filler content. In fact, the dielectric constant measured at 10^3 Hz increases from about 5 (neat PVDF) to about 23 for 0.5GO/Au-PVDF, to about 31 for 1.0GO/Au-PVDF, to about 39 for 5.0GO/Au-PVDF nanocomposites. A similar behaviour can be observed in **Figure 6.11b** for the dielectric constant of nanocomposite thin films with 0.5, 1.0 and 5.0 % wt. of GO/Cu nanoparticles. In this case, at a frequency of 10^3 Hz the dielectric constant of neat PVFD is increased to about 12 for 0.5GO/ Cu-PVDF, to about 27 for 1.0GO/Cu-PVDF, to about 45 for 5.0GO/Cu PVDF nanocomposites. The observed behavior is consistent with what previously observed by He et al. on the effect of graphene oxide on the relative permittivity of PVDF nanocomposites films obtained using solvent N,N-Dimethylformamide (DMF) and cosolvent comprising deionized water/DMF combination [199].

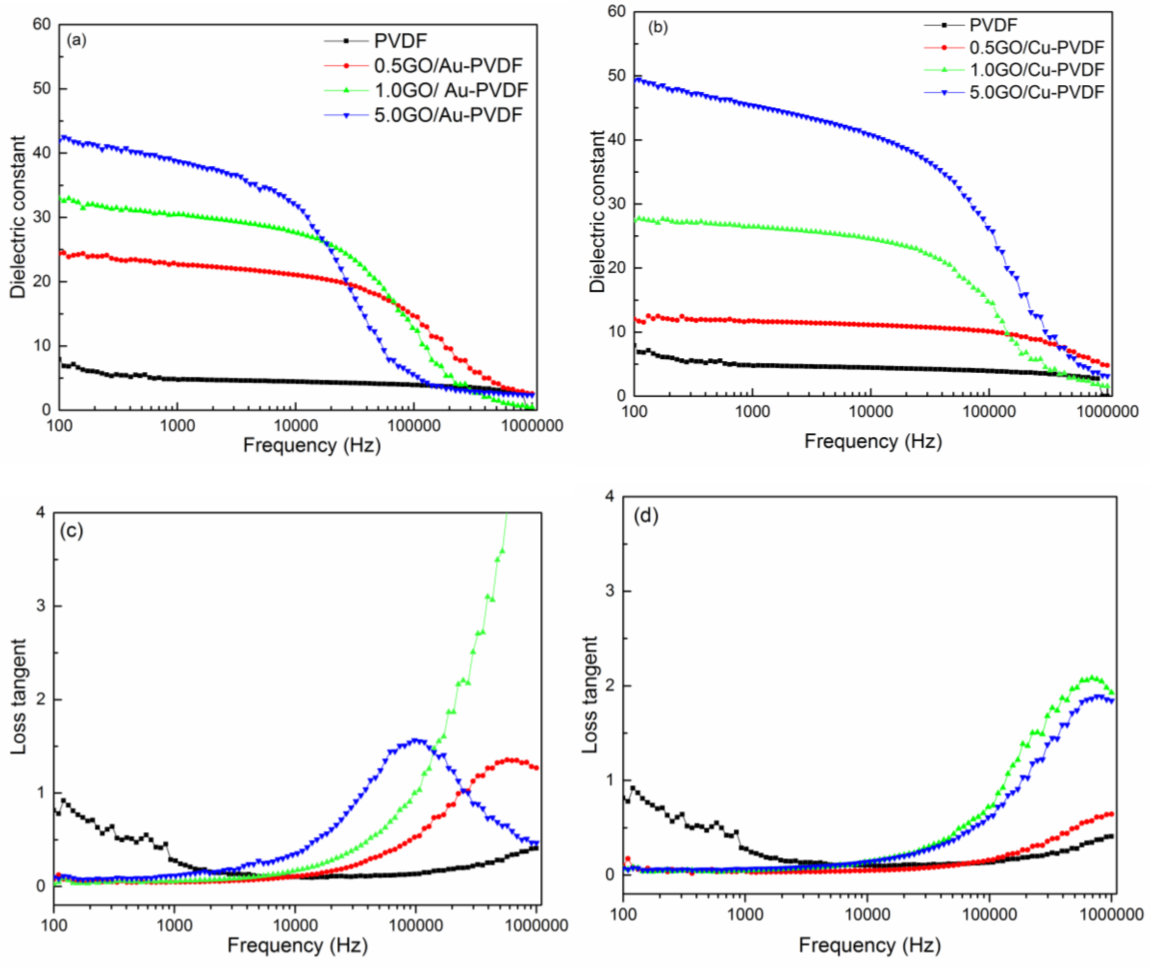

Figure 6.11. Frequency dependence of dielectric constant and dielectric loss tangent (tan δ) of pure PVDF and nanocomposites with various amount of a,c) GO/Au and b, d) GO/Cu.

In general, an increment of relative permittivity may occur for several reasons. One of them is the formation of a network of micro-capacitors in the nanocomposite due to the presence of nanofillers. This mechanisms has been reported by He et al. in a study on the effect of expanded graphite nanoparticles (xGnP) on the dielectric permittivity of PVDF nanocomposites [200]. In fact, when GO/Au and GO/Cu nanofillers are incorporated into the PVDF matrix, they could play the role of micro-capacitors thus resulting in an overall increase of the dielectric constant of the nanocomposites with respect of that of neat PVDF. Another possible mechanisms responsible for the observed increase of the dielectric constant in nanocomposites could be the Maxwell–Wagner–Sillars (MWS) polarization effect, often observed in heterogeneous systems [201, 202]. In fact, the MWS effect, which is associated to an entrapment of free charges at an interface between two heterogeneous materials, can significantly enhance the permittivity. This effect has been frequently observed in composites filled with a conductive filler and it has been previously reported also for PVDF nanocomposites filled with carbon nano- fibers [203], graphene [204, 205] and nano silver-anchored reduced graphene oxide sheets [206]. The MWS effect is generally characterized by a frequency dependence of the dielectric constant, particularly in the low-frequency range where interfacial polarization effects are more intense [200]. In addition, polymorphism of PVDF may also play a remarkable effect on the dielectric constant. In fact, it is well known that b- and g-phases of PVDF manifest the largest spontaneous polarization [207]. Therefore, part of the observed effects could be attributed to the ability of GO/Au and GO/Cu nanofillers to promote the formation of electroactive phases in PVDF, as discussed in previous sections. **Figure 6.11c and d** shows the changes of dielectric loss of neat PVDF and PVDF nanocomposites with frequency in a range between 10^2 and 10^6 Hz at room temperature. The dielectric loss is a measurement of the energy dissipation from the movement or rotation of the molecules in the alternating electric field. It is interesting to observe how for all the investigated nanocomposites the dielectric losses are suppressed in the low frequency range with respect to neat PVDF. Thus, these nanocomposites show relatively high dielectric constant with relatively low loss at low frequency range (below 10 KHz) which is basically the requirement of a material for its usage in devices for the energy storage.

References

[1] S.C. Jana and S. Jain, *Dispersion of nanofillers in high performance polymers using reactive solvents as processing aids*, Polymer, **2001**. 42(16): p. 6897-6905.

[2] K.K. Kar, S. Rana, and J. Pandey, *Handbook of polymer nanocomposites. Processing, performance and application*, **2015**: Springer.

[3] M. Šupová, G.S. Martynková, and K. Barabaszová, *Effect of Nanofillers Dispersion in Polymer Matrices: A Review*, Science of Advanced Materials, **2011**. 3(1): p. 1-25.

[4] S. Wu, R.B. Ladani, J. Zhang, A.J. Kinloch, Z. Zhao, J. Ma, *et al.*, *Epoxy nanocomposites containing magnetite-carbon nanofibers aligned using a weak magnetic field*, Polymer, **2015**. 68(p. 25-34.

[5] M. Monti, M. Natali, L. Torre, and J.M. Kenny, *The alignment of single walled carbon nanotubes in an epoxy resin by applying a DC electric field*, Carbon, **2012**. 50(7): p. 2453-2464.

[6] C. Ma, W. Zhang, Y.F. Zhu, L.J. Ji, R.P. Zhang, N. Koratkar, *et al.*, *Alignment and dispersion of functionalized carbon nanotubes in polymer composites induced by an electric field*, Carbon, **2008**. 46(4): p. 706-710.

[7] R.B. Ladani, S. Wu, A.J. Kinloch, K. Ghorbani, J. Zhang, A.P. Mouritz, *et al.*, *Improving the toughness and electrical conductivity of epoxy nanocomposites by using aligned carbon nanofibres*, Composites Science and Technology, **2015**. 117(p. 146-158.

[8] H. Yan, Y. Tang, W. Long, and Y. Li, *Enhanced thermal conductivity in polymer composites with aligned graphene nanosheets*, Journal of Materials Science, **2014**. 49(15): p. 5256-5264.

[9] J.G. Park, Q. Cheng, J. Lu, J. Bao, S. Li, Y. Tian, *et al.*, *Thermal conductivity of MWCNT/epoxy composites: The effects of length, alignment and functionalization*, Carbon, **2012**. 50(6): p. 2083-2090.

[10] Y.F. Zhu, C. Ma, W. Zhang, R.P. Zhang, N. Koratkar, and J. Liang, *Alignment of multiwalled carbon nanotubes in bulk epoxy composites via electric field*, Journal of Applied Physics, **2009**. 105(5): p. 054319.

[11] M.K. Schwarz, W. Bauhofer, and K. Schulte, *Alternating electric field induced agglomeration of carbon black filled resins*, Polymer, **2002**. 43(10): p. 3079-3082.

[12] C.A. Martin, J.K.W. Sandler, A.H. Windle, M.K. Schwarz, W. Bauhofer, K. Schulte*, et al.*, *Electric field-induced aligned multi-wall carbon nanotube networks in epoxy composites*, Polymer*,* **2005**. 46(3): p. 877-886.

[13] S.H. Tolbert, A. Firouzi, G.D. Stucky, and B.F. Chmelka, *Magnetic Field Alignment of Ordered Silicate-Surfactant Composites and Mesoporous Silica*, Science*,* **1997**. 278(5336): p. 264.

[14] B.W. Steinert and D.R. Dean, *Magnetic field alignment and electrical properties of solution cast PET–carbon nanotube composite films*, Polymer*,* **2009**. 50(3): p. 898-904.

[15] M. Abdalla, D. Dean, M. Theodore, J. Fielding, E. Nyairo, and G. Price, *Magnetically processed carbon nanotube/epoxy nanocomposites: Morphology, thermal, and mechanical properties*, Polymer*,* **2010**. 51(7): p. 1614-1620.

[16] H. Mahfuz, S. Zainuddin, M.R. Parker, T. Al-Saadi, V.K. Rangari, and S. Jeelani, *Reinforcement of SC-15 epoxy with CNT/CNF under high magnetic field: an investigation of mechanical and thermal response*, Journal of Materials Science*,* **2009**. 44(4): p. 1113-1120.

[17] D. Fragouli, A. Das, C. Innocenti, Y. Guttikonda, S. Rahman, L. Liu*, et al.*, *Polymeric Films with Electric and Magnetic Anisotropy Due to Magnetically Assembled Functional Nanofibers*, ACS Applied Materials & Interfaces*,* **2014**. 6(6): p. 4535-4541.

[18] E. Camponeschi, R. Vance, M. Al-Haik, H. Garmestani, and R. Tannenbaum, *Properties of carbon nanotube–polymer composites aligned in a magnetic field*, Carbon*,* **2007**. 45(10): p. 2037-2046.

[19] M. Bhattacharya, *Polymer Nanocomposites—A Comparison between Carbon Nanotubes, Graphene, and Clay as Nanofillers*, Materials*,* **2016**. 9(4): p. 262.

[20] M. Zoghi, *The International Handbook of FRP Composites in Civil Engineering*, **2013**: CRC Press.

[21] J.C. Gerdeen and R.A. Rorrer, *Engineering design with polymers and composites*, **2011** vol. 30: CRC Press.

[22] F.C. Campbell, *Structural composite materials*, **2010**: ASM international.

[23] P.K. Mallick, *Fiber-reinforced composites: materials, manufacturing, and design*, **2007**: CRC press.

[24] P. Herrera-Franco and L. Drzal, *Comparison of methods for the measurement of fibre/matrix adhesion in composites*, Composites*,* **1992**. 23(1): p. 2-27.

[25] H. Ishida, *Controlled Interphases in Composite Materials: Proceedings of the Third International Conference on Composite Interfaces (ICCI-III) Held on May 21–24, 1990 in Cleveland, Ohio, USA*, **2012**: Springer Science & Business Media.

[26] E. Sideridis, *Thermal expansion coefficients of fiber composites defined by the concept of the interphase*, Composites science and technology, **1994**. 51(3): p. 301-317.

[27] J. Karger-Kocsis, H. Mahmood, and A. Pegoretti, *Recent advances in fiber/matrix interphase engineering for polymer composites*, Progress in Materials Science, **2015**. 73(p. 1-43.

[28] W.T.Y. Tze, D.J. Gardner, C.P. Tripp, and S.C. O'Neill, *Cellulose fiber/polymer adhesion: effects of fiber/matrix interfacial chemistry on the micromechanics of the interphase*, Journal of Adhesion Science and Technology, **2006**. 20(15): p. 1649-1668.

[29] A. Kelly and W.R. Tyson, *Tensile properties of fibre-reinforced metals: Copper/tungsten and copper/molybdenum*, Journal of the Mechanics and Physics of Solids, **1965**. 13(6): p. 329-350.

[30] P.J. Herrera-Franco and L.T. Drzal, *Comparison of methods for the measurement of fibre/matrix adhesion in composites*, Composites, **1992**. 23(1): p. 2-27.

[31] L.Z. Linganiso and R.D. Anandjiwala, *4 - Fibre-reinforced laminates in aerospace engineering*, in *Advanced Composite Materials for Aerospace Engineering*. **2016**: Woodhead Publishing. p. 101-127.

[32] F.L. Shan, Y.Z. Gu, M. Li, Y.N. Liu, and Z.G. Zhang, *Effect of deposited carbon nanotubes on interlaminar properties of carbon fiber-reinforced epoxy composites using a developed spraying processing*, Polymer Composites, **2013**. 34(1): p. 41-50.

[33] X. Zhang, X. Fan, C. Yan, H. Li, Y. Zhu, X. Li, *et al.*, *Interfacial Microstructure and Properties of Carbon Fiber Composites Modified with Graphene Oxide*, ACS Applied Materials & Interfaces, **2012**. 4(3): p. 1543-1552.

[34] V.C.S. Chandrasekaran, S.G. Advani, and M.H. Santare, *Influence of resin properties on interlaminar shear strength of glass/epoxy/MWNT hybrid composites*, Composites Part A: Applied Science and Manufacturing, **2011**. 42(8): p. 1007-1016.

[35] A.K. Pathak, M. Borah, A. Gupta, T. Yokozeki, and S.R. Dhakate, *Improved mechanical properties of carbon fiber/graphene oxide-epoxy hybrid composites*, Composites Science and Technology, **2016**. 135(p. 28-38.

[36] A.S. Paipetis and V. Kostopoulos, *Carbon Nanotubes for Novel Hybrid Structural Composites with Enhanced Damage Tolerance and Self-Sensing/Actuating Abilities*, in

Carbon Nanotube Enhanced Aerospace Composite Materials: A New Generation of Multifunctional Hybrid Structural Composites. **2013**. Dordrecht: Springer Netherlands. p. 1-20.

[37] T. Gibson, S. Putthanarat, J.C. Fielding, A. Drain, K. Will, and M. Stoffel, *Conductive nanocomposites: focus on lightning strike protection*, in *Proc int SAMPE tech conf and exhibition–from art to science: advancing mater and proc eng*, Conference 2007 Location.

[38] W. Qin, F. Vautard, L.T. Drzal, and J. Yu, *Mechanical and electrical properties of carbon fiber composites with incorporation of graphene nanoplatelets at the fiber–matrix interphase*, Composites Part B: Engineering, **2015**. 69(p. 335-341.

[39] C. Zhi, Y. Bando, T. Terao, C. Tang, H. Kuwahara, and D. Golberg, *Towards Thermoconductive, Electrically Insulating Polymeric Composites with Boron Nitride Nanotubes as Fillers*, Advanced Functional Materials, **2009**. 19(12): p. 1857-1862.

[40] X. Huang, P. Jiang, and T. Tanaka, *A review of dielectric polymer composites with high thermal conductivity*, IEEE Electrical Insulation Magazine, **2011**. 27(4): p. 8-16.

[41] N. Shenogina, S. Shenogin, L. Xue, and P. Keblinski, *On the lack of thermal percolation in carbon nanotube composites*, Applied Physics Letters, **2005**. 87(13): p. 133106.

[42] C.-C. Teng, C.-C.M. Ma, K.-C. Chiou, T.-M. Lee, and Y.-F. Shih, *Synergetic effect of hybrid boron nitride and multi-walled carbon nanotubes on the thermal conductivity of epoxy composites*, Materials Chemistry and Physics, **2011**. 126(3): p. 722-728.

[43] X. Zhao and L. Ye, *Preparation, structure, and property of polyoxymethylene/carbon nanotubes thermal conducive composites*, Journal of Polymer Science Part B: Polymer Physics, **2010**. 48(8): p. 905-912.

[44] K.C. Yung and H. Liem, *Enhanced thermal conductivity of boron nitride epoxy-matrix composite through multi-modal particle size mixing*, Journal of Applied Polymer Science, **2007**. 106(6): p. 3587-3591.

[45] S.-Y. Yang, C.-C.M. Ma, C.-C. Teng, Y.-W. Huang, S.-H. Liao, Y.-L. Huang, *et al.*, *Effect of functionalized carbon nanotubes on the thermal conductivity of epoxy composites*, Carbon, **2010**. 48(3): p. 592-603.

[46] K. Yang and M. Gu, *Enhanced thermal conductivity of epoxy nanocomposites filled with hybrid filler system of triethylenetetramine-functionalized multi-walled carbon*

nanotube/silane-modified nano-sized silicon carbide, Composites Part A: Applied Science and Manufacturing, **2010**. 41(2): p. 215-221.

[47] G.T. Pham, Y.-B. Park, Z. Liang, C. Zhang, and B. Wang, *Processing and modeling of conductive thermoplastic/carbon nanotube films for strain sensing*, Composites Part B: Engineering, **2008**. 39(1): p. 209-216.

[48] N. Hu, Y. Karube, C. Yan, Z. Masuda, and H. Fukunaga, *Tunneling effect in a polymer/carbon nanotube nanocomposite strain sensor*, Acta Materialia, **2008**. 56(13): p. 2929-2936.

[49] Z. Li, P. Dharap, S. Nagarajaiah, E.V. Barrera, and J.D. Kim, *Carbon Nanotube Film Sensors*, Advanced Materials, **2004**. 16(7): p. 640-643.

[50] K. Inpil, J.S. Mark, H.K. Jay, S. Vesselin, and S. Donglu, *A carbon nanotube strain sensor for structural health monitoring*, Smart Materials and Structures, **2006**. 15(3): p. 737.

[51] S. Blazewicz, B. Patalita, and P. Touzain, *Study of piezoresistance effect in carbon fibers*, Carbon, **1997**. 35(10): p. 1613-1618.

[52] J.H. Kang, C. Park, J.A. Scholl, A.H. Brazin, N.M. Holloway, J.W. High, *et al.*, *Piezoresistive characteristics of single wall carbon nanotube/polyimide nanocomposites*, Journal of Polymer Science Part B: Polymer Physics, **2009**. 47(10): p. 994-1003.

[53] S.-H. Bae, Y. Lee, B.K. Sharma, H.-J. Lee, J.-H. Kim, and J.-H. Ahn, *Graphene-based transparent strain sensor*, Carbon, **2013**. 51(p. 236-242.

[54] C. Yan, J. Wang, W. Kang, M. Cui, X. Wang, C.Y. Foo, *et al.*, *Highly Stretchable Piezoresistive Graphene–Nanocellulose Nanopaper for Strain Sensors*, Advanced Materials, **2014**. 26(13): p. 2022-2027.

[55] C. Stampfer, A. Jungen, R. Linderman, D. Obergfell, S. Roth, and C. Hierold, *Nano-Electromechanical Displacement Sensing Based on Single-Walled Carbon Nanotubes*, Nano Letters, **2006**. 6(7): p. 1449-1453.

[56] P. Michalczyk and M. Bramoulle, *Ultimate properties of the polypropylene film for energy storage capacitors*, IEEE Transactions on Magnetics, **2003**. 39(1): p. 362-365.

[57] C.J. Dias and D.K. Das-Gupta, *Inorganic ceramic/polymer ferroelectric composite electrets*, IEEE Transactions on Dielectrics and Electrical Insulation, **1996**. 3(5): p. 706-734.

[58] E. Reichmanis, H. Katz, C. Kloc, and A. Maliakal, *Plastic electronic devices: From materials design to device applications*, Bell Labs Technical Journal, **2005**. 10(3): p. 87-105.

[59] S. Stankovich, D.A. Dikin, G.H.B. Dommett, K.M. Kohlhaas, E.J. Zimney, E.A. Stach, *et al.*, *Graphene-based composite materials*, Nature, **2006**. 442(7100): p. 282-286.

[60] T. Ramanathan, A.A. Abdala, S. Stankovich, D.A. Dikin, M. Herrera-Alonso, R.D. Piner, *et al.*, *Functionalized graphene sheets for polymer nanocomposites*, Nat Nanotechnol, **2008**. 3(6): p. 327-31.

[61] H. Kim, A.A. Abdala, and C.W. Macosko, *Graphene/Polymer Nanocomposites*, Macromolecules, **2010**. 43(16): p. 6515-6530.

[62] N. Yousefi, X. Sun, X. Lin, X. Shen, J. Jia, B. Zhang, *et al.*, *Highly Aligned Graphene/Polymer Nanocomposites with Excellent Dielectric Properties for High-Performance Electromagnetic Interference Shielding*, Advanced Materials, **2014**. 26(31): p. 5480-5487.

[63] K.S. Novoselov, A.K. Geim, S.V. Morozov, D. Jiang, Y. Zhang, S.V. Dubonos, *et al.*, *Electric Field Effect in Atomically Thin Carbon Films*, Science, **2004**. 306(5696): p. 666-669.

[64] A.K. Geim and K.S. Novoselov, *The rise of graphene*, Nat Mater, **2007**. 6(3): p. 183-191.

[65] C. Lee, X. Wei, J.W. Kysar, and J. Hone, *Measurement of the Elastic Properties and Intrinsic Strength of Monolayer Graphene*, Science, **2008**. 321(5887): p. 385-388.

[66] S.V. Morozov, K.S. Novoselov, M.I. Katsnelson, F. Schedin, D.C. Elias, J.A. Jaszczak, *et al.*, *Giant Intrinsic Carrier Mobilities in Graphene and Its Bilayer*, Physical Review Letters, **2008**. 100(1): p. 016602.

[67] A.A. Balandin, S. Ghosh, W. Bao, I. Calizo, D. Teweldebrhan, F. Miao, *et al.*, *Superior thermal conductivity of single-layer graphene*, Nano letters, **2008**. 8(3): p. 902-907.

[68] P.R. Wallace, *The Band Theory of Graphite*, Physical Review, **1947**. 71(9): p. 622-634.

[69] J.C. Slonczewski and P.R. Weiss, *Band Structure of Graphite*, Physical Review, **1958**. 109(2): p. 272-279.

[70] A.F. Young and P. Kim, *Quantum interference and Klein tunnelling in graphene heterojunctions*, Nat Phys, **2009**. 5(3): p. 222-226.

[71] Y. Wang, D. Wong, A.V. Shytov, V.W. Brar, S. Choi, Q. Wu, *et al.*, *Observing Atomic Collapse Resonances in Artificial Nuclei on Graphene*, Science, **2013**. 340(6133): p. 734-737.

[72] A. De Martino, D. Klöpfer, D. Matrasulov, and R. Egger, *Electric-Dipole-Induced Universality for Dirac Fermions in Graphene*, Physical Review Letters, **2014**. 112(18): p. 186603.

[73] Y. Zhang, Y.-W. Tan, H.L. Stormer, and P. Kim, *Experimental observation of the quantum Hall effect and Berry's phase in graphene*, Nature, **2005**. 438(7065): p. 201-204.

[74] K.S. Novoselov, A.K. Geim, S.V. Morozov, D. Jiang, M.I. Katsnelson, I.V. Grigorieva, *et al.*, *Two-dimensional gas of massless Dirac fermions in graphene*, Nature, **2005**. 438(7065): p. 197-200.

[75] Y.-W. Son, M.L. Cohen, and S.G. Louie, *Energy Gaps in Graphene Nanoribbons*, Physical Review Letters, **2006**. 97(21): p. 216803.

[76] H. Liu, S. Ryu, Z. Chen, M.L. Steigerwald, C. Nuckolls, and L.E. Brus, *Photochemical Reactivity of Graphene*, Journal of the American Chemical Society, **2009**. 131(47): p. 17099-17101.

[77] D.R. Dreyer, S. Park, C.W. Bielawski, and R.S. Ruoff, *The chemistry of graphene oxide*, Chem Soc Rev, **2010**. 39(1): p. 228-40.

[78] P. Lange, M. Dorn, N. Severin, D.A. Vanden Bout, and J.P. Rabe, *Single- and Double-Layer Graphenes as Ultrabarriers for Fluorescent Polymer Films*, The Journal of Physical Chemistry C, **2011**. 115(46): p. 23057-23061.

[79] M.H. Jung and M.J. Chu, *Comparative experiments of graphene covalently and physically binding CdSe quantum dots to enhance the electron transport in flexible photovoltaic devices*, Nanoscale, **2014**. 6(15): p. 9241-9.

[80] M.Z. Iqbal, S. Siddique, M.W. Iqbal, and J. Eom, *Formation of p-n junction with stable p-doping in graphene field effect transistors using deep UV irradiation*, Journal of Materials Chemistry C, **2013**. 1(18): p. 3078-3083.

[81] K.S. Novoselov, V.I. Falko, L. Colombo, P.R. Gellert, M.G. Schwab, and K. Kim, *A roadmap for graphene*, Nature, **2012**. 490(7419): p. 192-200.

[82] F. Schwierz, *Graphene transistors*, Nat Nano, **2010**. 5(7): p. 487-496.

[83] P. Avouris, *Graphene: electronic and photonic properties and devices*, Nano letters, **2010**. 10(11): p. 4285-4294.

[84] M. Pumera, *Graphene-based nanomaterials and their electrochemistry*, Chemical Society Reviews, **2010**. 39(11): p. 4146-4157.

[85] U. Khan, A. O'Neill, H. Porwal, P. May, K. Nawaz, and J.N. Coleman, *Size selection of dispersed, exfoliated graphene flakes by controlled centrifugation*, Carbon, **2012**. 50(2): p. 470-475.

[86] K.R. Paton, E. Varrla, C. Backes, R.J. Smith, U. Khan, A. O'Neill, *et al.*, *Scalable production of large quantities of defect-free few-layer graphene by shear exfoliation in liquids*, Nat Mater, **2014**. 13(6): p. 624-630.

[87] M. Yi and Z. Shen, *Kitchen blender for producing high-quality few-layer graphene*, Carbon, **2014**. 78(p. 622-626.

[88] M.Y. null, Z.S. null, and J.Z. null, *A fluid dynamics route for producing graphene and its analogues*, Chinese Science Bulletin, **2014**. 59(16): p. 1794.

[89] S. Zhigang, L. Jinzhi, Y. Min, Z. Xiaojing, and M. Shulin, *Preparation of graphene by jet cavitation*, Nanotechnology, **2011**. 22(36): p. 365306.

[90] L. Liu, Z. Shen, M. Yi, X. Zhang, and S. Ma, *A green, rapid and size-controlled production of high-quality graphene sheets by hydrodynamic forces*, RSC Advances, **2014**. 4(69): p. 36464-36470.

[91] W.A. de Heer, C. Berger, X. Wu, P.N. First, E.H. Conrad, X. Li, *et al.*, *Epitaxial graphene*, Solid State Communications, **2007**. 143(1–2): p. 92-100.

[92] K.V. Emtsev, A. Bostwick, K. Horn, J. Jobst, G.L. Kellogg, L. Ley, *et al.*, *Towards wafer-size graphene layers by atmospheric pressure graphitization of silicon carbide*, Nat Mater, **2009**. 8(3): p. 203-207.

[93] H. Huang, W. Chen, S. Chen, and A.T. Wee, *Bottom-up growth of epitaxial graphene on 6H-SiC(0001)*, ACS Nano, **2008**. 2(12): p. 2513-8.

[94] X. Li, W. Cai, L. Colombo, and R.S. Ruoff, *Evolution of Graphene Growth on Ni and Cu by Carbon Isotope Labeling*, Nano Letters, **2009**. 9(12): p. 4268-4272.

[95] J.N. Coleman, *Liquid Exfoliation of Defect-Free Graphene*, Accounts of Chemical Research, **2013**. 46(1): p. 14-22.

[96] W.C. Wang, Y. Wang, Y.H. Gao, and Y.P. Zhao, *Control of number of graphene layers using ultrasound in supercritical CO2 and their application in lithium-ion batteries*, Journal of Supercritical Fluids, **2014**. 85(p. 95-101.

[97] Y. Meng, F. Su, and Y. Chen, *Synthesis of nano-Cu/graphene oxide composites by supercritical CO2-assisted deposition as a novel material for reducing friction and wear*, Chemical Engineering Journal, **2015**. 281(p. 11-19.

[98] H.S. Sim, T.A. Kim, K.H. Lee, and M. Park, *Preparation of graphene nanosheets through repeated supercritical carbon dioxide process*, Materials Letters, **2012**. 89(p. 343-346.

[99] L. Li, X. Zheng, J. Wang, Q. Sun, and Q. Xu, *Solvent-exfoliated and functionalized graphene with assistance of supercritical carbon dioxide*, ACS Sustainable Chemistry & Engineering, **2012**. 1(1): p. 144-151.

[100] L. Li, J. Xu, G. Li, X. Jia, Y. Li, F. Yang, *et al.*, *Preparation of graphene nanosheets by shear-assisted supercritical CO 2 exfoliation*, Chemical Engineering Journal, **2016**. 284(p. 78-84.

[101] D. Chen, H. Feng, and J. Li, *Graphene oxide: preparation, functionalization, and electrochemical applications*, Chemical reviews, **2012**. 112(11): p. 6027-6053.

[102] B.C. Brodie, *On the Atomic Weight of Graphite*, Philosophical Transactions of the Royal Society of London, **1859**. 149(p. 249-259.

[103] L. Staudenmaier, *Verfahren zur Darstellung der Graphitsäure*, Berichte der deutschen chemischen Gesellschaft, **1898**. 31(2): p. 1481-1487.

[104] W.S. Hummers Jr and R.E. Offeman, *Preparation of graphitic oxide*, Journal of the American Chemical Society, **1958**. 80(6): p. 1339-1339.

[105] D.R. Dreyer, S. Park, C.W. Bielawski, and R.S. Ruoff, *The chemistry of graphene oxide*, Chemical Society Reviews, **2010**. 39(1): p. 228-240.

[106] M.J. McAllister, J.-L. Li, D.H. Adamson, H.C. Schniepp, A.A. Abdala, J. Liu, *et al.*, *Single sheet functionalized graphene by oxidation and thermal expansion of graphite*, Chemistry of materials, **2007**. 19(18): p. 4396-4404.

[107] S. Park, D.A. Dikin, S.T. Nguyen, and R.S. Ruoff, *Graphene oxide sheets chemically cross-linked by polyallylamine*, The Journal of Physical Chemistry C, **2009**. 113(36): p. 15801-15804.

[108] H.C. Schniepp, J.-L. Li, M.J. McAllister, H. Sai, M. Herrera-Alonso, D.H. Adamson, *et al.*, *Functionalized single graphene sheets derived from splitting graphite oxide*, The Journal of Physical Chemistry B, **2006**. 110(17): p. 8535-8539.

[109] L.M. Veca, F. Lu, M.J. Meziani, L. Cao, P. Zhang, G. Qi, *et al.*, *Polymer functionalization and solubilization of carbon nanosheets*, Chemical Communications, **2009**. 18): p. 2565-2567.

[110] Y. Yang, J. Wang, J. Zhang, J. Liu, X. Yang, and H. Zhao, *Exfoliated graphite oxide decorated by PDMAEMA chains and polymer particles*, Langmuir, **2009**. 25(19): p. 11808-11814.

[111] Z.-B. Liu, Y.-F. Xu, X.-Y. Zhang, X.-L. Zhang, Y.-S. Chen, and J.-G. Tian, *Porphyrin and fullerene covalently functionalized graphene hybrid materials with large nonlinear optical properties*, The Journal of Physical Chemistry B, **2009**. 113(29): p. 9681-9686.

[112] X. Zhang, Y. Huang, Y. Wang, Y. Ma, Z. Liu, and Y. Chen, *Synthesis and characterization of a graphene–C60 hybrid material*, Carbon, **2009**. 47(1): p. 334-337.

[113] Z. Liu, J.T. Robinson, X. Sun, and H. Dai, *PEGylated nanographene oxide for delivery of water-insoluble cancer drugs*, Journal of the American Chemical Society, **2008**. 130(33): p. 10876-10877.

[114] N. Mohanty and V. Berry, *Graphene-based single-bacterium resolution biodevice and DNA transistor: interfacing graphene derivatives with nanoscale and microscale biocomponents*, Nano letters, **2008**. 8(12): p. 4469-4476.

[115] R.K. Layek and A.K. Nandi, *A review on synthesis and properties of polymer functionalized graphene*, Polymer, **2013**. 54(19): p. 5087-5103.

[116] L. Gomez De Arco, Y. Zhang, C.W. Schlenker, K. Ryu, M.E. Thompson, and C. Zhou, *Continuous, highly flexible, and transparent graphene films by chemical vapor deposition for organic photovoltaics*, ACS Nano, **2010**. 4(5): p. 2865-73.

[117] L. Valentini, M. Cardinali, S. Bittolo Bon, D. Bagnis, R. Verdejo, M.A. Lopez-Manchado, *et al.*, *Use of butylamine modified graphene sheets in polymer solar cells*, Journal of Materials Chemistry, **2010**. 20(5): p. 995-1000.

[118] S.-S. Li, K.-H. Tu, C.-C. Lin, C.-W. Chen, and M. Chhowalla, *Solution-processable graphene oxide as an efficient hole transport layer in polymer solar cells*, ACS nano, **2010**. 4(6): p. 3169-3174.

[119] P. Blake, P.D. Brimicombe, R.R. Nair, T.J. Booth, D. Jiang, F. Schedin, *et al.*, *Graphene-based liquid crystal device*, Nano letters, **2008**. 8(6): p. 1704-1708.

[120] J. Wu, H.A. Becerril, Z. Bao, Z. Liu, Y. Chen, and P. Peumans, *Organic solar cells with solution-processed graphene transparent electrodes*, Applied Physics Letters, **2008**. 92(26): p. 263302.

[121] W. Hong, Y. Xu, G. Lu, C. Li, and G. Shi, *Transparent graphene/PEDOT–PSS composite films as counter electrodes of dye-sensitized solar cells*, Electrochemistry Communications, **2008**. 10(10): p. 1555-1558.

[122] G. Eda, H.E. Unalan, N. Rupesinghe, G.A.J. Amaratunga, and M. Chhowalla, *Field emission from graphene based composite thin films*, Applied Physics Letters, **2008**. 93(23): p. 233502.

[123] V.P. Verma, S. Das, I. Lahiri, and W. Choi, *Large-area graphene on polymer film for flexible and transparent anode in field emission device*, Applied Physics Letters, **2010**. 96(20): p. 203108.

[124] S. Bae, H. Kim, Y. Lee, X. Xu, J.-S. Park, Y. Zheng, *et al.*, *Roll-to-roll production of 30-inch graphene films for transparent electrodes*, Nat Nano, **2010**. 5(8): p. 574-578.

[125] Y. Lee, S. Bae, H. Jang, S. Jang, S.-E. Zhu, S.H. Sim, *et al.*, *Wafer-scale synthesis and transfer of graphene films*, Nano letters, **2010**. 10(2): p. 490-493.

[126] H.-B. Zhang, Q. Yan, W.-G. Zheng, Z. He, and Z.-Z. Yu, *Tough graphene− polymer microcellular foams for electromagnetic interference shielding*, ACS applied materials & interfaces, **2011**. 3(3): p. 918-924.

[127] Z. Chen, C. Xu, C. Ma, W. Ren, and H.-M. Cheng, *Lightweight and Flexible Graphene Foam Composites for High-Performance Electromagnetic Interference Shielding*, Advanced Materials, **2013**. 25(9): p. 1296-1300.

[128] J. Liang, Y. Wang, Y. Huang, Y. Ma, Z. Liu, J. Cai, *et al.*, *Electromagnetic interference shielding of graphene/epoxy composites*, Carbon, **2009**. 47(3): p. 922-925.

[129] A.R. Boccaccini and I. Zhitomirsky, *Application of electrophoretic and electrolytic deposition techniques in ceramics processing*, Current Opinion in Solid State & Materials Science, **2002**. 6(3): p. 251-260.

[130] O.O.V.d.B. and and L.J. Vandeperre, *ELECTROPHORETIC DEPOSITION OF MATERIALS*, Annual Review of Materials Science, **1999**. 29(1): p. 327-352.

[131] P. Sarkar and P.S. Nicholson, *Electrophoretic Deposition (EPD): Mechanisms, Kinetics, and Application to Ceramics*, Journal of the American Ceramic Society, **1996**. 79(8): p. 1987-2002.

[132] N. Sato, M. Kawachi, K. Noto, N. Yoshimoto, and M. Yoshizawa, *Effect of particle size reduction on crack formation in electrophoretically deposited YBCO films*, Physica C: Superconductivity, **2001**. 357–360, Part 2(p. 1019-1022.

[133] B. Ferrari and R. Moreno, *The conductivity of aqueous Al2O3 slips for electrophoretic deposition*, Materials Letters, **1996**. 28(4-6): p. 353-355.

[134] N.S. Waluyo, R.-H. Song, S.-B. Lee, T.-H. Lim, S.-J. Park, and J.-W. Lee, *Electrophoretically Deposited LaNi0.6Fe0.4O3 Perovskite Coatings on Metallic Interconnects for Solid Oxide Fuel Cells*, Journal of The Electrochemical Society, **2016**. 163(10): p. F1245-F1250.

[135] L. Besra and M. Liu, *A review on fundamentals and applications of electrophoretic deposition (EPD)*, Progress in Materials Science, **2007**. 52(1): p. 1-61.

[136] H.G. Kruger, A. Knote, U. Schindler, H. Kern, and A.R. Boccaccini, *Composite ceramic-metal coatings by means of combined electrophoretic deposition and galvanic methods*, Journal of Materials Science, **2004**. 39(3): p. 839-844.

[137] M. Zarbov, I. Schuster, and L. Gal-Or, *Methodology for selection of charging agents for electrophoretic deposition of ceramic particles*, Journal of Materials Science, **2004**. 39(3): p. 813-817.

[138] Y.-C. Wang, I.-C. Leu, and M.-H. Hon, *Kinetics of Electrophoretic Deposition for Nanocrystalline Zinc Oxide Coatings*, Journal of the American Ceramic Society, **2004**. 87(1): p. 84-88.

[139] R.N. Basu, C.A. Randall, and M.J. Mayo, *Fabrication of Dense Zirconia Electrolyte Films for Tubular Solid Oxide Fuel Cells by Electrophoretic Deposition*, Journal of the American Ceramic Society, **2001**. 84(1): p. 33-40.

[140] P. Sarkar, D. De, and H. Rho, *Synthesis and microstructural manipulation of ceramics by electrophoretic deposition*, Journal of Materials Science, **2004**. 39(3): p. 819-823.

[141] H.C. Hamaker, *Formation of a deposit by electrophoresis*, Transactions of the Faraday Society, **1940**. 35(0): p. 279-287.

[142] F. Grillon, D. Fayeulle, and M. Jeandin, *Quantitative image analysis of electrophoretic coatings*, Journal of Materials Science Letters, **1992**. 11(5): p. 272-275.

[143] C. Du, D. Heldbrant, and N. Pan, *Preparation and preliminary property study of carbon nanotubes films by electrophoretic deposition*, Materials Letters, **2002**. 57(2): p. 434-438.

[144] C. Du, D. Heldebrant, and N. Pan, *Preparation of carbon nanotubes composite sheet using electrophoretic deposition process*, Journal of Materials Science Letters, **2002**. 21(7): p. 565-568.

[145] B.J.C. Thomas, A.R. Boccaccini, and M.S.P. Shaffer, *Multi-Walled Carbon Nanotube Coatings Using Electrophoretic Deposition (EPD)*, Journal of the American Ceramic Society, **2005**. 88(4): p. 980-982.

[146] Y.W. Jin, J.E. Jung, Y.J. Park, J.H. Choi, D.S. Jung, H.W. Lee, *et al.*, *Triode-type field emission array using carbon nanotubes and a conducting polymer composite prepared by electrochemical polymerization*, Journal of Applied Physics, **2002**. 92(2): p. 1065-1068.

[147] I. Singh, C. Kaya, M.S.P. Shaffer, B.C. Thomas, and A.R. Boccaccini, *Bioactive ceramic coatings containing carbon nanotubes on metallic substrates by electrophoretic deposition*, Journal of Materials Science, **2006**. 41(24): p. 8144-8151.

[148] Z. Wu, Z. Chen, X. Du, J.M. Logan, J. Sippel, M. Nikolou, *et al.*, *Transparent, Conductive Carbon Nanotube Films*, Science, **2004**. 305(5688): p. 1273-1276.

[149] W.B. Choi, Y.W. Jin, H.Y. Kim, S.J. Lee, M.J. Yun, J.H. Kang, *et al.*, *Electrophoresis deposition of carbon nanotubes for triode-type field emission display*, Applied Physics Letters, **2001**. 78(11): p. 1547-1549.

[150] Y. Nakayama and S. Akita, *Field-emission device with carbon nanotubes for a flat panel display*, Synthetic Metals, **2001**. 117(1–3): p. 207-210.

[151] R. Colorado and A.R. Barron, *Silica-coated single-walled nanotubes: nanostructure formation*, Chemistry of materials, **2004**. 16(14): p. 2691-2693.

[152] G. Girishkumar, K. Vinodgopal, and P.V. Kamat, *Carbon nanostructures in portable fuel cells: Single-walled carbon nanotube electrodes for methanol oxidation and oxygen reduction*, Journal of Physical Chemistry B, **2004**. 108(52): p. 19960-19966.

[153] G. Girishkumar, M. Rettker, R. Underhile, D. Binz, K. Vinodgopal, P. McGinn, *et al.*, *Single-wall carbon nanotube-based proton exchange membrane assembly for hydrogen fuel cells*, Langmuir, **2005**. 21(18): p. 8487-8494.

[154] W.Z. Li, X. Wang, Z.W. Chen, M. Waje, and Y.S. Yan, *Carbon nanotube film by filtration as cathode catalyst support for proton-exchange membrane fuel cell*, Langmuir, **2005**. 21(21): p. 9386-9389.

[155] C.Y. Lee, H.M. Tsai, H.J. Chuang, S.Y. Li, P. Lin, and T.Y. Tseng, *Characteristics and electrochemical performance of supercapacitors with manganese oxide-carbon nanotube nanocomposite electrodes*, Journal of the Electrochemical Society, **2005**. 152(4): p. A716-A720.

[156] Z.-S. Wu, S. Pei, W. Ren, D. Tang, L. Gao, B. Liu*, et al.*, *Field Emission of Single-Layer Graphene Films Prepared by Electrophoretic Deposition*, Advanced Materials*,* **2009**. 21(17): p. 1756-1760.

[157] B.-K. Tay, *The hysteresis phenomenon of the field emission from the graphene film*, Applied Physics Letters*,* **2011**. 99(17): p. 173104.

[158] U.N. Maiti, S. Maiti, N.S. Das, and K.K. Chattopadhyay, *Hierarchical graphene nanocones over 3D platform of carbon fabrics: A route towards fully foldable graphene based electron source*, Nanoscale*,* **2011**. 3(10): p. 4135-4141.

[159] O. Akhavan and E. Ghaderi, *Toxicity of graphene and graphene oxide nanowalls against bacteria*, ACS nano*,* **2010**. 4(10): p. 5731-5736.

[160] S. Liu, J. Ou, J. Wang, X. Liu, and S. Yang, *A simple two-step electrochemical synthesis of graphene sheets film on the ITO electrode as supercapacitors*, Journal of Applied Electrochemistry*,* **2011**. 41(7): p. 881.

[161] V. Lee, L. Whittaker, C. Jaye, K.M. Baroudi, D.A. Fischer, and S. Banerjee, *Large-area chemically modified graphene films: electrophoretic deposition and characterization by soft X-ray absorption spectroscopy*, Chemistry of Materials*,* **2009**. 21(16): p. 3905-3916.

[162] J.R. Lake, A. Cheng, S. Selverston, Z. Tanaka, J. Koehne, M. Meyyappan*, et al.*, *Graphene metal oxide composite supercapacitor electrodes*, Journal of Vacuum Science & Technology B, Nanotechnology and Microelectronics: Materials, Processing, Measurement, and Phenomena*,* **2012**. 30(3): p. 03D118.

[163] S.J. An, Y. Zhu, S.H. Lee, M.D. Stoller, T. Emilsson, S. Park*, et al.*, *Thin film fabrication and simultaneous anodic reduction of deposited graphene oxide platelets by electrophoretic deposition*, The Journal of Physical Chemistry Letters*,* **2010**. 1(8): p. 1259-1263.

[164] S. Bittolo Bon, L. Valentini, J.M. Kenny, L. Peponi, R. Verdejo, and M.A. Lopez-Manchado, *Electrodeposition of transparent and conducting graphene/carbon nanotube thin films*, physica status solidi (a)*,* **2010**. 207(11): p. 2461-2466.

[165] Y.-B. Tang, C.-S. Lee, J. Xu, Z.-T. Liu, Z.-H. Chen, Z. He*, et al.*, *Incorporation of graphenes in nanostructured TiO2 films via molecular grafting for dye-sensitized solar cell application*, Acs Nano*,* **2010**. 4(6): p. 3482-3488.

[166] C.X. Guo, H.B. Yang, Z.M. Sheng, Z.S. Lu, Q.L. Song, and C.M. Li, *Layered Graphene/Quantum Dots for Photovoltaic Devices*, Angewandte Chemie International Edition, **2010**. 49(17): p. 3014-3017.

[167] B. Seger and P.V. Kamat, *Electrocatalytically active graphene-platinum nanocomposites. Role of 2-D carbon support in PEM fuel cells*, The Journal of Physical Chemistry C, **2009**. 113(19): p. 7990-7995.

[168] S. Liu, J. Wang, J. Zeng, J. Ou, Z. Li, X. Liu, *et al.*, *"Green" electrochemical synthesis of Pt/graphene sheet nanocomposite film and its electrocatalytic property*, Journal of Power Sources, **2010**. 195(15): p. 4628-4633.

[169] L. Tang, H. Feng, J. Cheng, and J. Li, *Uniform and rich-wrinkled electrophoretic deposited graphene film: a robust electrochemical platform for TNT sensing*, Chemical Communications, **2010**. 46(32): p. 5882-5884.

[170] G. Zhu, L. Pan, T. Lu, T. Xu, and Z. Sun, *Electrophoretic deposition of reduced graphene-carbon nanotubes composite films as counter electrodes of dye-sensitized solar cells*, Journal of Materials Chemistry, **2011**. 21(38): p. 14869-14875.

[171] H. Kim, H. Choi, S. Hwang, Y. Kim, and M. Jeon, *Fabrication and characterization of carbon-based counter electrodes prepared by electrophoretic deposition for dye-sensitized solar cells*, Nanoscale Research Letters, **2012**. 7(1): p. 53.

[172] E. Petrie, *Epoxy adhesive formulations*, **2005**: McGraw Hill Professional.

[173] H. Mahmood, M. Tripathi, N. Pugno, and A. Pegoretti, *Enhancement of interfacial adhesion in glass fiber/epoxy composites by electrophoretic deposition of graphene oxide on glass fibers*, Composites Science and Technology, **2016**. 126(p. 149-157.

[174] C.P. Green, H. Lioe, J.P. Cleveland, R. Proksch, P. Mulvaney, and J.E. Sader, *Normal and torsional spring constants of atomic force microscope cantilevers*, Review of Scientific Instruments, **2004**. 75(6): p. 1988-1996.

[175] J.E. Sader, J.W.M. Chon, and P. Mulvaney, *Calibration of rectangular atomic force microscope cantilevers*, Review of Scientific Instruments, **1999**. 70(10): p. 3967-3969.

[176] M.R. Gurvich, A.T. Dibenedetto, and A. Pegoretti, *Evaluation of the statistical parameters of a Weibull distribution*, Journal of Materials Science, **1997**. 32(14): p. 3711-3716.

[177] A. Dorigato and A. Pegoretti, *Tensile creep behaviour of polymethylpentene–silica nanocomposites*, Polymer International, **2010**. 59(6): p. 719-724.

[178] W.J. Parker, R.J. Jenkins, C.P. Butler, and G.L. Abbott, *Flash Method of Determining Thermal Diffusivity, Heat Capacity, and Thermal Conductivity*, Journal of Applied Physics, **1961**. 32(9): p. 1679-1684.

[179] F. Chen, D. Tripathi, and F.R. Jones, *Determination of the interfacial shear strength of glass-fibre-reinforced phenolic composites by a bimatrix fragmentation technique*, Composites Science and Technology, **1996**. 56(6): p. 609-622.

[180] A. Buchsteiner, A. Lerf, and J. Pieper, *Water dynamics in graphite oxide investigated with neutron scattering*, The Journal of Physical Chemistry B, **2006**. 110(45): p. 22328-22338.

[181] Q. An, A.N. Rider, and E.T. Thostenson, *Hierarchical composite structures prepared by electrophoretic deposition of carbon nanotubes onto glass fibers*, ACS applied materials & interfaces, **2013**. 5(6): p. 2022-2032.

[182] K.M. Lee and A.A. Polycarpou, *Shear strength determination using the nanoscratch technique and its application to thin solid films*, Journal of Materials Research, **2006**. 21(9): p. 2304-2313.

[183] F. Creuzet, G. Ryschenkow, and H. Arribart, *A New Tool for Adhesion Science: The Atomic Force Microscope*, The Journal of Adhesion, **1992**. 40(1): p. 15-25.

[184] S. Aoyama, Y.T. Park, C.W. Macosko, T. Ougizawa, and G. Haugstad, *AFM probing of polymer/nanofiller interfacial adhesion and its correlation with bulk mechanical properties in a poly(ethylene terephthalate) nanocomposite*, Langmuir, **2014**. 30(43): p. 12950-9.

[185] N.M. Pugno, Q. Yin, X. Shi, and R. Capozza, *A generalization of the Coulomb's friction law: from graphene to macroscale*, Meccanica, **2013**. 48(8): p. 1845-1851.

[186] D.P. Hunley, T.J. Flynn, T. Dodson, A. Sundararajan, M.J. Boland, and D.R. Strachan, *Friction, adhesion, and elasticity of graphene edges*, Physical Review B, **2013**. 87(3): p. 035417.

[187] J. Chen, D. Zhao, X. Jin, C. Wang, D. Wang, and H. Ge, *Modifying glass fibers with graphene oxide: Towards high-performance polymer composites*, Composites Science and Technology, **2014**. 97(p. 41-45.

[188] X. Wang, H. Yang, L. Song, Y. Hu, W. Xing, and H. Lu, *Morphology, mechanical and thermal properties of graphene-reinforced poly(butylene succinate) nanocomposites*, Composites Science and Technology, **2011**. 72(1): p. 1-6.

[189] G. Eda, C. Mattevi, H. Yamaguchi, H. Kim, and M. Chhowalla, *Insulator to semimetal transition in graphene oxide*, The Journal of Physical Chemistry C, **2009**. 113(35): p. 15768-15771.

[190] A. Pegoretti, H. Mahmood, D. Pedrazzoli, and K. Kalaitzidou, *Improving fiber/matrix interfacial strength through graphene and graphene-oxide nano platelets*, IOP Conference Series: Materials Science and Engineering, **2016**. 139(1): p. 012004.

[191] C.-W. Nan, Y. Shen, and J. Ma, *Physical Properties of Composites Near Percolation*, Annual Review of Materials Research, **2010**. 40(1): p. 131-151.

[192] W.-L. Song, M.-S. Cao, M.-M. Lu, S. Bi, C.-Y. Wang, J. Liu, *et al.*, *Flexible graphene/polymer composite films in sandwich structures for effective electromagnetic interference shielding*, Carbon, **2014**. 66(p. 67-76.

[193] P. Martins, A.C. Lopes, and S. Lanceros-Mendez, *Electroactive phases of poly(vinylidene fluoride): Determination, processing and applications*, Progress in Polymer Science, **2014**. 39(4): p. 683-706.

[194] S.K. Karan, D. Mandal, and B.B. Khatua, *Self-powered flexible Fe-doped RGO/PVDF nanocomposite: an excellent material for a piezoelectric energy harvester*, Nanoscale, **2015**. 7(24): p. 10655-10666.

[195] M. Sharma, G. Madras, and S. Bose, *Contrasting Effects of Graphene Oxide and Poly(ethylenimine) on the Polymorphism in Poly(vinylidene fluoride)*, Crystal Growth & Design, **2015**. 15(7): p. 3345-3355.

[196] M. Yin, C.K. Wu, Y. Lou, C. Burda, J.T. Koberstein, Y. Zhu, *et al.*, *Copper oxide nanocrystals*, J Am Chem Soc, **2005**. 127(26): p. 9506-11.

[197] B. Wang and H.-X. Huang, *Incorporation of halloysite nanotubes into PVDF matrix: Nucleation of electroactive phase accompany with significant reinforcement and dimensional stability improvement*, Composites Part A: Applied Science and Manufacturing, **2014**. 66(p. 16-24.

[198] R.K. Layek, A.K. Das, M.J. Park, N.H. Kim, and J.H. Lee, *Enhancement of physical, mechanical, and gas barrier properties in noncovalently functionalized graphene oxide/poly(vinylidene fluoride) composites*, Carbon, **2015**. 81(p. 329-338.

[199] N. An, S. Liu, C. Fang, R. Yu, X. Zhou, and Y. Cheng, *Preparation and properties of β-phase graphene oxide/PVDF composite films*, Journal of Applied Polymer Science, **2015**. 132(10): p. n/a-n/a.

[200] F. He, S. Lau, H.L. Chan, and J. Fan, *High Dielectric Permittivity and Low Percolation Threshold in Nanocomposites Based on Poly(vinylidene fluoride) and Exfoliated Graphite Nanoplates*, Advanced Materials, **2009**. 21(6): p. 710-715.

[201] F. Kremer and A. Schönhals, *Broadband Dielectric Spectroscopy*, **2012**: Springer Berlin Heidelberg.

[202] Z.-M. Dang, H.-P. Xu, and H.-Y. Wang, *Significantly enhanced low-frequency dielectric permittivity in the BaTiO3/poly(vinylidene fluoride) nanocomposite*, Applied Physics Letters, **2007**. 90(1): p. 012901.

[203] L.L. Sun, B. Li, Y. Zhao, G. Mitchell, and W.H. Zhong, *Structure-induced high dielectric constant and low loss of CNF/PVDF composites with heterogeneous CNF distribution*, Nanotechnology, **2010**. 21(30): p. 305702.

[204] F. Wen, Z. Xu, S.B. Tan, W.M. Xia, X.Y. Wei, and Z.C. Zhang, *Chemical Bonding-Induced Low Dielectric Loss and Low Conductivity in High-K Poly(vinylidenefluoride-trifluorethylene)/Graphene Nanosheets Nanocomposites*, Acs Applied Materials & Interfaces, **2013**. 5(19): p. 9411-9420.

[205] K. Yang, X. Huang, L. Fang, J. He, and P. Jiang, *Fluoro-polymer functionalized graphene for flexible ferroelectric polymer-based high-k nanocomposites with suppressed dielectric loss and low percolation threshold*, Nanoscale, **2014**. 6(24): p. 14740-14753.

[206] S. Wageh, L. He, A.A. Al-Ghamdi, Y.A. Al-Turki, and S.C. Tjong, *Nano silver-anchored reduced graphene oxide sheets for enhanced dielectric performance of polymer nanocomposites*, RSC Advances, **2014**. 4(54): p. 28426-28431.

[207] A. Roy, B. Dutta, and S. Bhattacharya, *Electroactive phase nucleation and non-isothermal crystallization kinetics study in [DEMM][TFSI] ionic liquid incorporated P(VDF-HFP) co-polymer membranes*, Journal of Materials Science, **2016**. 51(17): p. 7814-7830.

Other activities

Journal reviewing:

- Journal of Nanomaterials (IF = 1.758)
- Polymers (IF = 2.944)

Research activities:

- Research advisor of a graduate student (David Novel) in Materials Science and Engineering (University of Trento 2014-15) for thesis “Design and production of micro / nanofibers with graphene reinforcement”.
- Research advisor of a graduate student (Menkir Gashaw Birhane) in Materials Science and Engineering (University of Trento 2015-16) for thesis “Enhancing Interfacial Adhesion in Basalt Fiber/Epoxy Composites by Electrophoretic Deposition of Graphene Oxide”.
- Research collaborator to a visiting doctoral student (Parisa Fakhri) from “Bu-Ali Sina University, Hamedan, Iran” for the research work titled “Improved electroactive phase content and dielectric properties of flexible PVDF nanocomposite films filled with Au- and Cu-doped graphene oxide hybrid nanofiller”

Acknowledgements

The completion of my PhD thesis took place with the assistance of many people, and naming them all here seems to be impossible. However, mentioning some people cannot be left because of their most significant role.

First of all, my sincere regards and gratitude go to my advisor professor Alessandro Pegoretti for his utmost patience, invaluable guidance, genuine support and generosity over the tenure of my research work.

I would like to thank our laboratory technicians Alfredo Casagranda, Claudia Gavazza, and Lorenzo Moschini for their sincere and fruitful help towards the project work, material testing, analysis and other laboratory matters.

I would like to offer my sincerest gratitude to Professor Flavio Deflorian for allowing me to use the voltage meter in his laboratory to test the electrophoretic deposition of graphene oxide on my samples.

My expression of gratitude also extends towards professor Luca Fambri, professor Luca Lutterotti, professor Riccardo Ceccato, professor Gianluca Dalla Betta and Dr. Seraphin Unterberger for helping me carry out different characterization analysis on graphene and composite specimens.

My acknowledgment are also due to all my former and current colleagues especially Andrea Dorigato, Thiago Medeiros Araujo, Izabela Dabrowska, Diego Pedrazzoli, Annalisa Cataldi, Sithiprumnea Dul, Daniele Rigotti, Giulia Fredi and many others whose help in my PhD research efforts have made valuable difference.

Finally, I would like to thank my wonderful family and friends. Their support was more than crucial in keeping this project moving forward. A very special and heartfelt thank goes to my dearest parents, sisters and especially my wife for their endless help, support, prayers and wishes throughout my life. THANK YOU

Trento, December 18th 2016